



**New observational approaches for optically
complex waters based on high-resolution
transmissometry**

Ph.D Thesis

AUTHOR

Marta Ramírez Pérez

SUPERVISORS

Jaume Piera Fernández

David McKee



Universitat Politècnica de Catalunya

PhD Thesis

**New observational approaches for optically
complex waters based on high-resolution
transmissometry**

Author: Marta Ramírez Pérez

Supervisors: Dr. Jaume Piera Fernández, ICM-CSIC

Dr. David McKee, University of Strathclyde

Barcelona, 19 April 2017

New observational approaches for optically complex waters based on high-resolution transmissometry

Marta Ramírez Pérez

Instituto de Ciencias del Mar, CSIC

Dissertation submitted to the Universidad Politécnica de Cataluña as a requirement for the Doctoral degree with international mention. Speciality: Marine Sciences

Advisor - Dr. Jaume Piera Fernández (ICM-CSIC)

Co-advisor - Dr. David McKee (University of Strathclyde)

Tutor - Dr. Manuel Espino Infantes (UPC)

Tribunal - Dr. Mikel Latasa Arcalis (IEO)

Tribunal - Dr. Manel Grifoll Colls (UPC)

Tribunal - Dr. Stefan Simis (Plymouth Marine Laboratory)

External reviewer - Dr. Víctor Martínez Vicente (Plymouth Marine Laboratory-UK)

External reviewer - Dr. Arjun Chennu (Max-Planck-Institut-Germany)

Barcelona, April 2017

Abstract

There is a growing concern for protection and conservation of coastal ecosystems, which require a proper understanding of ecosystem dynamics and the ability to detect and predict changes in the ecosystem state. For this purpose, there is general agreement on the requirement of multidisciplinary and multiscale observing systems, due to the complex physical and biogeochemical processes occurring in these environments at a wide range of time-space scales.

In this sense, optical-based approaches arise as powerful tools since they allow to assess biogeochemical constituents at high temporal and spatial resolution. Moreover, the recent development of cost-effective, hyperspectral, compact and low power optical sensors has broadened their observational capabilities by allowing the assembly on a variety of platforms and by reducing the operational costs. Among the different optical properties, the beam attenuation coefficient presents numerous advantages due to the general availability and simplicity of operation and data processing of the required instrumentation (i.e. transmissometers).

In this context, this thesis seeks to improve the capabilities for coastal waters monitoring and assessment by developing new observational strategies based on high resolution beam attenuation measurements. With this aim, the reliability of a recent commercially available advanced-technology transmissometer (i.e. VIPER, TriOS GmbH) has been determined by analyzing the instrument uncertainties and performance. Despite some issues related to the thermal management of the LEDs and the contamination of ambient light, VIPER measurements have been validated in the field by comparison with other transmissometers.

Then, to evaluate to what extent is possible to retrieve environmental information from these measurements, attenuation data collected in the Mediterranean estuary of Alfacs Bay have been analyzed against laboratory-derived biogeochemical variables. The analysis has successfully used three major spectral features of the beam attenuation coefficient as qualitative proxies for the biogeochemical variables: coloured dissolved organic matter (CDOM), Chlorophyll a (Chl-a) and total suspended matter (TSM), allowing the detection of changes and patterns in these variables at high temporal and spatial resolution. Thereby, high-frequency in situ beam attenuation measurements are proposed as cost-effective, rapid and simple method to better understand the complex physical and biogeochemical interactions in coastal environments.

Nevertheless, there are numerous factors affecting the attenuation signal, which restrict the

capability of these measurements to quantitatively assess the biogeochemical constituents and involve that complementary optical data are required. For this reason, an additional approach has been investigated by including spectral absorption measurements collected in situ with a dual spectrophotometer widely used by the scientific community. An inversion model of attenuation and absorption data has been developed based on local material-specific inherent optical properties to quantitatively estimate CDOM, Chl-a and mineral suspended solids in optically complex waters. The advantages of this approach lie in the simple input requirements, the avoidance of error amplification, full exploitation of the available spectral information and the reasonably successful retrieval of constituent concentrations.

In summary, this thesis has proposed two complementary beam attenuation-based approaches for complex coastal waters. On one hand, cost-effective and compact transmissometers allow to determine the scales of variability in the in-water constituents, providing a comprehensive overview of the biogeochemical processes. On the other hand, this information is highly valuable to define the optimal sampling strategy to be adopted with more sophisticated optical sensors required to estimate the concentration of the biogeochemical variables in a water body.

Resumen

Existe la necesidad de desarrollar herramientas capaces de predecir y detectar cambios en el estado de los ecosistemas costeros con el fin último de proteger y conservar dichos sistemas. Para ello, es necesario el uso de sistemas de observación multidisciplinares y multiescala, dada la complejidad de los procesos físico-biogeoquímicos y los numerosos cambios que se producen a diversas escalas espacio-temporales. Uno de los métodos más efectivos y utilizados para evaluar el estado biogeoquímico de las masas de agua a alta resolución espacio-temporal se basa en la medición de sus propiedades ópticas. Entre las distintas propiedades ópticas, la atenuación presenta numerosas ventajas, como por ejemplo la sencillez de uso y procesamiento de los datos de los instrumentos utilizados (los transmisómetros).

En este contexto, el objetivo de esta tesis consiste en investigar nuevas técnicas de análisis de aguas costeras utilizando datos de atenuación de la luz medidos in situ a alta resolución espacio-temporal. En primer lugar, se ha determinado la fiabilidad de los datos recogidos por un transmisómetro de última generación caracterizado por su bajo coste y fácil manejo (VIPER, de TriOS GmbH). Los resultados aportan medidas fiables de atenuación en aguas costeras, a pesar de que este análisis también muestra una serie de limitaciones relacionadas con la gestión térmica de los LEDs y con la contaminación por luz ambiente.

Una vez caracterizado el instrumento, se ha analizado el tipo de información ambiental que se puede extraer de estas medidas utilizando los datos recogidos en la bahía mediterránea de los Alfacs y correlacionándolos con las variables biogeoquímicas obtenidas a partir de muestras discretas de agua. El estudio se basa en la utilización de tres parámetros calculados a partir del espectro de atenuación como indicadores de las tres principales variables biogeoquímicas (la materia orgánica disuelta coloreada -CDOM-, la clorofila-a y la concentración de material particulado). Esto ha permitido detectar cambios y patrones en dichas variables de una forma rápida, sencilla y económica. Así, este método se propone como una herramienta eficaz para entender las complejas interacciones físico-biogeoquímicas en las aguas costeras.

Sin embargo, la señal de atenuación se ve afectada por la influencia de numerosos factores, lo que limita su capacidad para cuantificar los constituyentes biogeoquímicos e implica la necesidad de recurrir a medidas ópticas adicionales para lograr este fin. Por esta razón, se ha desarrollado otro método de observación que incluye, además de la atenuación, medidas de absorción, ambas recogidas con un espectrofotómetro doble ampliamente utilizado por la comunidad científica. Se ha desarrollado un modelo de inversión de los datos de atenuación

y absorción basado en las propiedades ópticas inherentes específicas de cada constituyente, que fueron obtenidas a partir de muestras de agua de la zona de estudio (el mar de Liguria). Dicho modelo ha permitido cuantificar satisfactoriamente la concentración de CDOM, de clorofila-a y de partículas inorgánicas en aguas ópticamente complejas, utilizando datos de entrada muy sencillos y explotando toda la información espectral disponible.

En resumen, esta tesis presenta dos aproximaciones basadas en medidas de atenuación que pueden considerarse complementarias. Por un lado, los transmisómetros de bajo coste y fácil manejo permiten determinar las escalas de variabilidad de los principales componentes biogeoquímicos para adquirir una idea global del funcionamiento del ecosistema. Por otro lado, esta información es de gran utilidad a la hora de definir la estrategia de muestreo a implementar con instrumentos más sofisticados que permitan cuantificar la concentración de dichas variables en zonas más localizadas.

Acknowledgements

En primer lugar, mi mayor agradecimiento es para mi director de tesis Jaume Piera, por abrirme las puertas a este grupo de investigación y a la ciencia en general, y por darme la oportunidad de realizar esta tesis (oportunidad muy valiosa, por cierto, dado lo mucho que escasean hoy en día). Gracias por tus ideas y por toda la confianza y libertad depositadas, que me han hecho crecer y madurar en todos los aspectos.

I am also very grateful to my supervisor David McKee, for all your support, motivation and for sharing your knowledge. I was very lucky to learn from such a enthusiastic, generous and competent researcher.

Mi más sincero agradecimiento a mis compañeros del grupo de bio-óptica: Elena Torrecilla, Carine Simone, Raúl Bardají, Eloy Zafra y Albert Sánchez. A Elena y Albert, mis compañeros de despacho, muchas gracias por vuestra paciencia, consejos y apoyo y por haber creado tan buen ambiente en el despacho, que hizo que yo me sintiera allí como en mi casa. Además, gracias a Elena por las tardes tan amenas y divertidas que compartimos juntas, siempre acompañadas por Nora y Ton. A Raúl y a Eloy, gracias por todas las experiencias compartidas. Me quedo con nuestras aventuras durante las pre-campañas de campo. A Carine, gracias por tu sonrisa diaria y por nuestros almuerzos al sol en la playa. Y a Oriol Sánchez, gracias por todos los detalles que tienes con nosotros. En este grupo no sólo he encontrado buenos compañeros de trabajo, sino también amigos con los que compartir los buenos y malos momentos.

In addition, I warmly thank to my “external menthors”: Dr. Rüdiger Röttgers and Prof. Astrid Bracher, without their help this thesis wouldn't have been possible. Thanks for your support and ideas. Thank you very much for hosting me and for opening the doors of your departments and laboratories. Thanks also to all the people from these groups (Remote Sensing department from the Helmholtz Zentrum Geesthacht, the Phytooptics group from the Alfred-Wegener-Institute and the Marine optics and Remote Sensing Group from the University of Strathclyde) for your warm welcome. Special thanks to Rafael Gonçalves-Araujo, Sonja Wiegmann and Christian Utschig. It was a real pleasure to work and collaborate with you.

I also thank to the external reviewers Dr. Arjun Chennu (Max-Planck-Institut) and Dr. Víctor

Martínez Vicente (Plymouth Marine Laboratory) for their careful reading of the thesis and for providing valuable comments.

Thanks to NASA and University of Maine, for giving me the opportunity of taking part in the Ocean Optics Summer Course in July 2013, which allowed me to build a knowledge base about the Ocean Optics and meet really nice people.

Gracias a muchos otros compañeros del Instituto de Ciencias del Mar. En especial, gracias a Joaquim Ballabrera, por haberme dado la oportunidad de empezar esta tesis y por ese apoyo tan necesario a comienzos del doctorado. A Jorge Guillén y otros miembros del departamento de Geología marina (Oriol Mulet, Silvia de Diago y Neus Maestro) por vuestra ayuda, consejos, material e instrumentos prestados. Muchísimas gracias a Alejandro Olariaga, Verónica Fuentes y Melissa Acevedo, del departamento de Biología marina, por vuestro apoyo altruista y fundamental durante nuestras campañas de campo.

A las chicas, Marta Umbert, Nina Hoareau y Ana Trindade, por estar siempre ahí. Por ser esa vía de escape cuando lo necesitaba, por todas las risas y momentos compartidos. En especial, gracias a Marta, sin la cual todo esto no hubiese sido posible. Gracias a los demás (ex-) doctorandos del DOFT (Sergio, Suso, Ignasi, Paola, Sebastien, etc.) y a todos los compañeros del club de montaña Aresta Nord, por crear tan buen ambiente en el ICM. En especial, gracias a Gustavo por enseñarme a escalar; a Alberto por ser el motor del club; y a Raquel y Quim, por aquél verano descubriendo nuevos rincones de Cataluña.

Agradecer también a las amigas de Barcelona (Kati, Leti, María, Mayte y Maite), colegas de escalada y danza africana y compañer@s de piso, por haber hecho de mis años en Barcelona una etapa de mi vida única e inolvidable.

Gracias a mi familia (Puly, Hermi, Pablo y Nuria), por estar siempre ahí apoyándome en todo momento. A mi sobrina Amanda, que está de camino y nos llenará de alegría. A mi abuela y a todos mis tí@s y prim@s, en especial a Rafa y Ángel, por vuestro apoyo y consejos. Y por último, y ocupando un lugar especial, gracias a Jorge, por ser la persona que me aguanta cada día y con la que comparto las mayores alegrías y risas.

Contents

List of Figures	xi
List of Tables	xv
Notation	xvii
0 Introduction	1
0.1 Motivation	1
0.2 Objectives	3
0.3 Thesis outline	3
1 Theoretical Background	5
1.1 Coastal environments: Importance and vulnerability	6
1.2 Water as an optical medium	8
1.2.1 Classification of natural waters	9
1.2.2 Optical properties of natural waters	10
1.2.3 Optically active constituents in water	14
1.2.3.1 Characteristics of particles affecting their optical properties	16
1.3 Inherent Optical Properties	19
1.3.1 Absorption properties	19
1.3.2 Scattering properties	22
1.3.3 Attenuation properties	24
1.3.3.1 Measurements of bulk and constituent-specific absorption and scattering coefficients	25
1.4 Optical sensors: IOPs devices	26
1.4.1 Transmissometers	26
1.4.2 Absorption meters	29
1.4.3 Scattering meters	29
2 Characterization of advanced-technology transmissometers: performance and uncertainty analyses	31
2.1 Introduction	32

2.2	Material and Procedures	33
2.2.1	Instrument description	33
2.2.1.1	Principles of operation	33
2.2.2	Uncertainty assessment of the measurement system	35
2.3	Assessment	37
2.3.1	Instrument stability	37
2.3.1.1	Instrument precision	37
2.3.1.2	Thermal management	37
2.3.2	Instrument-Specific temperature and salinity correction factors	39
2.3.2.1	Temperature correction coefficients	39
2.3.2.2	Salinity correction coefficients	40
2.3.3	Ambient light effects	41
2.3.4	Instrument performance during in situ measurements	43
2.3.4.1	VIPER <i>vs</i> AC-S	43
2.3.4.2	VIPER <i>vs</i> LISST 100X	45
2.4	Discussion	45
2.5	Conclusions	47

3 Application of cost-effective spectral beam attenuation measurements to assess changes and patterns in biogeochemical variables in a coastal environment 49

3.1	Introduction	50
3.2	Material and Methods	51
3.2.1	Study site	51
3.2.2	Field campaign	51
3.2.2.1	Physical parameters	52
3.2.2.2	Optical measurements	52
3.2.2.3	Laboratory analysis of water samples	53
3.2.2.4	Data and statistical analysis	55
3.3	Results and Discussion	57
3.3.1	Validation of biogeochemical proxies	57
3.3.1.1	Attenuation at 710 nm <i>vs.</i> Total Suspended Matter concentration	57
3.3.1.2	$c_{pg}(685)$ peak height <i>vs.</i> Chl-a concentration	58
3.3.1.3	Spectral slope of total non-water beam attenuation <i>vs.</i> $a_{CDOM}(443)$ 59	
3.3.2	Spatial variability	61
3.3.3	Temporal variability	64
3.4	Conclusions	66

4	Quantitative estimates of constituent concentrations in optically complex waters by means of inversion procedure of in situ spectral attenuation and absorption measurements	69
4.1	Introduction	71
4.2	Theory	72
4.2.1	A linear spectral deconvolution model for inversion of in situ ac-9 data	72
4.2.2	Practical implementation of the spectral deconvolution model	74
4.2.3	Propagation of measurement uncertainty	75
4.3	Materials and Methods	75
4.3.1	Field data	75
4.3.2	In situ optical measurements	76
4.3.3	Laboratory measurements	77
4.4	Results	78
4.4.1	Water type classification	78
4.4.2	Determination of SIOPs and associated uncertainties	80
4.4.3	Spectral deconvolution model sensitivity analysis	81
4.4.4	Inversion of in situ IOPs at sample depths	84
4.4.5	Deconvolution of vertical IOP profiles	86
4.5	Discussion	91
4.6	Conclusions	92
5	Conclusions and outlook	95
5.1	Summary of contributions	96
5.1.1	Summary and contributions of Chapter 2: “ <i>Characterization of advanced-technology transmissometers: performance and uncertainty analyses</i> ”:	97
5.1.2	Summary and contributions of Chapter 3: “ <i>Application of cost-effective spectral beam attenuation measurements to assess changes and patterns in biogeochemical variables in a coastal environment</i> ”:	98
5.1.3	Summary and contributions of Chapter 4: “ <i>Quantitative estimates of constituent concentrations in optically complex waters by means of inversion procedure of in situ spectral attenuation and absorption measurements</i> ”:	98
5.2	Applications and future research	99
	Bibliography	101

List of Figures

1.1	Schematic diagram with temporal and spatial scales of oceanic processes.	8
1.2	Example of waters dominated by different components	9
1.3	Diagrammatic representation of Case 1 and Case 2 waters	10
1.4	Relationships between the different quantities commonly used in hydrological optics	11
1.5	Geometry used to define the Inherent Optical Properties	12
1.6	The size distribution of mineral particles transported by Amazon River	16
1.7	Representative sizes of different in-water constituents	18
1.8	Examples of different shapes of marine particles	18
1.9	Pure water absorption spectrum taken from Pope & Fry (1997)	20
1.10	Exemplary CDOM absorption spectra measured in Alfacs Bay (NW Mediterranean) in June 2013.	20
1.11	Absorption spectra of individual photosynthetic pigments in solvents	21
1.12	Exemplary mass-specific absorption spectra of non-algal particles	23
1.13	Scattering coefficient for pure seawater derived from Morel (1974)	23
1.14	Measured volume scattering functions from three natural waters with different particle load and Scattering cross section vs wavelength for two different particle sizes	24
1.15	Transmissometer design with a collimated optical system	27
2.1	Hyperspectral VIS-Photometer VIPER (TriOS GmbH), path length of 25 cm.	33
2.2	Individual light emission spectra of the 5 LEDs used by VIPER	34
2.3	Sources of uncertainties in LED-based hyperspectral open-path transmissometers	35
2.4	Stability of the VIPER output signal over one hour	37
2.5	Normalized transmitted light intensity as function of the operating temperature at the emission peak wavelengths of the five LEDs	38
2.6	Corrected beam attenuation spectrum of purified water at different LED temperatures	39
2.7	Results from the temperature dependence analysis of VIPER and the comparison with model simulations	40

2.8	Results from the salinity dependence analysis of VIPER and the comparison with model simulations	41
2.9	Example of ambient light contamination	42
2.10	Light and dark VIPER measurements collected at different depths	42
2.11	Comparison between VIPER and ACS in the field	44
2.12	Comparison between VIPER-derived and ACS-derived attenuation spectral slopes	44
2.13	Comparison between VIPER and LISST in the field	45
3.1	Location map of Alfacs Bay in NW Mediterranean Sea	52
3.2	Spectral features of the beam attenuation coefficient used as proxies for biogeochemical variables	55
3.3	$c_{pg}(710)$ as proxy for TSM	58
3.4	$c_{pg}(685)$ peak as proxy for Chl-a	59
3.5	c_{pg} slope as proxy for CDOM	60
3.6	Analysis of the spatial variability in Alfacs Bay	61
3.7	Optical properties measured at seven stations in Alfacs Bay and over the water column	62
3.8	Spatial distribution of proxies from non-water beam attenuation and biogeochemical variables	63
3.9	Analysis of partitioned absorption data in Alfacs Bay	64
3.10	Time series of physical forcings along 48 hours in Alfacs Bay	65
3.11	Optical measurements collected during profiling along 48 hours for the analysis of temporal patterns in Alfacs Bay	66
3.12	Variations with time and depth in the attenuation-based proxies and PSD slope along with the current velocity	67
3.13	Variations with time and depth in biogeochemical variables	67
4.1	Study area and MODIS images of the Ligurian Sea in March 2009	76
4.2	Particulate backscattering against particulate scattering at 532 nm and Chl against total suspended matter concentration (TSS) for all the stations from Ligurian Sea	79
4.3	440 nm normalized Phytoplankton and CDOM absorption spectra	79
4.4	Material-specific IOPs with 95% confidence bounds	80
4.5	Chl standard deviation distributions for the synthetic IOP data set incorporating different sources of error	84
4.6	Spread and offset error distributions for Chl, TSS_{nd} and CDOM	85

4.7	Comparison of retrieved versus measured Chl and CDOM for offshore stations (Case I waters model)	86
4.8	Comparison of retrieved versus measured <i>Chl</i> , <i>TSS_{nd}</i> and <i>CDOM</i> for onshore stations (Case II waters model)	87
4.9	Chl depth profiles from onshore stations in the Ligurian Sea retrieved from the inversion of AC-9 measurements	88
4.10	<i>TSS_{nd}</i> depth profiles from onshore stations in the Ligurian Sea retrieved from the inversion of AC-9 measurements	89
4.11	CDOM depth profiles from onshore stations in the Ligurian Sea retrieved from the inversion of AC-9 measurements	90
4.12	Nonbiogenic detrital scattering coefficient, $b_{nd}(\lambda)$, normalized at 440 nm	93

List of Tables

1.1	Most commonly used commercial transmissometers and their characteristics.	28
3.1	Mean and standard deviation of the non-water beam attenuation-based proxies and biogeochemical variables for waters above and below the pycnocline . . .	63
4.1	Constituent concentration ranges used in the generation of the synthetic IOP data set.	82
4.2	Minimum and maximum standard deviations (σ) and offset errors of the retrieved variables obtained from the inversion of simulated IOPs.	84
4.3	RMSE errors obtained from the inversion of in situ AC-9 measurements of offshore and onshore stations from Ligurian Sea.	86

Notation

$a(\lambda)$ - Total absorption coefficient
 $a_{bd}(\lambda)$ - Biogenic detritus absorption coefficient
 $a_{CDOM}(\lambda)$ - CDOM absorption coefficient
 $a_{nap}(\lambda)$ - Non-algal particulate absorption coefficient
 $a_{nd}(\lambda)$ - Nonbiogenic detritus absorption coefficient
 $a_p(\lambda)$ - Particulate absorption coefficient
 $a_{ph}(\lambda)$ - Phytoplankton absorption coefficient
 $a_i * (\lambda)$ - Mass-specific absorption coefficient of the component i
 $a_w(\lambda)$ - Absorption coefficient of pure water
 AOP - Apparent optical properties
 $b(\lambda)$ - Total scattering coefficient
 $b_b(\lambda)$ - Backscattering coefficient
 $c(\lambda)$ - Total attenuation coefficient
 $c_p(\lambda)$ - Particulate attenuation coefficient
 $c_{pg}(\lambda)$ - Total non-water attenuation coefficient
 $CDOM$ - Coloured Dissolved Organic Matter
 $Chl - a$ - Chlorophyll a
 D - Volume equivalent sphere diameter of a particle
 $FWHM$ - Full width at half maximum
 $IOPs$ - Inherent optical properties
 $LEDs$ - Light emitting diodes
 MSS - Mineral suspended solids
 $N(D)$ - Particle number distribution at the size diameter D
 PSD - Particle size distribution
 RTE - Radiative transfer equation
 $SCDOM$ - CDOM absorption spectral slope
 $SIOPs$ - Specific inherent optical properties
 S - Salinity
 T - Temperature
 TSM - Total suspended matter
 $V(D)$ - Particle volume distribution at the size diameter D

λ - Wavelength

γ - Attenuation spectral slope

$\theta(\lambda)$ - Spectral radiant power

$\psi_T^i(\lambda)$ - Temperature correction factor

$\psi_S^i(\lambda)$ - Salinity correction factor

ξ - PSD slope

0

Introduction

0.1 Motivation

Coastal ecosystems are globally threatened by anthropogenic impacts, which have increased in the last decades as result of human expansion and climate change. These increasing pressures have led to rapid rates of ecosystem degradation and habitat destruction, carrying serious problems such as contamination and risk for human health. Given the great ecological, economic and social importance of coastal ecosystems, different national policies and international agreements and strategies have been established and implemented with the aim of protecting these valuable ecosystems, managing their resources and ensuring their sustainable development. The first steps to accomplish it require (1) to understand the ecosystem states, (2) to detect changes and perturbations in these states and (3) to understand the effects of these perturbations on coastal ecosystem, which is a big challenge due to the complex dynamics of coastal environments. Furthermore, the high costs associated with instruments acquisition and maintenance, logistics and qualified personnel expenses hamper the sustainable and long-term assessment of coastal waters. For this reason, there is an urgent need to develop new techniques for monitoring and assessing complex coastal waters at the appropriate time-space scales. These techniques should be also characterized by the use of cost-effective, low power, compact and easy-to-handle instrumentation, to minimize the observational costs. In this sense, the use of optical-based approaches have proven to provide a powerful tool, as they allow to resolve in-water variability at high temporal and spatial scales. Furthermore, in situ optical sensors are ideally suited to be deployed on a variety of platforms including moorings, AUVs and from ships which improve their operational capabilities. Among the different optical properties, the beam attenuation coefficient presents distinct advantages due to the general availability and relatively simple operation and data processing of the required instrumentation (i.e. transmissometers or beam attenuation meters). In fact, these instruments have been in use for more than forty years and are the most commonly employed measuring devices of Inherent Optical Properties (IOPs). They present a variety of applications ranging from determinations of particulate matter, chlorophyll a -Chl-a- (as

proxy for phytoplankton biomass) or particulate organic carbon -POC- concentrations to particle size characteristics. However, various of the relationships found between the beam attenuation coefficient and seawater constituents fail for optically complex waters (such as coastal environments) and thus, they are restricted to clear oceanic waters. Bulk beam attenuation coefficients measured in coastal environments respond to the combined scattering and absorption action of a complex mixture of constituents, including phytoplankton and associated biogenic detritus, mineral suspended particles and coloured dissolved organic material. The multiple optical contributions affecting this signal restrict the capability of beam attenuation measurements in deriving information about seawater compounds and, consequently, involve that ancillary measurements are needed to separate bulk attenuation into single constituent IOP. Nevertheless, studies based on the beam attenuation signal used, exclusively, the particulate attenuation coefficient at one specific wavelength (commonly at 532, 555, 660 or 670 nm) or the particulate attenuation spectral slope, whereas the rest of the visible spectrum remains unexplored. The recent development of high-spectral (hyperspectral) resolution transmissometers broadens the possibility to extract more extensive information from these measurements, as occurred for other optical properties (e.g. particulate absorption or remote sensing reflectance). Furthermore, economically affordable, compact and low power in situ sensors have emerged in recent years as result of advances in technology, which improve considerably the ability to perform research, long term monitoring and sustained operational programs in coastal ecosystems. In this context, this thesis seeks to explore, firstly, the potential and limitations of inexpensive advanced-technology transmissometers for coastal waters applications and, secondly, the full spectral information contained in the beam attenuation coefficient as optical proxy for the major biogeochemical variables. Thus, the general questions addressed in the framework of this thesis, are:

- *How much information of biogeochemical constituents can be retrieved from in situ spectral beam attenuation measurements in optically complex waters?*
- *Can optical transmissometers provide a potential tool to address the actual needs of high resolution and cost-effective observing systems for optically complex waters?*

To answer these questions, two different strategies have been adopted along this thesis. Firstly, we focus on the potential of recently-developed advanced-technology transmissometers. Secondly, the research is conducted by means of a widely used and validated dual spectrophotometer (beam attenuation and absorption meters), due to the larger observational capabilities provided by additional absorption data.

0.2 Objectives

General objective:

This thesis aims to investigate new observational approaches based on in situ measurements of beam attenuation coefficient to fulfill the urgent demand for sustained and routine characterization of coastal waters environments. With this purpose, we seek to explore and exploit all the spectral information contained in the beam attenuation signal since it can provide useful insights about biogeochemical constituents present in water.

Specific objectives:

- **Objective 1:** To determine the reliability and limitations of beam attenuation measurements collected in situ with a recently developed advanced-technology and cost-effective transmissometer.
- **Objective 2:** To develop and implement an observational strategy based on high resolution, cost-effective and rapid beam attenuation measurements in order to better understand the ranges of variability and the physical and biogeochemical interactions in a complex coastal environment.
- **Objective 3:** To derive quantitative estimates of the major in-water constituents by including additional optical data beyond the spectral attenuation coefficient.

0.3 Thesis outline

In order to address the above listed objectives, the manuscript has been structured as follows:

Chapter 1 provides a theoretical background about optical oceanography, by describing the concepts, the optically active water compounds, the measuring devices and the most important applications of optical-based approaches. Special attention has been paid to the Inherent Optical Properties (IOPs), since the beam attenuation coefficient (as an IOP) is the focus of this thesis. At the beginning of this chapter, the importance of studying coastal ecosystems is described.

Chapter 2 addresses the first specific objective, which seeks to analyze the practicality and suitability of a new generation and still unexplored transmissometer, characterized by being hyperspectral, cost-effective, compact and low power. With this purpose, the instrument uncertainties and limitations were examined and the sensor performance was compared with other widely used and validated transmissometers. This chapter has been published in:

Chapter 0

Ramírez-Pérez M, Röttgers R, Torrecilla E, Piera J. Cost-effective hyperspectral transmissometers for oceanographic applications: performance analysis. Sensors 2015; 15: 20967-20989. doi:10.3390/s150920967.

Once the instrument uncertainties were characterized and the potential limitations were defined, its application as optical tool for assessing complex coastal environments was tested. This analysis is presented in **Chapter 3**, which addresses the second specific objective. This chapter has been published in: *Ramírez-Pérez M, Gonçalves-Araujo R, Wiegmann S, Torrecilla E, Bardaji R, Röttgers R, Bracher A, Piera J. (2017) Towards Cost-Effective Operational Monitoring Systems for Complex Waters: Analyzing Small-Scale Coastal Processes with Optical Transmissometry. PLoS ONE 12(1): e0170706. doi:10.1371/journal.pone.0170706.*

The numerous factors affecting the beam attenuation signal compromise the ability of optical transmissometers to derive quantitative estimates of the optically active water compounds. For this reason, in **Chapter 4**, additional spectral absorption data were included in the analysis beyond the attenuation coefficient, due to the general availability of both optical properties derived from a commonly used dual spectrophotometer. With both IOPs, an inversion model was developed to estimate the concentration of the major in-water constituents CDOM, Chl-a and inorganic particle concentrations. This chapter is in process to be published in: *Ramírez-Pérez M., Twardowski M., Trees C., Piera J., McKee D. (2017) Inversion of in situ absorption and attenuation measurements to estimate constituent concentrations in optically complex shelf seas. Journal of Geophysical Research: Oceans. In press.*

Finally, **Chapter 5** summarizes the results achieved in this thesis and points the direction of future work. Some guidelines for future applications are also proposed.

1

Theoretical Background

This chapter provides the theoretical framework of this thesis, including the conceptual background of optical oceanography and related findings presented in the reviewed literature.

1.1 Coastal environments: Importance and vulnerability

Coastal regions are defined to range from the continental shelf (to a depth of 200 m), the intertidal areas and adjacent land within 100 km of the coastline (Martínez *et al.* 2007). These environments are a valuable and finite resource, with high ecological, economic and social importance.

From an **ecological point of view**, coastal ecosystems are among the most productive systems in the world, with high ecological value (MEA 2005). They harbor a great biological diversity and provide a wide array of habitats and essential sources for supporting life in the ocean and the bordering land. In addition, shelf seas act as important interfaces for global material cycles, since they are subject to a continuous influx of natural and anthropogenic material from river systems and the atmosphere. Therefore, these ecosystems are of great importance in terms of nutrient assimilation and carbon fixation, with an estimated uptake rate of atmospheric CO_2 ranging between 0.33 and 0.36 Pg C yr^{-1} (Tang *et al.* 2011).

From an **economic point of view**, these environments generate significant revenues derived from a wide array of human activities such as fisheries, tourism, recreation, shipping, natural resources (*e.g.* oil and gas) extraction, industry, infrastructures, agriculture and aquaculture, etc. In particular, the mean annual value of goods and services from the world's coastal ecosystems is estimated to be greater than \$25,000 billion per year. According to Costanza *et al.* (1997) coastal ecosystems contribute 77% of global ecosystem-services value. Coastal zones account for 90% of marine fisheries catch (MEA 2005).

From a **social point of view**, coastal ecosystems support 41% of total population (*i.e.* 2.385 million people) living within 100 kilometers of the coastline and 21 of the 33 world's megacities are found on the coast (Martínez *et al.* 2007). All these people depend directly on the adjacent sea for livelihood and well-being.

Coastal ecosystems are vulnerable areas subjected to considerable pressures derived from the multiple above mentioned human activities. As a result of human expansion and destruction of natural habitats, coastal marine and estuarine ecosystems have experienced rapid rates of degradation over the last 150 to 300 years. This habitat degradation carried, in many cases, serious environmental and economic consequences, such as harmful algal blooms (HABs), anoxia, accumulation of pollutants and toxins or over-exploited fisheries (Kennish 2002). Added to this, the effects of climate change (such as sea level rise and ocean acidification) and natural hazards are threatening the capability of coastal ecosystems to support goods and valuable services (Malone *et al.* 2010).

For these reasons, understanding and monitoring coastal ecosystems is highly valued, not only from a scientific point of view, but also due to its social and economic values. Since the 1960s,

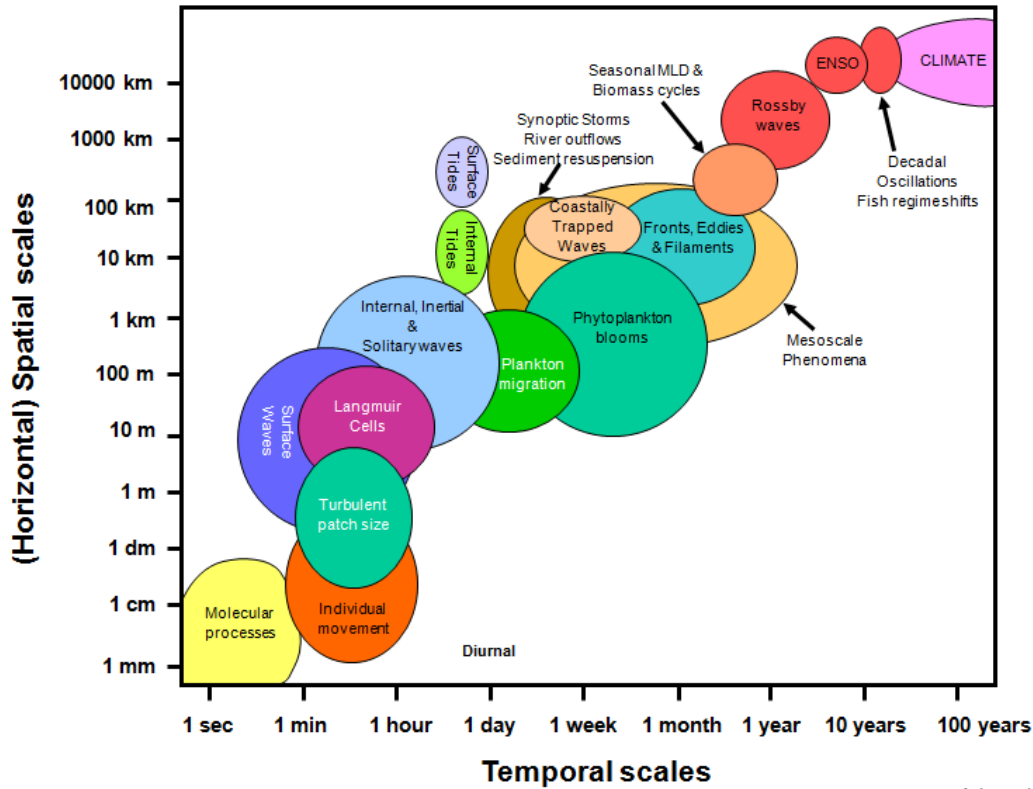
Chapter 1

there has been an increasing concern over the impacts of the changes in coastal ecosystems as result of human population growth and climate change. This has led to many national policies and international conventions and agreements, aimed at the preservation, conservation and sustainable use of coastal ecosystems. According to these conventions, there is a need for adaptive, ecosystem-based approaches to sustainable development, which involves integrated, multidisciplinary and multiscale coastal observing systems. In this context, some examples of European interdisciplinary research programs are the coastal module of the global ocean observing system (coastal GOOS), the Coastal Observing System for Northern and Arctic Seas (COSYNA), the Global Earth Observations System of Systems (GEOSS) or the Marine Geological and Biological Habitat Mapping (GEOHAB).

However, coastal environments are still little understood and insufficiently monitored, due to their high dynamic behavior. They are complex natural systems that interact with terrestrial, oceanic and atmospheric processes. These environments are affected by large variations in water levels, controlled by offshore and wind-driven currents, waves, tides, storm surges, sea level rise and inputs from stream flow and groundwater. In response to all these processes, coastal ecosystems undergo continuous changes over a broad spectrum of time-space scales (from hours to decades and from meters to thousands of kilometers) (Fig. 1.1). Continuous and routine provision of data are therefore required in order to assess the states of marine and estuarine ecosystems, detect changes in these states and evaluate their impacts.

Water-quality monitoring in aquatic ecosystems has historically consisted of collecting water samples weekly or monthly for later laboratory analyses. Besides this kind of analyses can take days or weeks to complete, they have high costs and involve logistic and technical constraints. These traditional techniques are therefore time-consuming and provide low-frequency and delayed data. This hampers a timely response during events, limits the ability to identify specific causes or actions, and may result in poorly quantified effects on ecosystems. Technological advancements in commercial in situ sensors, data platforms, and new techniques for data analysis provide an opportunity to monitor aquatic ecosystems on the time scales in which changes occur. In addition, the availability of these data in real-time enables the early trend detection, the mitigation of adverse effects and supplies valuable information in decisions making. Nevertheless, there exist numerous difficulties in obtaining long-term and high-resolution consistent measurements, due to the elevated costs (including the equipments, installation, operational and maintenance costs). For this reason, there is also a demand for compact, inexpensive, stable and low power in situ sensors to facilitate sustained monitoring.

In this sense, optical measurements offer a powerful tool since the water optical characteristics are strongly related to biological, chemical and physical processes in the water. Thus,



Adapted from Dickey et al. 2005

Figure 1.1: Schematic diagram with temporal and spatial scales of oceanic processes.

continuous in-situ measurements of water optical properties allow to determine changes in the biological composition as well as in the concentration of optically active constituents in coastal regions, monitor the water quality and identify the underlying causes of any changes in the water characteristics (*e.g.* Moore *et al.* 2009). Moreover, recent advances in optical sensor technology have enabled to develop miniaturized, low power and cost-effective instrumentation, which promote these sensors to be mounted on a variety of observing platforms such as moorings, drifter buoys, and autonomous vehicles. All these advances have allowed to analyze biogeochemical processes in aquatic environments at high temporal and spatial resolution that were not possible before, such as sub-meter and sub-second scales.

1.2 Water as an optical medium

Understanding how light interacts with sea water is fundamental to many research fields such as biological primary production, mixed-layer thermodynamics, photochemistry, lidar bathymetry, ocean-color remote sensing, etc. For this reason, optics is one of the fastest growing oceanographic research areas. Most of the variability in the optical properties of the upper ocean is due to changes in the concentration and type of constituents present in

the water, which in turn, are often of interest to ecologists and biogeochemists. Thereby, the ability to derive information about the in-water constituents at wide range of space and time scales based on the analysis of the optical properties motivates much of the research in ocean optics.

1.2.1 Classification of natural waters

The optical complexity of natural waters differ greatly among different aquatic environments, which exhibit broad variations in transparency, color and composition. These optical characteristics affect the magnitude and spectral behavior of light penetrating into the water column. In order to indicate the optical character of a water body in a generalized and systematized way, different classification schemes have been proposed. [Jerlov \(1951\)](#) was the first to establish an optical classification of marine waters based on transparency. He recognized three basic types of oceanic water (I, II and III) and nine types of coastal waters (1 to 9), in order of decreasing transmittance. [Pelevin & Rutkovskaya \(1977\)](#) proposed waters to be classified based on the diffuse attenuation coefficient at 500 nm, $K_d(500)$. According to [Smith & Baker \(1978\)](#), the classification of oceanic waters (*i.e.* not significantly influenced by terrigenous material or resuspended sediments) can be performed based on the total chlorophyll-like pigment concentration. [Kirk \(1980\)](#) classified inland waters into type G (“gelbstoff” or CDOM dominated), type T (“tripton” or inorganic particles), and type A (algae-dominated). [Prieur & Sathyentranath \(1981\)](#) proposed a similar classification also for open and coastal waters.

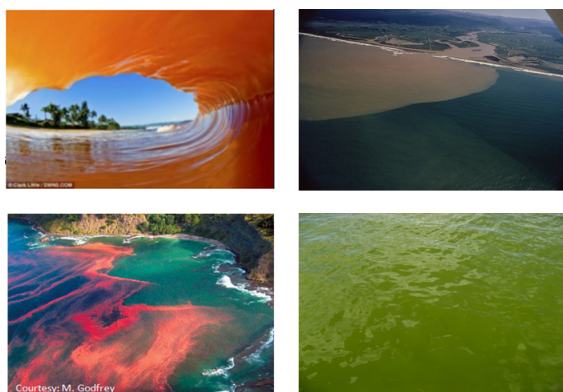


Figure 1.2: Example of waters dominated by different components: (top-left) CDOM-dominated water (source: <http://www.clarklittlephotography.com/>); (top-right) domination of suspended sediments (source: <http://www4.ncsu.edu/elleitho/>); (bottom-left) red tide (source: <http://www.whoi.edu/redtide/>); (bottom-right) Pedinophyceae bloom (source: <https://www.flickr.com/photos/myfwc/6442818691>).

The most widely used optical classification scheme is the one proposed by [Morel & Prieur \(1977\)](#), which distinguish between two basic types of oceanic waters according to optically

dominant constituents: case 1 and case 2 waters (Fig. 1.3). In case 1 waters phytoplankton and their products dominate, whereas case 2 waters are influenced not just by phytoplankton and related particles, but also by other substances, such as mineral particles and coloured dissolved organic matter not associated with phytoplankton. Thus, Case 1 waters represent the phytoplankton-dominant water environments, whereas Case 2 waters represent all other possible cases. Case 1 waters are typical of the open ocean, away from coasts and river mouths. Depending on the phytoplankton concentration, these types of waters range from very clear (oligotrophic) to very turbid (eutrophic) waters, with Chlorophyll-a concentrations from $\sim 0.02 \text{ mg} \cdot \text{m}^{-3}$ up to $5 - 20 \text{ mg} \cdot \text{m}^{-3}$, respectively. Meanwhile, case 2 waters are found in coastal zones influenced by land drainage or sediment resuspension.



Figure 1.3: Diagrammatic representation of Case 1 and Case 2 waters. Source: [Sathyendranath \(2000\)](#).

1.2.2 Optical properties of natural waters

When light reaches the water surface, it can either be reflected or enter the water. Light is reflected when the critical angle of the light reaching the atmosphere/water interface is too great. The amount of light reflected varies depending on the surface waves and on the incident angle of the sun. Light that penetrates the water surface and propagates down into the water is subject to different processes determined by the optical properties of the water body. The optical properties of waters are conveniently divided in two groups: inherent and apparent properties ([Preisendorfer 1976](#)). Inherent optical properties (IOPs) depend only upon the medium (*i.e.* on the water composition and the optical characteristics of each individual constituent) and therefore are independent of the ambient light field within the medium. IOPs include the absorption, the scattering and the attenuation coefficients, the volume scattering function and the single-scattering albedo. Apparent optical properties (AOPs) are those properties that depend both on the medium (the IOPs) and on the geometrical distribution of the ambient light field. Commonly used AOPs are the vector and scalar irradiances, reflectance, the average cosines, and the various attenuation functions (K functions). The

IOPs are easily defined but they can be difficult to measure (especially in situ), whereas the AOPs are generally easier to measure, but difficult to interpret because of the environmental effects. The link between the IOPs and the AOPs is given by the radiative transfer equation (RTE) (Fig. 1.4). Surface waves, bottom characteristics, cloud cover and angle of the incident radiance constitute the boundary conditions necessary for solution of the radiative transfer equation. This thesis focus on the IOPs and thus, a detailed description about these optical properties is provided below. Details about radiative transfer theory and equation, as well as the different AOPs, can be found in [Mobley \(1994\)](#) and [Kirk \(1994\)](#).

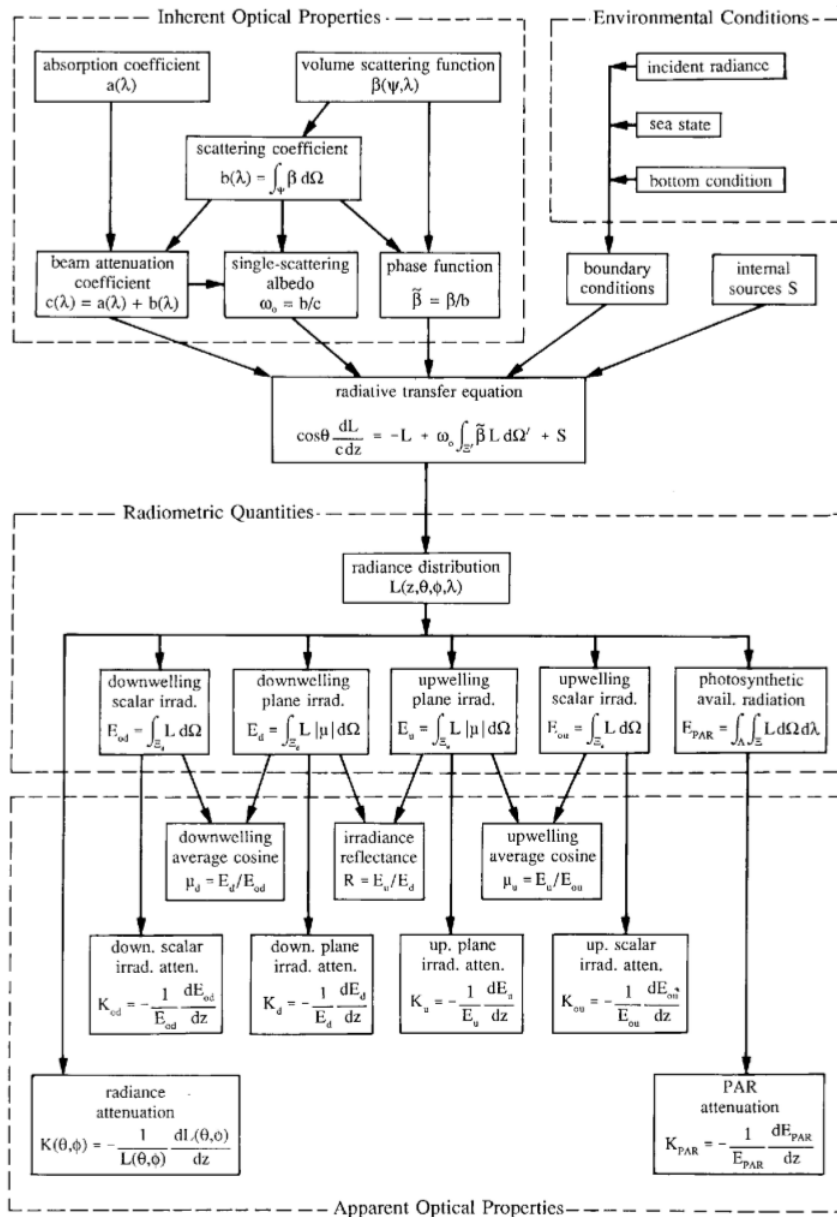


Figure 1.4: Relationships between the different quantities commonly used in hydrological optics. Source: [Mobley \(1994\)](#).

- Definition of Inherent Optical Properties

Light penetrating into the water can either be transmitted (remain unaffected) or attenuated due to the absorption (transformation into other forms of energy) and scattering (redirection) processes that take place within the water. These IOPs can be easily defined by using the schematic illustration shown in Fig. 1.5. This figure illustrates a collimated beam of monochromatic light of wavelength λ and spectral radiant power $\phi_i(\lambda)$ penetrating into a small volume (ΔV) of water of thickness Δr . Some of the incident light is absorbed, $\phi_a(\lambda)$, and some is scattered out of the beam at an angle ψ , $\phi_s(\lambda, \psi)$. $\phi_s(\lambda)$ represents the total power that is scattered into all directions. The remaining power, $\phi_t(\lambda)$, is transmitted through the volume with no changes in direction.

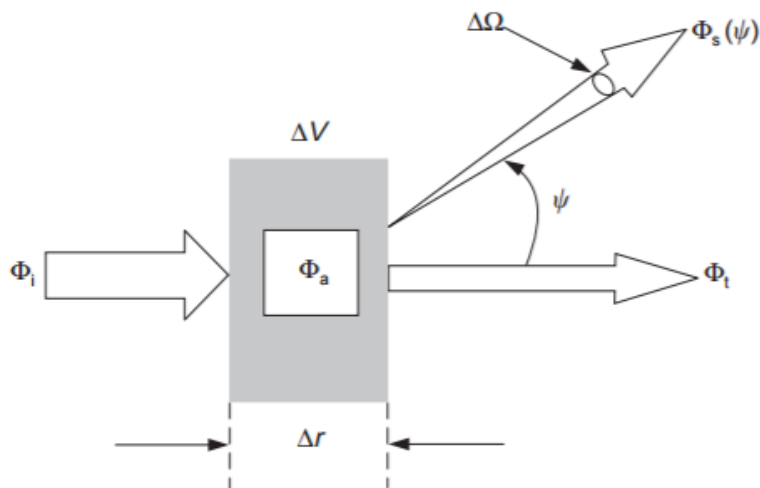


Figure 1.5: Geometry used to define the Inherent Optical Properties. Source: Mobley (1994).

The proportion of photons absorbed, $\Delta\phi_a(\lambda)/\phi_i(\lambda)$ (which correspond to the absorbance) over the small path length Δr represents the **absorption coefficient**, $a(\lambda)$.

$$a(\lambda) = \lim_{\Delta r \rightarrow 0} \left(\frac{1}{\phi_i(\lambda)} \frac{\phi_a(\lambda)}{\Delta r} \right) [m^{-1}] \quad (1.1)$$

As represented in Fig 1.5, $\phi_s(\lambda, \psi)/\phi_i(\lambda)$ is the fraction of incident flux scattered out of the beam through an angle ψ into a solid angle $\Delta\Omega$ centered on Ω . The proportion of scattered power per unit distance and unit solid angle is known as **volume scattering function** (VSF), $\beta(\psi, \lambda)$.

$$\beta(\psi, \lambda) = \lim_{\Delta r \rightarrow 0} \lim_{\Delta\Omega \rightarrow 0} \left(\frac{1}{\phi_i(\lambda)} \frac{\phi_s(\psi, \lambda)}{\Delta r \Delta\Omega} \right) [m^{-1} sr^{-1}] \quad (1.2)$$

Chapter 1

Integrating $\beta(\psi, \lambda)$ over all directions (solid angles) gives the spectral **scattering coefficient**, $b(\lambda)$, which is the total scattered power, $\Delta\phi_s(\lambda)/\phi_i(\lambda)$, per unit incident irradiance and unit volume of water.

$$b(\lambda) = 2\Pi \int_0^\Pi \beta(\psi, \lambda) \sin \psi d\psi [m^{-1}] \quad (1.3)$$

This integration is often divided into forward scattering, $0 \leq \psi \leq \Pi/2$, and backward scattering, $\Pi/2 \leq \psi \leq \Pi$, parts, being this last one the **backscatter coefficient**, $b_b(\lambda)$.

The **beam attenuation coefficient**, $c(\lambda)$, is defined as the sum of the absorption and scattering coefficients, and represents the total loss of radiant energy from the original beam.

$$c(\lambda) = a(\lambda) + b(\lambda) [m^{-1}] \quad (1.4)$$

Other commonly used IOP is the **single scattering albedo**, $\omega_0(\lambda)$, which is the probability that a photon will be scattered (rather than absorbed) in any given interaction:

$$\omega_0(\lambda) = b(\lambda)/c(\lambda) [unitless] \quad (1.5)$$

Finally, the **volume scattering phase function**, $\tilde{\beta}(\psi, \lambda)$, provides the angular distribution of the scattered light and is defined by:

$$\tilde{\beta}(\psi, \lambda) = \beta(\psi, \lambda)/b(\lambda) [sr^{-1}] \quad (1.6)$$

The inherent optical properties are conservative in nature, which implies that bulk IOPs can be expressed as the sum of the individual contributions by the different optically active components present in the water column (Bukata *et al.* 1995). Thereby, as examples, the absorption and attenuation coefficients can be written as:

$$a(\lambda) = \sum_{i=1}^n a_i(\lambda) [m^{-1}] \quad (1.7)$$

$$c(\lambda) = \sum_{i=1}^m c_i(\lambda) [m^{-1}] \quad (1.8)$$

$a_i(\lambda)$ and $c_i(\lambda)$ represent the absorption and attenuation attributed to a particular component i of the water column and n and m are the total number of absorbing and attenuating constituents, respectively.

1.2.3 Optically active constituents in water

The in-water constituents are traditionally divided into “dissolved” and “particulate” matter, of inorganic and organic origins, living and non-living. The dissolved fraction is defined as everything that passes through a filter paper of pore size $0.2 \mu m$, whereas the fraction retained on the filter comprises the particulate matter. The concentration and optical properties of these constituents vary by many orders of magnitude in oceanic waters, which implies wide variations in color from the deep blue of the open ocean to yellowish-brown in a turbid estuary. The most important optically active constituents (OACs) of sea water are described as follow.

- a) **Pure seawater:** it consists of pure water plus various dissolved salts (predominantly sodium, Na^+ , and chloride, Cl^- , ions), with an average salinity about 35 PSU. The water itself absorbs light, mainly in the red part of the spectrum (up to 600 nm) and scatter light very weakly. The presence of salts increases the scattering by about 30% relative to pure water, whereas they have a negligible effect on absorption at visible wavelengths. Nevertheless, they greatly increase the absorption at extremely long ($\lambda \geq 0.1 \text{ nm}$) wavelengths and slightly at ultraviolet wavelengths (Mobley 1994).
- b) **Chromophoric dissolved organic matter (CDOM):** it is also known as yellow substance or “gelbstoff”. It is the optically active fraction of the dissolved organic matter contained in aquatic systems, which derive from autochthonous primary production and river run-off of terrestrial organic matter. Concentrations are thus generally greatest in inland and coastal waters than in open ocean. It consists mostly of various humic and fulvic acids (Kirk 1983). This compound strongly absorbs light at ultraviolet and short visible wavelengths (blue light) and very little in the red. The scattering is negligible. CDOM is one of the major components controlling the amount of underwater UV light, especially in lakes, rivers, estuaries and coastal environments.
- c) **Particulate organic matter:** it can be divided into living (phytoplankton, bacteria and viruses) and non-living (colloids and organic detritus) organic particles.
 - **Phytoplankton:** phytoplankton are among the most significant live substances that determine the optical and biological characteristics of open ocean and coastal waters. They are microscopic plants exhibiting high diversity of size (from $2 \mu m$ (nanoplankton) to more than 2 cm (macroplankton)), shape, species, and concentration. The principal phytoplankton taxonomic groups include diatoms, dinoflagellates, coccolithophores and silicoflagellates. In coastal environments the predominant taxonomic group may be the green algae, blue-green algae and brown colored phytoflagellates (Kennish 2001). Phytoplankton are the most important

biomass producers in aquatic ecosystems and constitute the basis for the food web in the oceans. They are responsible for determining the optical properties of most oceanic (case 1) waters. Their chlorophyll and related pigments strongly absorb light in the red and blue wavelengths. Phytoplankton are also efficient scatterers of light, especially at small scattering angles, influencing significantly the total scattering properties of seawater. However, due to their relatively large size, they contribute relatively little to the backscattering coefficient. Phytoplankton require sunlight (as well as water and nutrients) for growth and reproduction, which is most abundant near the sea surface. For this reason, most phytoplankton remain in the upper part of the water column.

- **Bacteria:** living bacteria are microscopic unicellular organisms in the size range $0.2 - 2 \mu\text{m}$ in diameter, occurring in number concentrations of $10^{11} - 10^{13} \text{ m}^{-3}$. Bacteria are significant scatterers and absorbers of light, especially at blue wavelengths and in clear oceanic waters with low chlorophyll concentrations. Furthermore, bacteria are likely the most important microorganisms contributing to particulate backscatter (Morel & Ahn 1990, Stramski & Kiefer 1991).
- **Viruses:** virus particles are found in concentrations from 10^6 to $10^{15} \text{ particles} \cdot \text{m}^{-3}$ in eutrophic regions (Suttle *et al.* 1990). They would be considered dissolved matter by the traditional definition due to their small size (20 – 250 nm). These particles do not contribute significantly to the total absorption and scattering properties of natural waters, because they are inefficient absorbers and scatterers on a per particle basis (Mobley 1994).
- **Zooplankton:** they are living organisms with sizes from tens of micrometers to two centimeters. Even at large concentrations, these large particles tend to be missed by optical instruments that randomly sample only a small volume of water.
- **Colloids:** these nonliving particles contribute significantly to backscattering (*e.g.* Stramski & Kiefer 1991). They can be found in the size range $0.4 - 1.0 \mu\text{m}$ in typical number concentrations of 10^{13} m^{-3} , and colloids of size $\leq 0.1 \mu\text{m}$ in abundances of 10^{15} m^{-3} (Wells & Goldberg 1991).
- **Organic detritus:** they are nonliving organic particles of different sizes derived from phytoplankton death and zooplankton grazing. Absorption by organic detritus is maximal at the shorter wavelengths. According to Stramski & Kiefer (1991) the sub-micrometer, low-index-of-refraction, detrital particles are the major backscatterers in the ocean.

d) Particulate inorganic matter: these particles are, generally, a consequence of river discharge or seabed resuspension. They consist of finely ground quartz sand, feldspars,

calcite, clay minerals (*e.g.* illites and micas), silt or trace metals in a wide range of sizes, from much less than 1 μm to several tens of micrometers (Fig. 1.6). They significantly contribute to the optical properties of the aquatic system, especially in turbid coastal waters with high sediment load.

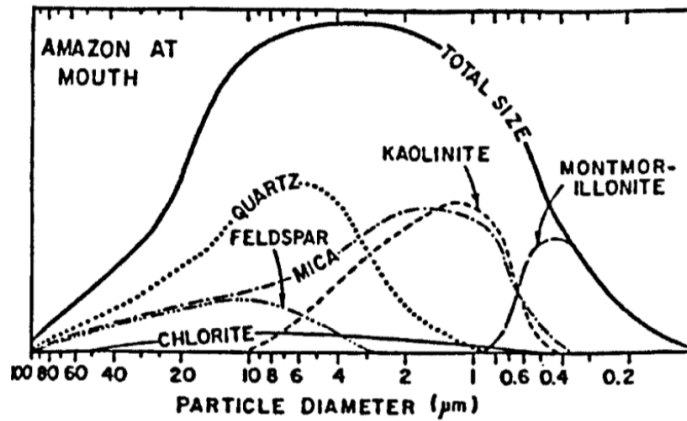


Figure 1.6: The size distribution of mineral particles transported by Amazon River. Source: Gibbs (1977).

1.2.3.1 Characteristics of particles affecting their optical properties

The optical properties of the particulate fraction are determined by the following physical characteristics: particle concentration, size, shape, composition (*i.e.* index of refraction) and, in the case of non-spherical particles, the orientation of the particle in relation to the light beam.

- Concentration: The first order source of variation in the magnitude of the absorption and scattering coefficients is the total amount of constituents in the water. In fact, both absorption and scattering are conservative properties and therefore their magnitude vary linearly with the concentration of the absorbing/ scatter material. Thereby, the component IOPs can be expressed as:

$$a_i(\lambda) = C_i \cdot a_i^*(\lambda) [m^{-1}] \quad (1.9)$$

$$b_i(\lambda) = C_i \cdot b_i^*(\lambda) [m^{-1}] \quad (1.10)$$

where C_i is the component concentration and $a_i^*(\lambda)$ and $b_i^*(\lambda)$ are the mass-specific absorption and scattering coefficients for the component i . The units on C vary depending

upon normalization of the optical property. The mass-specific optical coefficients represent an optical cross-section per unit mass in units of $m^2 \cdot g^{-1}$ and they vary with the nature of the particles.

- Composition: it is manifested by the refractive index. The complex index of refraction comprises real, n , and imaginary, k , parts:

$$m = n + ik[\text{dimensionless}] \quad (1.11)$$

The real part of the refractive index primarily determines scattering processes and is controlled by the density and composition of the particle (*i.e.* relative amounts of water, protein, calcite, quartz, etc.). The imaginary part governs absorption and, in the case of phytoplankton, depends strongly on the structure of pigment molecules. Living phytoplankton typically have low indices of refraction, in the range 1.01 to 1.09 relative to the index of refraction of pure seawater. Detritus and inorganic particles generally have high indices, in the range of 1.15 to 1.20 relative to seawater (Jerlov 1976).

- Size: The size determines not only the optical properties of the particle, but also its sedimentation rate, the encounter rate between particles, etc. In natural waters, the size of the particles relevant to optics ranges within at least eight orders of magnitude, from sub-micron particles (colloids and viruses) to centimeters (aggregates and zooplankton) (Fig. 1.7). The particle size distribution, PSD, is a widely used parameter to characterize marine particles, since it describes the relationship between particle sizes and their concentrations (Bader 1970). Numerically, small particles are much more abundant than larger particles and, consequently, the PSD in the ocean exhibits a rapid decrease in particle concentration with increasing size. In fact, PSDs in marine waters can be often well described by a power-law (Junge-like) distribution,

$$N(D) = N_0(D/D_0)^\xi \quad (1.12)$$

where $N(D)$ is the number of particles with diameter D and D_0 is a reference diameter for which the number concentration is N_0 . The exponent of the PSD, ξ , typically varies between 3 and 5 (*e.g.* Diehl & Haardt 1980, Morel 1973) and is linearly related with the exponent of the particulate attenuation spectrum (Boss *et al.* 2001a, Diehl & Haardt 1980).

- Shape: particles immersed in natural waters exhibit a wide range of shapes, from spheres to complex shapes and inhomogeneous surfaces (Fig. 1.8). Most of the theo-

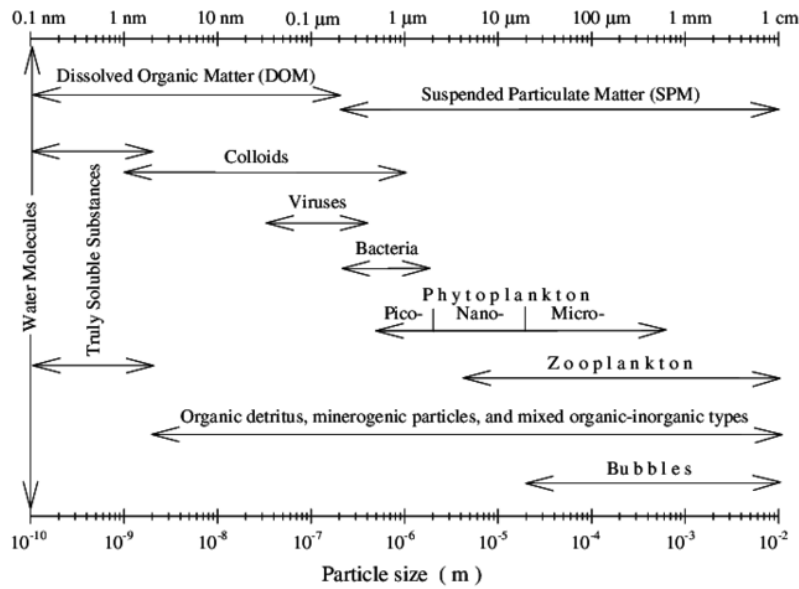


Figure 1.7: Representative sizes of different in-water constituents. Source: *Stramski et al. (2004)*.

retical investigations on the IOPs of marine particles assume that particles are homogeneous spheres and there is a good agreement between theory and measurement for such particles (*Kerker 1969*). However, only a limited number of studies have examined the IOPs of non-spherical marine particles and results indicate a strong dependence of optical properties, in particular scattering, on shape (*Aas 1984, Voss & Fry 1984*). Further studies are therefore needed to evaluate the shape effects on IOPs in the context of marine particles.

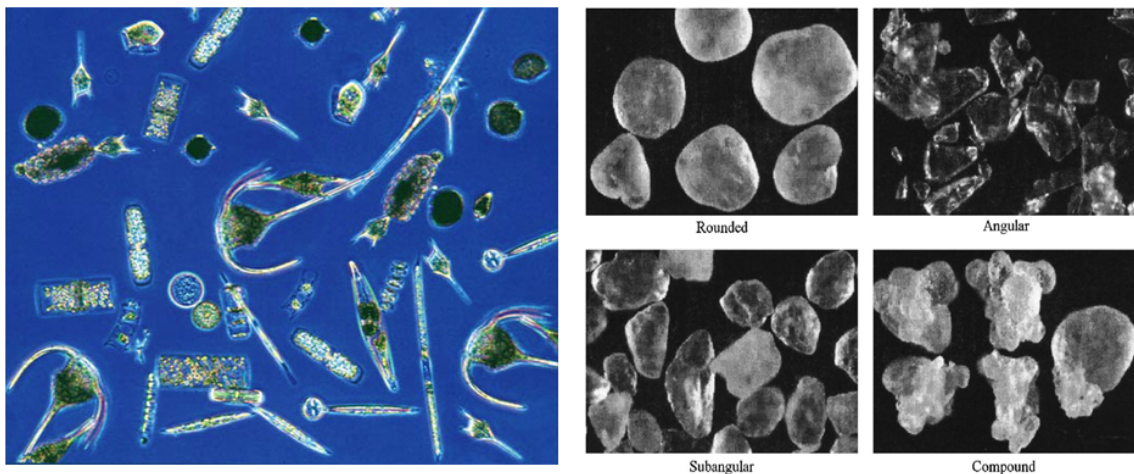


Figure 1.8: Examples of different shapes of marine particles: (left) phytoplankton particles (source: <http://actionoutdoors.org>) and (right) mineralic particles (source: *Schrotenboer & Arbogast (2010)*).

- Orientation: IOPs of non-spherical particles are strongly dependent on particle orientation (*e.g.* Asano 1979) but data on orientation of particles found in natural marine environments are roughly nonexistent. In most of the studies, a random particle orientation is assumed, which is not appropriate under certain environmental conditions (*e.g.* shear flows can result in alignment of particles with respect to the flow). Based on Mie theory for homogeneous and spherical particles, it can be partially explained the dependence of light scattering on particle size, shape and refractive index (*e.g.* Morel & Bricaud 1986). For a given wavelength, scattering by polydisperse particles tends to increase with average particle size and with the average real part of the refractive index. Furthermore, the smaller the particles, the steeper the scattering spectral slope. Phytoplankton absorption is affected by particle size and shape since these characteristics have a direct impact on the pigment package effect (which is explained below).

1.3 Inherent Optical Properties

1.3.1 Absorption properties

Pure seawater is blue because the selective absorption of red light and because of the minimum absorption in the 400 – 500 nm range. It absorbs light strongly in the infrared, where the scattering by water molecules is insignificant (Fig. 1.9). Different authors (*e.g.* Buiteveld *et al.* 1994, Smith & Baker 1981, Sogandares & Fry 1997) have measured the spectral absorption coefficient of pure water, obtaining a very good agreement in the NIR region ($\lambda > 600$ nm) but larger inconsistencies at shorter wavelengths (Pope & Fry 1997). The absorption by pure water usually is taken from Pope & Fry (1997), since they provide the most reliable data for the wavelength region 380 to 700 nm (Fry 2000). The absorption by water is dependent on temperature, with an effect less than $0.001 \text{ m}^{-1}/^{\circ}\text{C}$ throughout the visible region of the spectrum with the exception of wavelengths near 610 nm. Temperature and salinity dependencies of the absorption and attenuation by pure seawater was examined by Pegau *et al.* (1997).

The **chromophoric dissolved organic matter**, CDOM, absorbs light strongly in the ultraviolet region and thus, is usually the principal constituent that controls the penetration depth of radiation potentially harmful to organism. In coastal waters, where its concentration is usually higher than in open ocean, CDOM absorption can extend well into the visible region, often dominating the absorption by phytoplankton in the blue band of the spectrum and determining the availability of photosynthetically available radiation (PAR) (Fig. 1.10). The absorption by CDOM decreases exponentially with wavelength and is usually described by the exponential function proposed by Bricaud *et al.* (1981):

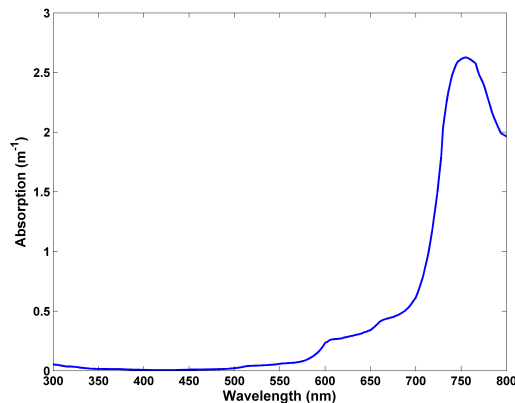


Figure 1.9: Pure water absorption spectrum taken from Pope & Fry (1997).

$$a_{CDOM}(\lambda) = a_{CDOM}(\lambda_0) \cdot \exp[-S_{CDOM} \cdot (\lambda - \lambda_0)] \quad (1.13)$$

where $a_{CDOM}(\lambda)$ and $a_{CDOM}(\lambda_0)$ are the absorption coefficients at wavelength λ and at a reference wavelength λ_0 (often chosen to be $\lambda_0 = 440$ nm), and S_{CDOM} is the spectral slope. Both the amplitude and the spectral slope of a_{CDOM} depend on the composition of the dissolved organic matter present in the water, which in turn depends on the terrestrial input, photooxidation, local microbial activity, etc. Values of S_{CDOM} vary between 0.011 and 0.035 nm^{-1} . The magnitude of CDOM absorption may vary greatly, with values at 355 nm, $a_{CDOM}(355)$, oscillating from less than 0.05 m^{-1} , in oligotrophic waters, to more than 15 m^{-1} in rivers, lakes, and coastal regions (Blough & Vecchio 2002). The absorption coefficient at 440 nm is commonly used as an indicator of the concentration of CDOM. Absorption and fluorescence are the most significant optical properties of CDOM in natural waters, whereas the scattering is considered to be insignificant.

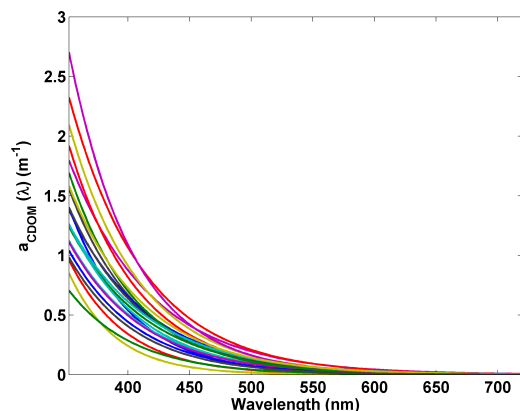


Figure 1.10: Exemplary CDOM absorption spectra measured in Alfacs Bay (NW Mediterranean) in June 2013.

Phytoplankton cells are strong absorbers of visible light, due to their photosynthetic pigments located in the chloroplasts. Pigments absorb light and transform the energy of sunlight into chemical energy through the process of photosynthesis. There are three basic types of photosynthetic pigments: the chlorophylls, the carotenoids and the biliproteins. Chlorophylls and carotenoids are present in all algal species, whereas biliproteins are additionally present in certain blue-green and red algae (Bukata *et al.* 1995). Chlorophylls are the main photosynthetic pigments in plants and include the chlorophylls (Chl) a, b, c and d. Chlorophylls have two major absorption bands (in the blue and in the red), whereas the absorption in the green is minimum. Chlorophylls -a and -b exhibit an absorption peak in the red region of the spectrum (~ 675 nm for chl-a and ~ 650 nm for chl-b), and a stronger absorption band in the blue wavelengths (~ 440 nm for chl-a and ~ 460 nm for chl-b). Meanwhile, chl-c absorbs strongly in the blue region and exhibits a smaller absorption maxima at larger wavelengths (~ 580 and ~ 630 nm). Carotenoids display absorption peaks mainly in the spectral region between 450 nm to 550 nm. They include α -carotene, β -carotene, diadinoxanthin, fucoxanthin, diatoxanthin, peridinin, etc. The biliprotein pigments are divided into three classes, the phycoerythrins - phycoerythrocyanins, the phycocyanins, and the allophycocyanins. The main absorption by biliproteins occur between 480 – 600 nm (Fig. 1.11).

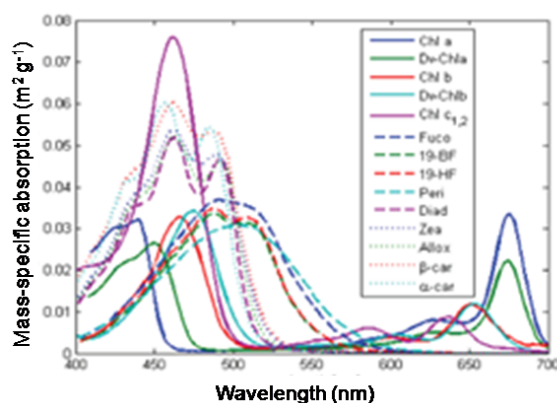


Figure 1.11: Absorption spectra of individual photosynthetic pigments in solvents. Pigment abbreviations are: Chl a = monovinyl chlorophyll-a, Dv-Chla = divinyl chlorophyll-a, Chl b = monovinyl chlorophyll-b, Dv-Chlb = divinyl chlorophyll-b, Chl c1,2 = chlorophyll c1 + c2, Fuco = fucoxanthin, 19-BF = 19'-butanoloxyfucoxanthin, 19HF = 19'-hexanoyloxyfucoxanthin, Peri = peridinin, Diad = diadinoxanthin, Zea = zeaxanthin, Allox = alloxanthin, β -car = beta carotene, α -car = alpha carotene (Source: ftp://misclab.umeoce.maine.edu).

Different species of phytoplankton contain specific pigment composition and in different proportions, which determine their spectral absorption characteristics. The accessory pigments (*i.e.* pigments that improve light energy absorption, but they are not a primary part of photosynthesis, such as biliproteins and caretonoids) are responsible for specific organism colors, such as yellow, red, blue and brown. In this way, diatoms are usually yellow, yellow-brown due to xanthophyll (fucoxanthin and diatoxanthin) carotenoids. Dinoflagellates contain peridinin

Chapter 1

carotenoid pigment, which determine the reddish color. Coccolithophorids are also yellow, yellow-brown cells. They are distinguished by special calcium carbonate plates (called coccoliths) which confer a milky turquoise color on the seawater. Green algae have chl-a and chl-b as dominant pigments.

Since chlorophyll occurs in all photosynthetic plants, its concentration is commonly used as the optical measure of phytoplankton abundance. In practice, the term “chlorophyll concentration” (in milligrams per cubic meter of water) refers to the sum of chl-a and the related pigment pheophytin a. Chlorophyll concentrations oscillate from $0.01 \text{ mg} \cdot \text{m}^{-3}$ in the clearest waters, to more than $100 \text{ mg} \cdot \text{m}^{-3}$ in eutrophic estuaries or lakes (Mobley 1994). Variations in the absorption properties of phytoplankton result from the combined influences of the pigment composition and the so-called “pigment package effect”. The latter is a major source of both inter- and intra-species variability, derived from the localized distribution of the absorbing pigments within the phytoplankton cells. Thereby, pigments are localized into small “packages” called chloroplasts, which are non randomly distributed throughout the cell. The package effect depends on the cell size and on physiological state (which, in turn, varies depending on environmental factors such as ambient light and nutrient availability). In addition, phytoplankton have the ability to increase the amount of light collectors (*i.e.* chlorophyll molecules) at low light conditions, which allow growth rates to be higher than would otherwise be at such conditions. This physiological adaptation to ambient light conditions is known as photoadaptation.

The absorption by **non-pigmented particulate matter** is characterized by increasing exponentially with decreasing wavelength (Fig. 1.12). Thereby, the spectral shape is similar to that of CDOM and the absorption coefficient can be fitted to the exponential model (Roesler *et al.* 1989):

$$a_{npp}(\lambda) = a_{npp}(\lambda_0) \cdot \exp[-S_{npp} \cdot (\lambda - \lambda_0)] \quad (1.14)$$

where $a_{npp}(\lambda)$ and $a_{npp}(\lambda_0)$ are the non-pigmented particulate absorption coefficients at wavelength λ and a reference wavelength λ_0 (often $\lambda_0 = 400 \text{ nm}$). S_{npp} is the absorption spectral slope. Non-pigmented particulate matter includes non-living organic (such as detritus) and inorganic particles (such as fine clay, silt particles, sand, iron and manganese hydroxides and calcium carbonate (Bukata *et al.* 1995)).

1.3.2 Scattering properties

Scattering in natural waters is caused both by small scale ($\ll \lambda$) density fluctuations attributable to random molecular motions and by large ($> \lambda$) organic and inorganic particles

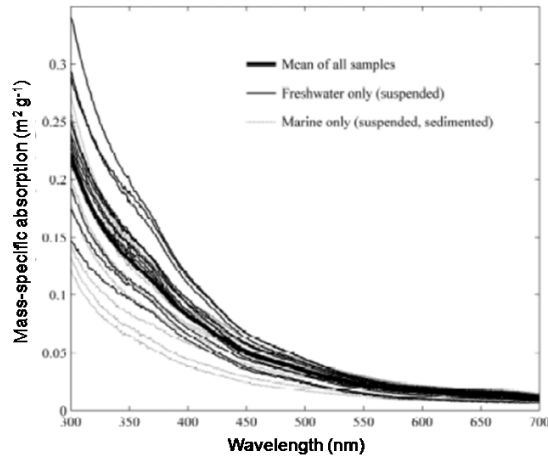


Figure 1.12: Exemplary mass-specific absorption spectra of non-algal particles. (Source: [Estapa et al. \(2012\)](#)).

([Mobley 1994](#)). These density fluctuations are associated with fluctuations in the index of refraction, and the interaction of the radiation field with these inhomogeneities gives rise to scattering. The presence of dissolved salts (salinity, $S = 35 - 39$ PSU) increase the scattering coefficient of pure seawater about 30% respect to the pure water, because of the larger index of refraction fluctuations resulting from random fluctuations in the concentrations of the various ions (Cl^- , Na^+ , etc). Because of the random orientation of water molecules, scattering by water itself and its dissolved constituents is isotropic (*i.e.* the probability of forward and backward scattering are equal). This molecular scattering is strongly wavelength dependent ($b \sim \lambda^{-4.3}$) (Fig. 1.13) and decreases as decreasing temperature. Scattering by pure seawater is important only in the very clearest natural waters, since scattering by particles is much more efficient than molecular scattering. The water scattering contribution to total backscattering ($b_b = 0.0015b + 0.5b_w$) is most likely to be significant at blue wavelengths.

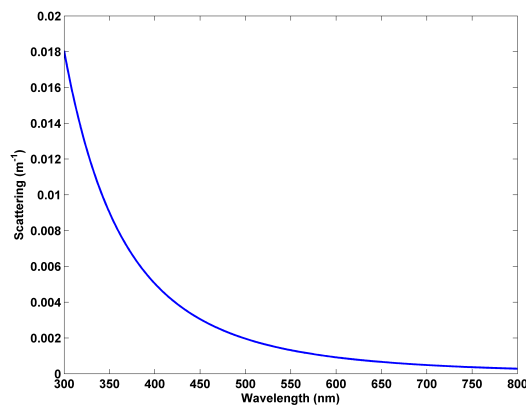


Figure 1.13: Scattering coefficient for pure seawater derived from [Morel \(1974\)](#).

Coastal waters environments are typically characterized by a higher scattering than open oceanic, oligotrophic waters, mainly due to the larger concentration of particles (organic particulate matter, terrigenous particles, minerals and re-suspended sediments) (Kirk 1983). In contrast to the volume scattering function of pure water (which is symmetric), the volume scattering functions measured in natural waters are highly peaked in the forward direction (Fig. 1.14). This is because scattering is dominated by diffraction from polydisperse particles that are usually much larger than the wavelength of visible light. Scattering by refraction and reflection from particle surfaces becomes important at large scattering angles ($\psi > 15^\circ$, where ψ is the scattering angle). Particles cause at least a four-order-of-magnitude increase in scattering between $\psi \approx 90^\circ$ and $\psi \approx 1^\circ$. Thus, the contribution of molecular scattering to the total is completely negligible except at backscattered directions ($\psi \geq 90^\circ$) in the clearest natural waters (Morel & Gentili 1991).

Regarding the spectral behavior of the scattering coefficient, particulate matter scatters the shorter wavelengths more intensely than longer wavelengths (Morel 1973). For weakly absorbing particles, the scattering is a smoothly varying function of wavelength, where the slope of which is related to the particle size distribution and the magnitude is a function of the concentration and the real index of refraction (Fig. 1.14). For strongly absorbing particles such as phytoplankton, the scattering spectra exhibit minima near the absorption peaks due to anomalous dispersion (Morel & Bricaud 1981, Van de Hulst 1957, Zaneveld & Kitchen 1995). The light scattering behavior of spherical particles of any size is explained in Mie (1908). Detailed measurements and explanation of the volume scattering function of different natural waters can be found in Petzold (1972).

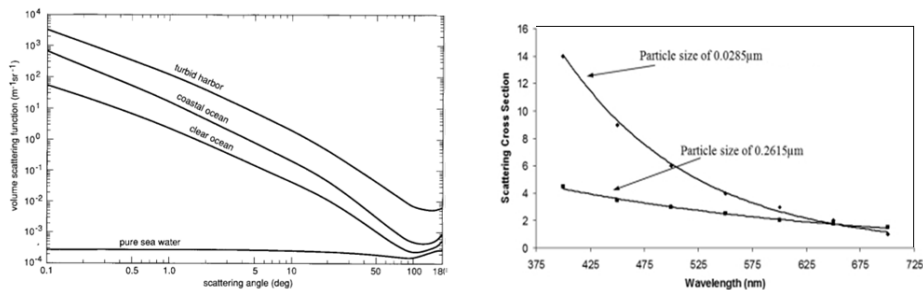


Figure 1.14: (left) Measured volume scattering functions from three natural waters with different particle load (Petzold 1972) and the computed volume scattering function for pure sea water, all at $\lambda = 514$ nm. Source: Mobley (1994). (right) Scattering cross section *vs* wavelength for two different particle sizes. Source: Omar & Matjafri (2009).

1.3.3 Attenuation properties

The beam attenuation is decomposed to the attenuation by particles, dissolved material, and the water itself. Most of the studies focused on the particulate attenuation, which is

determined by measuring the water sample previously filtered through $0.2 \mu\text{m}$ nominal pore size. The particulate attenuation, $c_p(\lambda)$, is observed to be a smoothly varying function of wavelength (*e.g.* Boss *et al.* 2001a, Voss 1992), which can be well described by the following hyperbolic function:

$$c_p(\lambda) = c_p(\lambda_0) \left(\frac{\lambda}{\lambda_0} \right)^\gamma \quad (1.15)$$

where γ is the hyperbolic slope. Nevertheless, it is important to take into account that deviations from its theoretical behavior -associated with absorbing particles- have been reported by several authors (Bricaud & Morel 1986, Zaneveld & Kitchen 1995). While the magnitude of the particulate attenuation is directly linked to the particulate matter concentration in the ocean (*e.g.* Gardner *et al.* 1993, McCave 1983), its shape (*i.e.* spectral slope) is highly correlated with the slope of the particle size distribution (*e.g.* Boss *et al.* 2001a).

1.3.3.1 Measurements of bulk and constituent-specific absorption and scattering coefficients

In situ measurements of inherent optical properties provide information on the presence, concentration and composition of the optically active constituents in water. Thereby, it is possible to estimate variables such as chromophoric dissolved organic matter (CDOM), nitrate and total suspended matter concentration, organic carbon or chlorophyll-a based on these measurements (*e.g.* Twardowski *et al.* 2005). However, this estimation is not straightforward since in situ (bulk) IOPs measurements provide a measure of the sum of the different contributions of individual components present in water. Thus, it is necessary to partition the bulk IOPs into constituent-specific optical properties. Because it is impossible to measure the IOPs of each individual constituent, they are grouped into operational components based on the spectral similarity of their IOPs or on analytic definitions. In this way, absorption is operationally separated into dissolved and particulate components by means of the nominal pore size of a filter (typically $0.2 \mu\text{m}$ to $0.7 \mu\text{m}$, respectively). Thereby, the absorption by dissolved material (*i.e.* CDOM) is determined by measuring the water sample previously filtered through $0.2 - \mu\text{m}$ pore size filters. The absorption by particulate material is further separated into phytoplankton and non-algal particles (NAP), the division of which is performed by means of the laboratory-based filter pad technique applied to discrete water samples. The total particulate matter is chemically depigmented and scanned, and the difference between the total particulate absorption and the depigmented particle absorption is the *in vivo* absorption by phytoplankton pigments (Ducha & Kubin 1976, Roesler & Perry 1995). The extraction of the pigments on the filter pad is performed with a strong polar solvent such as methanol or with oxidation by bleach on the filter. The non-algal particulate

matter comprises the non-pigmented portion of phytoplankton cells, bacteria and zooplankton, detritus and mineralic and biogenic inorganic particles. In regions with high mineralic particle concentrations, the partition of NAP absorption into organic and inorganic components has proven difficult due to their spectral similarity within the visible range (Babin & Stramski 2002, Stramski *et al.* 2001). On the other hand, measurements of the scattering coefficient provide the scattering by particles since the dissolved fraction not contribute to scattering (it does not contain particles). Unfortunately, there is not currently available any technique to partition the particulate scattering into organic and inorganic components. The scattering coefficient is commonly obtained by simply subtracting the absorption from the beam attenuation coefficient (*e.g.* Babin *et al.* 2003).

1.4 Optical sensors: IOPs devices

In contrast to AOP devices, IOP sensors use a light source of defined intensity, angular distribution, and spectral bandwidth (Roesler & Boss 2008). This, in turn, allows to derive absolute coefficients and allows these instruments to be used at any time of day, without being subject to variable cloud cover, surface conditions, ship shadows and other issues sometimes associated with AOP measurements. IOP devices measure over relatively short pathlengths and can resolve in-water variability at scales ranging down to a few centimeters (Twardowski *et al.* 2005). With the exception of turbidity meters and transmissometers, most commercial IOP devices were developed relatively recently.

1.4.1 Transmissometers

Transmissometers (or beam attenuation meters) are instruments relatively simple to build and operate and generally do not require sophisticated data correction schemes (Gibbs 1974). Therefore, they have been in use for more than forty years, since the early 1970s, when the first commercial transmissometers became available (Bartz *et al.* 1978, Petzold & Austin 1968). These instruments are conceived to measure the intensity loss of a near-parallel light beam along a defined path length in the water sample, as a consequence of light absorption and scattering processes (Jerlov 1976). The drop in intensity is converted to the beam attenuation coefficient with the equation (*e.g.* Jerlov 1978):

$$c = -\frac{1}{r} \ln(I/I_0) \quad (1.16)$$

where I_0 and I are the light intensity at the source and at the receiver respectively, and r is the instrument path length (in meters). In practice, it is difficult to determine I_0 without a separate reference detector. For this reason, the beam transmission is commonly calculated

Chapter 1

relative to a reference medium, which in oceanography is ultrapure water. Thus, I_0 corresponds to the light transmission through ultrapure water sample and c is the attenuation by all water constituents except water itself.

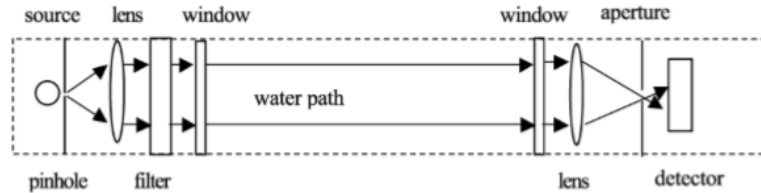






Figure 1.15: Transmissometer design with a collimated optical system. Source: [Pegau *et al.* \(2003\)](#).

Early transmissometer designs include that developed by [Petzold & Austin \(1968\)](#) which led to the Martek transmissometer, and a design developed by [Bartz *et al.* \(1978\)](#) which later became the SeaTech transmissometer. Both transmissometers measured in a single spectral band (in the photopic band and at 660 nm, for the Martek and SeaTech, respectively). They used different optical designs, with a cylindrically limited system in the case of Martek and a collimated light in the case of SeaTech. In the collimated light source all the rays of light in the beam are parallel whereas in a cylindrically limited system the measurement path is traversed by all rays which can be drawn between the projector and receiver apertures (see [Austin & Petzold 1977](#)). Transmissometers now exist that operate at single wavelengths, multiple wavelengths, and hyperspectrally ([Moore *et al.* 2009](#)). Table 1.1 describes the most currently used commercial transmissometers and their characteristics. Additionally, another hyperspectral transmissometer has been recently developed by TriOS (GmbH.), which is the focus of interest in this thesis due to its distinct characteristics such as cost-effectiveness, compactness, etc. This instrument will be described in detail in the next chapter.

Table 1.1: Most commonly used commercial transmissometers and their characteristics.

Transmissometer	Manufacturer	Light source	Spectral band	Band width (FWHM)	Path length	Receptor acceptance angle	Comments
Sea Tech	Sea Tech Inc.	LED	660 nm	25 nm	20 cm	< 30millirad	
C-Star	WET Labs	LED	Single wavelength: 370, 470, 530 or 650 nm	20 nm	10 or 25 cm	1.1954°	
LISST	Sequoia Scientific, Inc.	Collimated laser beam	670 nm	-	5 cm	0.0269°	It also measures the near-forward scattering at 32 angles
AC-9	Wet Labs	Tungsten lamp	Multispectral (9 wavelengths): 412, 440, 488, 510, 532, 555, 650, 676, 715 nm	10 nm	10 or 25 cm	0.93°	Double cuvette spectrophotometer to measure both the absorption and attenuation coefficients
AC-S	Wet Labs	Tungsten lamp	Hyperspectral (400 to 750 nm), with 5nm resolution	14-18 nm	10 or 25 cm	0.93°	
 <p>Sea Tech transmissometer</p>		 <p>C-Star 10 cm (left) & 25 cm (right) path length</p>		 <p>LISST 100X (Sequoia Scientific, Inc.)</p>		 <p>WET Labs AC-9 (left) & AC-S (right)</p>	

1.4.2 Absorption meters

The underwater absorption meters are generally still based upon a transmittance measurement. However, since the absorption coefficient is associated with losses due only to absorption processes, the conceptual framework behind these instruments is based on minimizing measurement losses due to scattering. There are a few different design approaches of modern absorption meters. The most common design for in situ measurements consists of a collimated beam propagating through a fixed path surrounded by a reflective tube and impinging upon a large area detector (Moore *et al.* 1992). The reflective tube and the wide area detector serve to collect the transmitted light as well as light that is scattered by particles in the near forward direction. Commercial instruments with this design include the multispectral ac-9 and the hyperspectral ac-s (from WET Labs) (Table 1.1). The Point Source Integrating Cavity Absorption Meter (PSICAM) is another commercial absorption meter for laboratory measurements. It was developed by Fry *et al.* (1992) and improved by Kirk (1997). It uses an integrating cavity sphere which is filled with the water sample. The principle is based on multiple reflection and scattering, and thus the extension of the path length. This inherently provides a reduction of scattering effects on absorption because the light field is already diffuse inside the cavity (*e.g.* Röttgers & Doerffer 2007). Finally, a very stable and accurate absorption meter for laboratory measurements of CDOM absorption is the liquid waveguide capillary cell (LWCC) (from WPI), which is a fiber optic cell that combine an increased optical pathlength (50 – 500 cm) with small sample volumes (*e.g.* D'Sa *et al.* 1999). Other commercial available absorption meters include the in situ spectrophotometer a-sphere (Hobi Labs) or the hyperspectral integrating cavity absorption meter OSCAR (TriOS GmbH).

1.4.3 Scattering meters

Scattering sensors measure over certain spectral and angular regions of the VSF. Turbidity sensors are among the most common optical sensors, and are widely available for ocean based applications. These instruments generally measure the optical scattering around 90 degrees from the primary beam axis of propagation (Greenberg *et al.* 1992). Among the most common commercial backscattering meters can be distinguished those developed by WET Labs. The ECO BB-9 measures the optical backscattering at nine different wavelengths and at a single angle (117 degrees). In contrast, the ECO-VSF measures the optical scattering at three different angles in the backward direction (at 100, 125, and 150 degrees) and at a single wavelength (470 nm, 530 nm, or 660 nm). In addition, the Particle Size Analyzer LISST (from Sequoia Scientific Inc) measures the near-forward-scattering at 32 logarithmically spaced angles from which it is possible to invert for particle size distributions (Agrawal 2005)(see Table 1.1).

Chapter 1

2

Characterization of advanced-technology transmissometers: performance and uncertainty analyses

The VIS-Photometer VIPER, from TriOS GmbH, is a recent commercially available transmissometer which presents distinct advantages such as cost-effectiveness, hyperspectral resolution, easy-to-handle and low power consumption. These distinct characteristics have been achieved by incorporating technologies such as micro-spectrometers as detectors and LEDs as light source. The lack of previously published works related to this instrument involves that the instrument uncertainties and the reliability of these measurements should be determined before its deployment in oceanographic applications.

Thereby, the operation of this transmissometer is examined in the present chapter, by analyzing experimental uncertainties related to the instrument stability, the effect of ambient light and derived temperature and salinity correction factors. Results identify some issues related to the thermal management of the LEDs and the contamination of ambient light. Furthermore, the performance of VIPER is validated against other transmissometers through simultaneous field measurements. It is demonstrated that VIPER provides a compact and cost-effective alternative for beam attenuation measurements in coastal waters, but it requires the consideration of several optimizations. Based on our measurements, several points of interest for future users and sensor development are discussed.

This chapter corresponds to the published article: *Ramírez-Pérez M, Röttgers R, Torrecilla E, Píera J. Cost-Effective hyperspectral transmissometers for oceanographic applications: performance analysis. Sensors 2015; 15: 20967-20989. doi:10.3390/s150920967.*

2.1 Introduction

As it was previously mentioned, optical data are a powerful tool for studying coastal ocean ecology and dynamics, since they provide essential information about particulate concentration (Campbell & Spinrad 1987, Spinrad *et al.* 1983, Zaneveld 1973), particle size distribution (Baker & Lavelle 1984, Boss *et al.* 2001a, Diehl & Haardt 1980) and composition (Astoreca *et al.* 2012, Boss *et al.* 2007), primary production (Lee *et al.* 2011), and water column turbidity (Gazzaz *et al.* 2013). Advances and progress in optical sensors technology, as well as in ocean observing platforms have increased the quantity and variety of optical observations, which have greatly extended their sampling capabilities in time and space. It consequently involves a higher ability for better understanding and quantifying many physical, biological, and chemical oceanographic processes (Dickey & Falkowski 2002). In the case of optical transmissometers (or beam attenuation meters), which are the focus of this thesis due to their general availability and simplicity of both operation and data processing, the technological advances have resulted in high spectral resolution, cost-effective, low power and compact instrument characteristics. These instruments are conceived to measure the intensity loss of a near-parallel light beam along a defined path length in the water sample, as a consequence of light absorption and scattering processes (Jerlov 1976). Transmissometers typically include a light source and a co-aligned photometer at the two ends of the optical path. The design is theoretically simple but it requires the accurate and robust alignment of the light transmitter and detector (Pegau *et al.* 2003).

Transmissometers with hyperspectral resolution allow to exploit all the spectral information contained in the beam attenuation coefficient and to carry out spectral shape analysis. Additionally, the use of modern technologies in the lighting and detection systems has contributed to the development of cost-effective and compact transmissometers. The use of light emitting diodes (LEDs) as light sources offer numerous advantages compared to traditional alternatives such as tungsten bulbs: increased lifetime, lower cost, reduced power consumption, higher brightness, flexible configuration, smaller size, and a wider choice of spectral ranges (Stojanovic & Karadaglic 2007, Yin *et al.* 2013). Furthermore, the LEDs output is stable for different orientations in contrast to the traditional lamps, for which the effective output can slightly vary depending on the position of the filaments relative to the collimation pinhole.

The use of a set of different LEDs to emulate the full visible light spectrum as well as a miniature photodiode array detector has enabled the combination of these capabilities (*i.e.* hyperspectral resolution, compact and low power) in the same transmissometer. This property might be important for cost-effective and widespread use in monitoring campaigns. However, the potential advantage of this setup remains to be explored since there are few field studies that employ hyperspectral transmissometers with this novel LED configuration.

An example of a transmissometer with these characteristics is the recently developed VIS-photometer VIPER, from the German manufacturer TriOS GmbH. Because none bibliography related to this instrument has been found, this chapter seeks to analyze the VIPER performance by examining the instrument uncertainties and by comparison with other transmissometers.

2.2 Material and Procedures

2.2.1 Instrument description

Advances in core photonics and optical instrumentation have led to the development of submersible transmissometers that use LEDs as light source and photodiode arrays as detector with hyperspectral resolution. One such commercially available model is the VIS-Photometer VIPER from TriOS GmbH (Fig. 2.1).

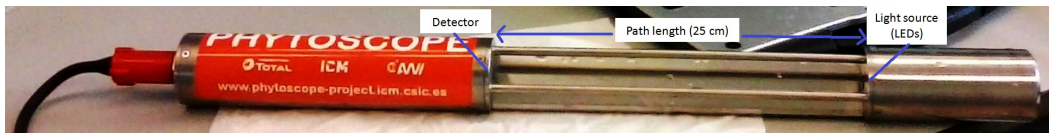


Figure 2.1: Hyperspectral VIS-Photometer VIPER (TriOS GmbH), path length of 25 cm.

Due to the limited range of the LEDs emission spectrum, this instrument combines light from five LEDs with different peak wavelengths to emulate a white-light spectral beam (Fig. 2.2). The light beam is collimated with a lens system of three lenses and a pinhole, providing a divergence angle of the beam of 1.33° (pers. comm. TriOS GmbH). The detector is a CMOS array covering the spectral range of 360-750 nm with a spectral resolution of 1.88 nm/pixels and an effective optical resolution of 15 nm (defined by the FWHM). According to the manufacturer, the detector optics provides a light acceptance angle of 0.8° (pers. comm. TriOS GmbH). The path length of the VIPER instrument employed in this study is 25 cm, with a manufacturer rating of suitable attenuation coefficients in the range between $0.04 m^{-1}$ and $9.2 m^{-1}$ (TriOS brochure 2014). VIPER has an open-path design, which avoids the use of a flow tube and an external pump.

In addition, VIPER is light-weight and relatively easy to handle for field operations, since the instrument has no internal memory or batteries.

2.2.1.1 Principles of operation

VIPER measurements are directly influenced by ambient light since this instrument does not use a flow-tube to optically isolate the sample from the surrounding medium (Pegau *et al.* 2003). This influence cannot be compensated by using intensity modulation because of the

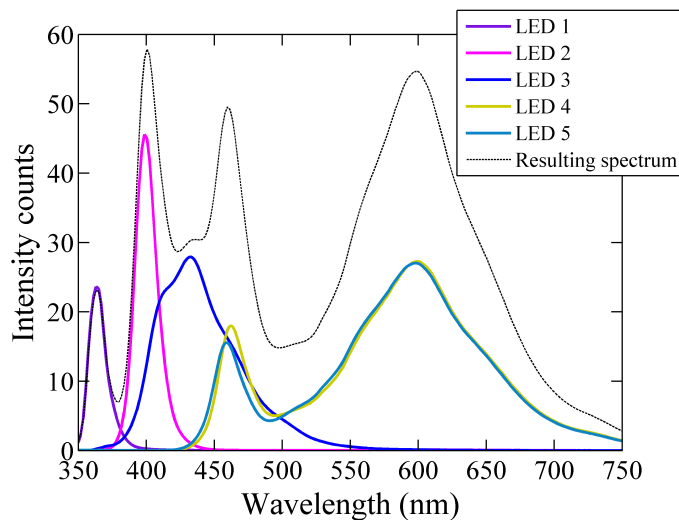


Figure 2.2: Individual light emission spectra of the 5 LEDs used by VIPER. The emission peak wavelengths, λ_p , are 365 nm, 400 nm, 430 nm, 600 nm and 600 nm for the LED 1 to LED 5, respectively. The dashed line represents the final emission spectrum (combination of the 5 LEDs).

employed type of detector. For this reason, two consecutive measurements of the intensity signal, V , are required to correct for ambient light effects. A first signal, V_D , is measured with the light source switched on. A second signal, V_D^{dark} , is obtained with the light source switched off. V_D^{dark} measures the light intensity induced by the ambient light alone. The latter signal is subtracted from the first, thereby the dark current of the detector is removed as well,

$$V(\lambda) = V_D(\lambda) - V_D^{dark}(\lambda) \quad (2.1)$$

$V(\lambda)$ is the final light intensity measurement. The intensity counts are converted into physical units by normalizing by both the maximum number of bits, 216^{-1} , and the maximum integration time (IT), 8192 ms. Although the IT can be manually selected, typically it is automatically adjusted by the instrument,

$$\Phi_{uncorr}(\lambda) = [V(\lambda) \cdot 8192] / [(216 - 1) \cdot IT] \quad (2.2)$$

$\Phi_{uncorr}(\lambda)$ is the spectrum converted to physical units. A temperature correction for the LED output is then applied to obtain the calibrated spectrum, $\Phi_T(\lambda)$,

$$\Phi_T(\lambda) = \Phi_{uncorr}(\lambda) / corr_factor(\lambda) \quad (2.3)$$

where $corr_factor(\lambda)$ is the correction factor for the LED temperature. Its wavelength dependence was fitted to a quadratic function by the manufacturer:

$$corr_factor(\lambda) = 1 + c_1(\lambda) \cdot (T_{LED} - T_{ref}) + c_2(\lambda) \cdot (T_{LED} - T_{ref})^2 \quad (2.4)$$

where c_1 and c_2 are the wavelength-dependent coefficients provided by the manufacturer in a calibration file; T_{LED} is the temperature of the LEDs, which is measured by the instrument with an internal temperature sensor, and T_{ref} is the reference temperature recorded during the calibration, $20^\circ C$ in this case. The beam transmittance, $T(\lambda)$, is calculated as the ratio between the flux transmitted to the detector and the flux entering to the water at the source window (Pegau *et al.* 2003). In practice, it is difficult to determine the absolute photon flux without a separate reference detector. For this reason, the beam transmission is calculated relative to a reference medium, $\Phi_{ref}(\lambda)$ (ultrapure water for oceanography):

$$T(\lambda) = \Phi_T(\lambda)/\Phi_{ref}(\lambda) \quad (2.5)$$

Thereby the attenuation by all water constituents except water itself, $c(\lambda)$, is determined as:

$$c(\lambda) = -\ln T(\lambda)/r \quad (2.6)$$

where r is the instrument's path length in meters and $c(\lambda)$, the beam attenuation in m^{-1} .

2.2.2 Uncertainty assessment of the measurement system

A proper instrument operation requires a prior knowledge about potential sources of uncertainty. In the case of LED-based hyperspectral open-path transmissometers, uncertainties may derive from different sources (Fig. 2.3).

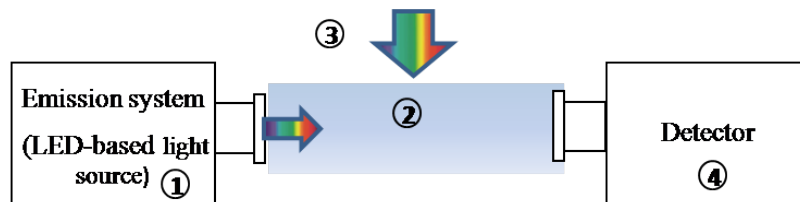


Figure 2.3: Sources of uncertainties in LED-based hyperspectral open-path transmissometers: 1) Instrument stability; 2) Temperature and salinity dependence of attenuation by water; 3) Effect of ambient light; 4) Temperature sensitivity of the detector and stray light effects.

- 1 .- A proper instrument operation demands that lighting and detection systems must be stable over time. This stability depends directly on mechanical, electronic, electrical,

thermal and optical characteristics of the instrument. The thermal management of the LED light source is one of the most critical factors concerning this issue (Lee et al., 2010; Del Lago et al., 2012). The performance of a LED is significantly dependent on temperature, which implies a proper heat dissipation and temperature compensation for a good reproducibility of operation. For compensation purposes, the LED temperature is measured by an internal temperature sensor and used to correct the collected spectra by means of correction coefficients provided in a calibration file (Eq. 2.4). Other optical sensors, such as the absorption meter a-Sphere (Hobi Labs), employ a cost-intensive system to regulate the temperature of the LEDs. In this case, the temperature of the light source is set to a specific value by heating/cooling the system (HOBILabs 2011).

- 2 .- $c(\lambda)$ is calculated relative to a reference medium (*i.e.* pure water), which is assumed to have constant optical properties. However, it is well known that $c(\lambda)$ of pure water depends on temperature and salinity, so these effects have to be corrected by including them in wavelength-dependent correction factors (Pegau et al. 1997, Röttgers et al. 2014b, Sullivan et al. 2006). Temperature and salinity also induce changes in the real part of the refractive index of both water and the glass material of the sensor's optical windows (*i.e.*, light source and detector windows). For this reason, these correction factors are specific for each instrument.
- 3 .- In open-path transmissometers, the ambient light field is assumed to remain constant within the time period between light and dark measurements. In this way, the effect of the ambient light is subtracted from the transmitted flux. This approach, however, may have problems under high-frequency variability of the ambient light (Pegau et al. 2003) especially when dealing with emission light spectra that are not spectrally flat. In these cases, the sensitivity to ambient light may result stronger and wavelength dependent.
- 4 .- A well-calibrated hyperspectral array-based spectrometer requires a detailed characterization of technical issues such as the temperature sensitivity and the spectral stray light. The VIPER's detector is a micro-spectrometer from Hamamatsu Photonics K.K. The technical specifications of this model can be found in the corresponding datasheet (Hamamatsu 2014). For this reason, these uncertainties have not been analyzed in the present research.

2.3 Assessment

2.3.1 Instrument stability

2.3.1.1 Instrument precision

The stability of the VIPER output signal was analyzed in the laboratory. With this purpose, measurements of light intensity were collected in air for one hour. Similarly to Sabbah *et al.* (2010), the precision of the measurement was determined by calculating the standard deviation within one-minute intervals (approximately 15 readings). The results obtained at the peak wavelengths of the different LEDs are shown in Fig. 2.4. Typically, all light sources require a warm-up period to reach a stable output, which was about 10 minutes in the case of VIPER. After this period, the signal became more stable at all examined wavelengths, leading to a minimum standard deviation of $c(\lambda)$ of 0.02 m^{-1} at 700 nm and a maximum value of 0.04 m^{-1} at 430 nm.

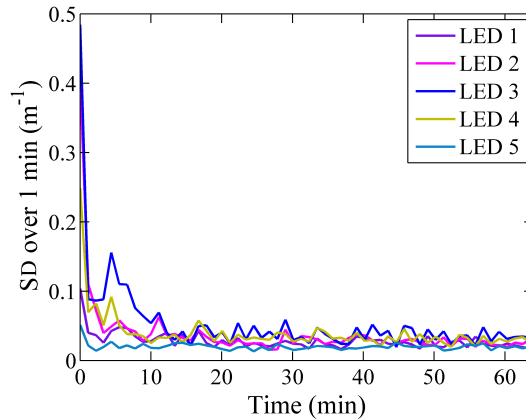


Figure 2.4: Stability of the VIPER output signal over one hour. Given is the standard deviation of the attenuation coefficient for 15 consecutive measurements (one minute) collected in air.

2.3.1.2 Thermal management

The dependency of the fully corrected output signal on the temperature of the LEDs was examined within the temperature range from 18°C to 35°C . With this aim, the instrument was immersed in purified water at different water temperatures and after the warm-up period, the transmitted light was recorded continuously for a couple of minutes. Data were corrected for both, LED-temperature effects and water temperature dependencies (see details in Section 2.3.2.1). The variability in the corrected transmitted light with the operating temperature of the LEDs was fitted with a simple linear regression model (Fig. 2.5a-e). In addition, the standard deviation was calculated in order to quantify this effect (Fig. 2.5-f). The results showed that, regardless of the LED-temperature correction (Eq. 2.3 and 2.4), the light

intensity decreased with increasing operating temperature. This is the expected behavior when the temperature dependence is not accurately corrected. In particular, these variations were larger at LED 3 with the emission peak at 430 nm, where both the rate of change in light intensity and the standard deviation were significantly higher (Fig. 2.5-c,f).

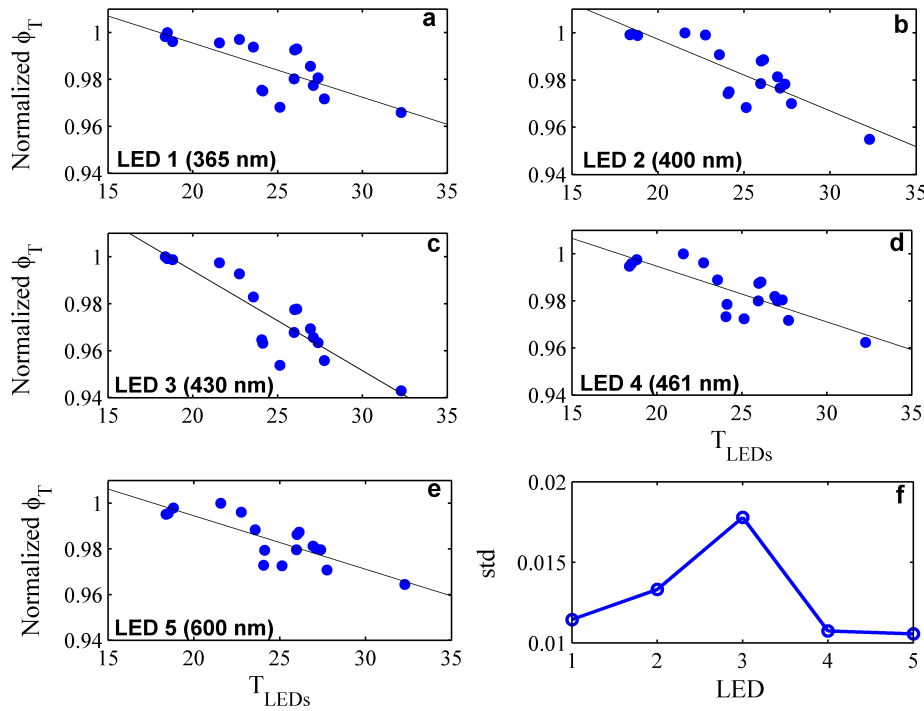


Figure 2.5: (a-e) Normalized transmitted light intensity as function of the operating temperature at the emission peak wavelengths of the five LEDs (*i.e.* 365 nm, 400 nm, 430 nm, 461 nm and 600 nm, respectively). The linear regression slope indicates the rate of change in the corrected output signal with the temperature of the diode. (f) Standard deviation of the measured data for the five LEDs.

To assess the effects of the observed fluctuations on the final beam attenuation coefficient, the measurements were processed using the same reference spectrum with a LED-temperature of $24^\circ C$ (Fig. 2.6). The results showed that not only the magnitude but also the spectral shape of the beam attenuation coefficient varied as a function of the LED-temperature. A change of $0.17 m^{-1}$ was obtained for a LED-temperature increment of $17^\circ C$ at 600 nm, which implied an error of $0.01 m^{-1}/^\circ C$. In addition, anomalous spectral features were observed from 420–440 nm (LED 3, Fig. 2.2), characterized by negative values of the beam attenuation when the LED-temperature of the sample was cooler than the reference and vice versa (blue and red lines in Fig. 2.6, respectively).

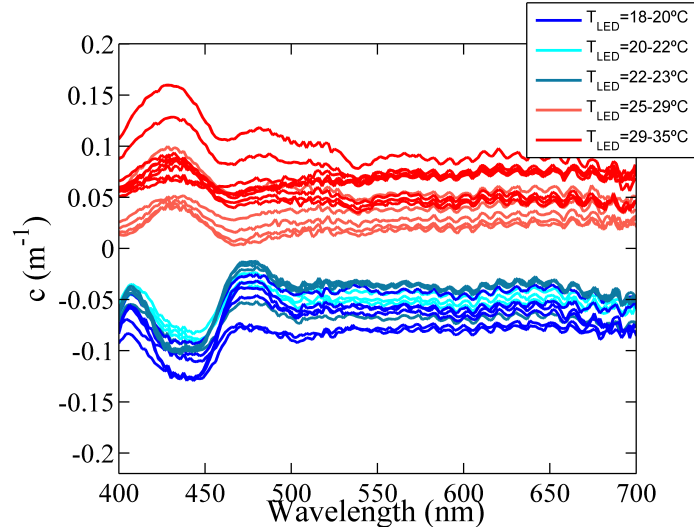


Figure 2.6: Corrected beam attenuation spectrum of purified water at different LED temperatures. The attenuation spectra were calculated relative to a reference spectrum with a LED-temperature of 24°C .

2.3.2 Instrument-Specific temperature and salinity correction factors

Laboratory experiments were carried out to determine the VIPER-specific temperature and salinity correction factors for the pure water attenuation coefficient. They are used in a correction procedure similar to that one employed by [Pegau *et al.* \(1997\)](#), and [Sullivan *et al.* \(2006\)](#), for the AC-9, AC-S and PSICAM instruments, respectively. The temperature and salinity dependence analysis was performed by using purified water (Milli-Q) at temperatures between 10°C and 35°C and a concentrated NaCl solution of 200 g/kg , respectively. The corresponding correction factors, ψ_T^i and ψ_S^i , represent the absolute change in water attenuation coefficient with the variation in temperature and salinity, *i.e.* $\delta c(\lambda)/\delta T$ and $\delta c(\lambda)/\delta S$ (units $[\text{m}^{-1}\text{ }^{\circ}\text{C}^{-1}]$ and $[\text{m}^{-1}\text{ PSU}^{-1}]$, respectively). In addition, the results were compared to model simulations of optical density in a cuvette based on [Max & Chapados \(2010\)](#). Additional details about the experiments, model simulations and the obtained temperature and salinity correction factors are provided in [Ramírez-Pérez *et al.* \(2015\)](#).

2.3.2.1 Temperature correction coefficients

VIPER-derived ψ_T^i spectral values and those predicted by model simulations are given in Fig 2.7-a. The spectral features for $\lambda > 500\text{ nm}$ agree very well with previous studies ([Pegau *et al.* 1997](#), [Röttgers *et al.* 2014b](#), [Sullivan *et al.* 2006](#)) and with the model (*i.e.* two smaller peaks at 604 and 662 nm and a large one at 740 nm), mainly showing the influence of temperature on the pure water light absorption. Spectral features induced by temperature changes at shorter wavelengths ($\lambda < 500\text{ nm}$) are very small, and changes in

the scattering coefficient here should not display any spectral signature, except a typical exponential increase with decreasing wavelength (Röttgers *et al.* 2014b). Hence, the spectral fluctuations observed in VIPER results at < 500 nm were considered to be induced by the above mentioned poor temperature compensation at the LED 3 (see Section 2.3.1.2). The small offset between VIPER measurements and model predictions was in the range of the experimental errors. When ignoring the spectral features at shorter wavelengths, the experimentally obtained ψ_T^i can be well represented by the model results of the specific optical setup. Thus, ψ_T^i values predicted by the model are considered here as final temperature correction factors (Fig. 2.7-b).

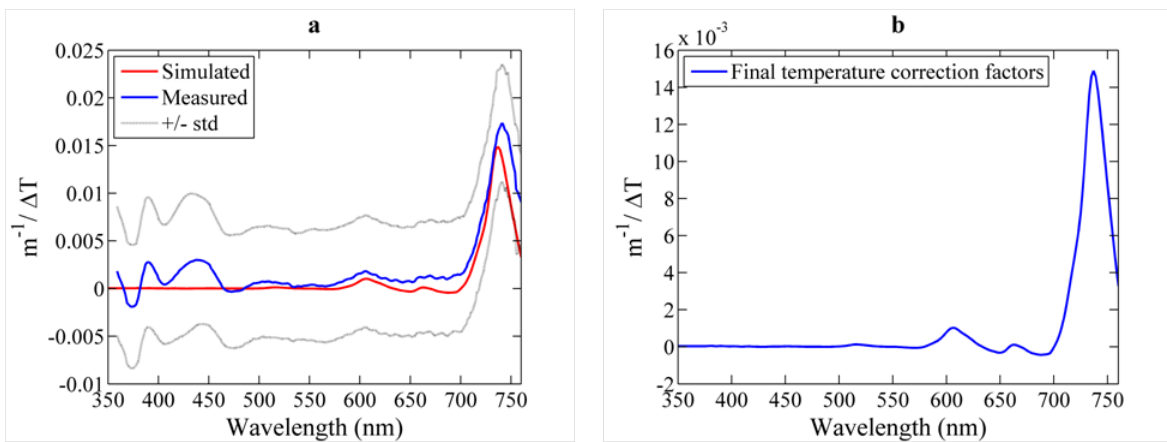


Figure 2.7: (a) Results from the temperature dependence analysis and the comparison with model simulations based on the approach by Max & Chapados (2010) (red line). The blue line corresponds to the average over the 20 experimental runs and the standard deviation is represented with dotted line. (b) Final VIPER-specific temperature correction coefficient for pure water beam attenuation as a function of the wavelength.

2.3.2.2 Salinity correction coefficients

The effects of the concentration of ions on the water attenuation and the optical path transmission were obtained both experimentally and computationally by using NaCl to represent seawater (Fig. 2.8-a). The ψ_S^i spectral values derived from both methods concurred for the spectral region $\lambda > 550$ nm and show overall agreement with previous works (Röttgers *et al.* 2014b, Sullivan *et al.* 2006). The main spectral features were the small negative troughs at 598 and 660 nm and the deeper negative trough at 733 nm followed by the positive peak at 757 nm. However, the noticeable trough at 540 nm displayed by VIPER results was not observed by model simulations or other studies. This behavior might be caused by stray light artifacts, whose analysis is outside the scope of the present work. Nevertheless, this effect is considered as an instrument-specific spectral feature since it was observed in all the experimental runs. The results for 360 – 500 nm showed an anomalous behavior that varied along the different tests. Similar to the results of the temperature analysis, it was

assumed that this behavior is related to the poor temperature compensation of the LED 3. Thus, these spectral features were discarded in the final ψ_S^i spectrum, and instead the model results were used here. Wavelength-independent differences between measured and modeled ψ_S^i were again smaller than the experimental error. For wavelengths > 500 nm the obtained ψ_S^i spectrum was finally adjusted to the level of the model results as depicted in Figure 2.8-b. Small differences on the magnitude of the troughs are due to the difference in optical resolution, which is 15 nm for VIPER and 1 nm for the model.

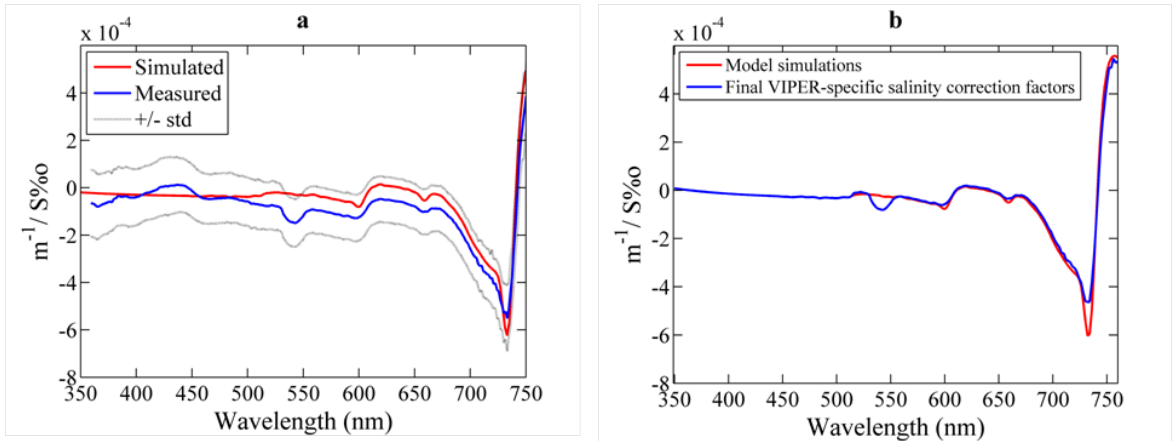


Figure 2.8: (a) Results from the salinity dependence analysis and comparison with model simulations based on the [Max & Chapados \(2010\)](#) approach (red line). The blue line corresponds to the average over 20 experimental runs and its standard deviation is represented by dotted lines. (b) Final VIPER-specific ψ_S^i spectrum for pure water beam attenuation as a function of the wavelength (blue line) and comparison with model simulations (red line).

2.3.3 Ambient light effects

The instrument’s sensitivity to ambient light fluctuations was analyzed in the field under different deployment conditions and different distances from the water surface. The study was performed on two different areas: Lake Schaalsee in northern Germany and Alfacs Bay in the NW Mediterranean coast (Spain). Sampling in Schaalsee was characterized by calm wave conditions and performed with the instrument hanging from a floating buoy. On the contrary, measurements in Alfacs Bay were conducted under rough sea surface conditions and the instrument was deployed from a winch mounted on a small boat. The beam attenuation spectra measured under both deployment conditions showed spectral contamination due to high-frequency variations in the ambient light (see Figs. 2.9 and 2.10). In both cases, the intensity collected by the instrument along the water column was slightly modified by waves focusing effects of sunlight occurring at periods of time shorter than the time interval between “dark” and light measurements. The induced artifacts were observed at specific wavelengths (500 – 550 nm and ~ 700 nm), at which the light intensity emitted by the LED system has minima (Fig. 2.2). This causes that variations in ambient light conditions have a

relatively large significant effect. The observed contamination also depends on the ambient light intensity, and consequently, on the sampling depth and turbidity level. Figure 2.10 shows the beam attenuation and the corresponding environmental light conditions (spectra measured with the light off) collected at different depths in a fixed station in Alfacs Bay. The variations in ambient light had a significant influence close to the surface, but decreased with water depth, being negligible at 3.7 m below the water surface.

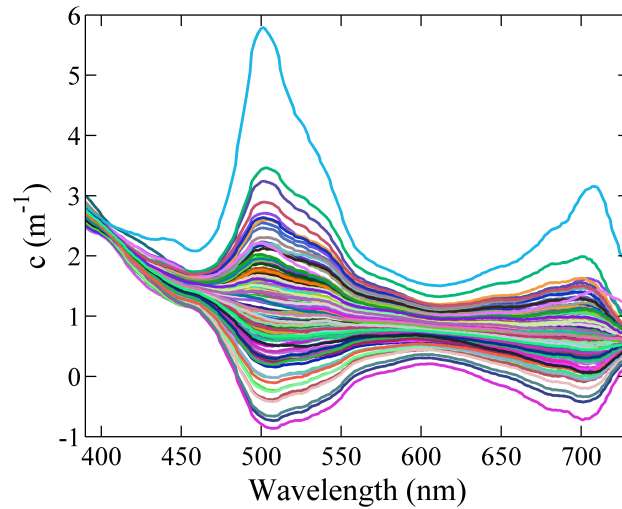


Figure 2.9: Example of artifacts in the measurements at specific spectral regions due to ambient light contamination during floating buoy deployment in Schaalsee Lake (Germany) in September 2014.

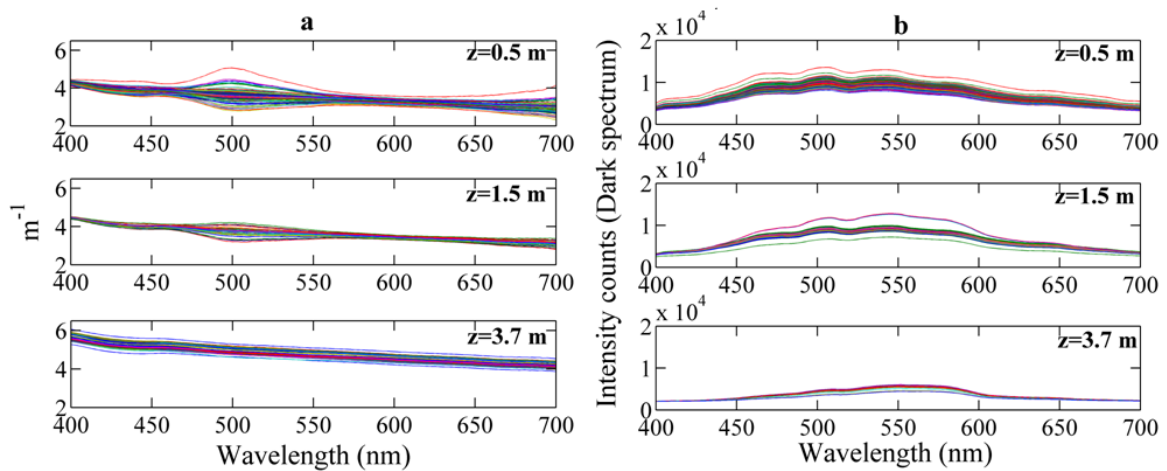


Figure 2.10: (a) Beam attenuation and (b) dark spectrum measured for several minutes at different depths in Alfacs Bay (NW Mediterranean coast, Spain) in March 2014.

2.3.4 Instrument performance during in situ measurements

The suitability of the VIPER transmissometer for coastal oceanographic applications was evaluated by comparison with other in situ transmissometers widely used and validated by the scientific community (AC-S, from WET Labs and LISST 100-X, from Sequoia Scientific). AC-S is a double cuvette spectrophotometer to measure the absorption and attenuation coefficients. It is a hyperspectral sensor (400 to 750 nm) with a spectral resolution of 5 nm, a band pass of 14 – 18 nm and the attenuation channel has a receptor acceptance angle of 0.93° . It employs flow tubes, tungsten lamps as light source and broadband detectors. Light of different wavelengths is analyzed by passing the collimated beam through a rotating, linear variable interference filter onto the detector (WetLabs 2014). The LISST 100-X is designed to measure volume scattering in near-forward direction at 32 different angles to determine the particle size distribution. It also measures the beam transmission at 670 nm along a 5-cm path length using a highly collimated, monochromatic and polarized light source, and the detector's acceptance angle is 0.0269° (Boss *et al.* 2009a). The comparison was performed with the beam attenuation coefficients measured by (i) 25-cm path length VIPER, (ii) 25-cm path length AC-S and (iii) 5-cm path length LISST 100-X. For this analysis, data collected during two field campaigns at a fixed station in the shallow estuarine area of Alfacs Bay (NW Mediterranean coast, Spain) were used. The dataset consisted of 24 hours time series of vertical profiles from 0.5 m to 3.5 m (maximum depth) with 0.5 m depth intervals. At each depth level, optical sensors were sampling continuously for five minutes.

2.3.4.1 VIPER vs AC-S

For the comparison of VIPER and AC-S, simultaneous measurements were collected from 6pm on March 24th to 6pm on March 25th 2014 in Alfacs Bay. For both instruments, recorded data were corrected for temperature and salinity effects and were averaged over five minutes. Due to the possibility that the presence of air bubbles in the path deteriorates the signal, only spectra with a relative error lower than 0.1 at 400 nm were selected for the analysis, which corresponded to about 60% of the total number of measurements. In general, good overall agreement was found between both instruments, although at 600 nm the attenuation coefficient was, on average, 4% higher for AC-S than for VIPER (Fig. 2.11-a). To evaluate the statistical significance of the difference in the beam attenuation of both instruments, a Student's two-tailed t-test was applied. Based on these results, no significant differences were found over the complete wavelength range investigated ($p = 0.77$ on average). Nevertheless, the root mean square error (RMSE) between both instruments was calculated as a function of the wavelength (Fig. 2.11-b). The maximum RMSE, 0.36 m^{-1} , was obtained at 430 nm strongly suggesting that artifacts associated with the thermal management of LED-430 nm

are responsible for this behavior.

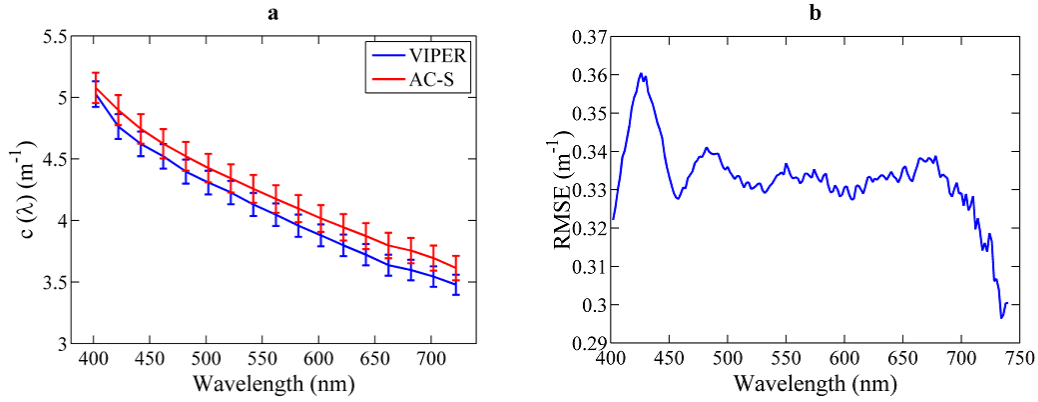


Figure 2.11: (a) Mean average and standard error of the spectral beam attenuation measured by VIPER (blue) and by WET Labs AC-S (red) in Alfacs Bay, respectively. (b) Root mean square error between VIPER and AC-S at different wavelengths for the analyzed data.

For a more detailed assessment of the different spectral shapes derived from both instruments, the spectral slopes were compared. For this analysis, beam attenuation spectra were fitted to a power law function $c(\lambda) = A \cdot \lambda^{-\gamma}$ between 400 and 700 nm. The goodness of fit, R^2 , was higher than 95% in all cases and the RMSE was of 0.036 and 0.034 for VIPER and AC-S, respectively. VIPER and AC-S spectral slopes exhibited a good correlation ($R^2 = 0.8$) and the same temporal trend along the time series, although VIPER slopes were slightly steeper than those from the AC-S (Fig. 2.12). The parameter γ varied between 0.43 and 0.75 for AC-S, whereas for VIPER it varied from 0.48 to 0.79, *i.e.*, values about 10% higher in the latter case. However, the result from the t-test showed that these differences are not statistically significant, with a p-value equal to 0.12.

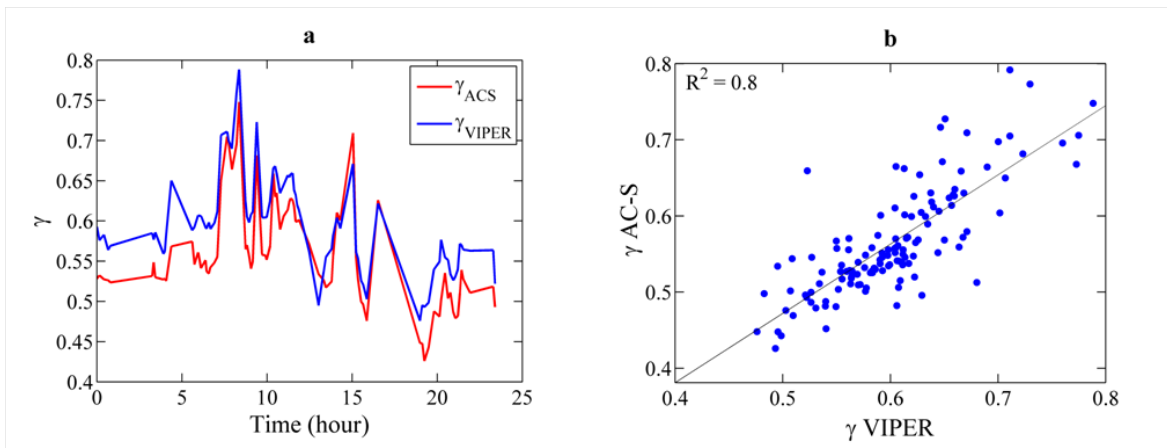


Figure 2.12: (a) Comparison of beam attenuation slopes, γ , measured with VIPER (blue) and AC-S (red) during vertical profiling at a fixed station in Alfacs Bay in March 2014. (b) Linear correlation between the slopes derived from both instruments for the analyzed time series.

2.3.4.2 VIPER vs LISST 100X

A second dataset of experimental measurements was obtained to compare the performance of VIPER with LISST-100X. In this case, simultaneous measurements were collected from 9pm on June 24th to 7pm on June 25th 2013 in Alfacs Bay, and were averaged over five minutes. The beam attenuation at 670 nm exhibited the same temporal trend for both instruments, although its magnitude differed significantly due to the strong difference in the acceptance angle (0.8° vs 0.0269°) (Boss *et al.* 2009b) (Fig. 2.13-a). The ratio of VIPER to LISST beam attenuation was on average 0.67, *i.e.*, VIPER underestimated the beam attenuation by 33% compared to LISST, due to the higher collection of near forward scattered light by VIPER (Fig. 2.13-b). This ratio varied between 0.57 and 0.72 along the time series, as a consequence of variations in the particle size distribution, that changes the volume scattering function (Boss *et al.* 2009b). Despite the known effect of the acceptance angle in the absolute beam attenuation coefficient, temporal variations are represented in the VIPER signal as good as in the LISST one.

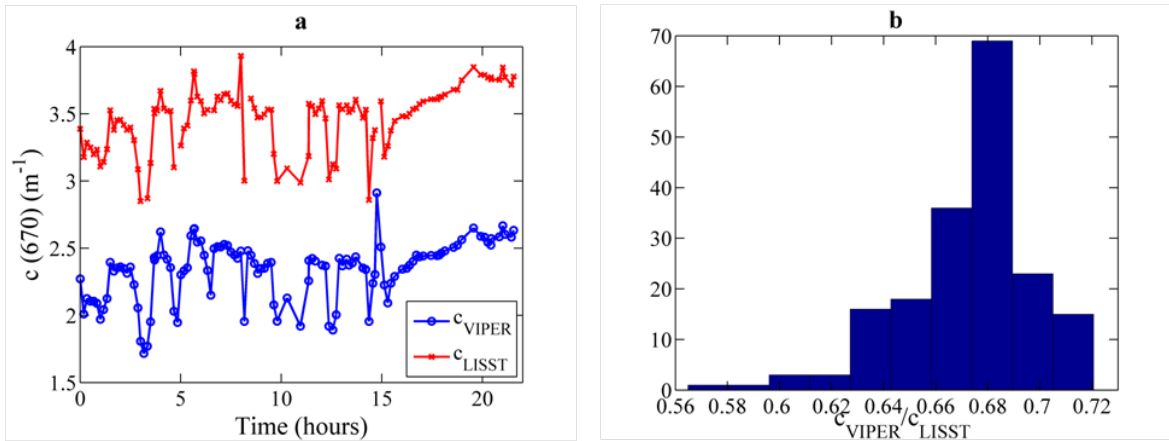


Figure 2.13: (a) Comparison of beam attenuation at 670 nm measured by VIPER (blue) and by LISST-100X (red) during vertical profiling at a fixed station in Alfacs Bay in June 2013. (b) Histogram with the frequency of occurrence of the ratio c_{VIPER}/c_{LISST} .

2.4 Discussion

The performance analysis of the newly-developed VIPER transmissometer allowed to define the instrument limitations as well as to determine the suitability of this instrument for specific coastal applications. Firstly, our results suggested that the application range of the VIPER 25-cm path length should be narrower than that one proposed by the manufacturer (*i.e.*, from $0.04 m^{-1}$ to $9.2 m^{-1}$). Regarding the lower bound, fluctuations of the light intensity were of the order of $0.04 m^{-1}$ at the shortest wavelengths, which implies an error of about 100% at these attenuation levels. These results were obtained after the warm-up

period, which was found here to be around 10 min. Furthermore, according to [Bugnolo \(1960\)](#), about 67% of the light will be multiply scattered along a path length of 25 cm at $c = 9.2 \text{ m}^{-1}$. Therefore, the suitable upper bound should be lower. Secondly, contrary to the proposal by [Voss & Austin \(1993\)](#), the acceptance angle of the VIPER's detector is smaller than the divergence of the beam source. This implies that part of the light exiting the source is not collected by the receiver. However, this light could be partially scattered by the suspended particles and redirected onto the detector. Thus, the real attenuation is underestimated. This explains the differences on the magnitude obtained between VIPER and both, the AC-S and LISST-100X instruments. In the first case, the AC-S beam attenuation coefficient was on average 4% higher than that obtained with VIPER. In the second case, the average VIPER to LISST ratio amounted to 0.67, which was in good agreement to the C-Star to LISST-100X ratio, $C_{C-STAR}/C_{LISST} = 0.7$, found by [Boss *et al.* \(2009a\)](#) (the C-Star acceptance angle is 1.2°). Despite these differences on the magnitude of the beam attenuation coefficient, we have demonstrated that VIPER provides reliable measurements in coastal waters based on our comparison to results obtained with the other transmissometers. Our validation was performed under field conditions with an attenuation range between 1.6 m^{-1} and 6 m^{-1} . Although no statistically significant differences were found at any of the analyzed wavelengths, the maximum error between VIPER and AC-S was obtained for the spectral range 420-440 nm. An anomalous behavior at this spectral region was also observed in the laboratory tests performed to determine the instrument-specific temperature and salinity correction factors. We observed that the LED-temperature compensation was poorly corrected at these wavelengths. The LED emitting light in this range has an emission peak at 430 nm (LED 3, see [Fig. 2.2](#)). In particular, this is a SMD (Surface Mounted Design) LED with ball lens, located at the center of the LEDs array (pers. comm. TriOS GmbH). The anomalous results in this spectral range suggest that this LED is overheated due to its mounting configuration. Depending on their design and position, the LEDs are heated up in a different rate, which is difficult to be accurately measured with a single internal temperature sensor. It is important to mention that these results were obtained in the lab by sampling in a continuous mode. Therefore the use of a longer timer mode might improve the LED-temperature compensation. In this way, the LED bulbs would heat up at a lower rate having a longer time for temperature stabilization. In addition, some limiting issues related to ambient light contamination were detected at specific deployment conditions. They are a consequence of the open-path design of VIPER and the non-flat white light spectrum emitted by the LEDs. Thus, specific spectral regions present higher sensitivity to slight variations in the environmental conditions, which induce significant spectral artifacts. However, the constant evolution in LEDs technology led to the development of flat-white LEDs (*e.g.* [Electrospell 2015](#)). Therefore, the observed limitations could be signifi-

cantly avoided in future instrument generations. The LED-temperature compensation could be also improved by the integration of several internal temperature sensors to make possible an accurate measurement of the temperature of each LED. In case that these corrections would not be sufficient, an active temperature regulation system could be implemented to set the LED at a reference temperature. Regarding the ambient light contamination, these effects could be somewhat reduced by shielding the instrument from the ambient light. By considering the recommendations and application limits analyzed in this study, we conclude that the VIPER transmissometer is a potentially interesting tool for specific coastal applications due to the numerous advantages of his design. Furthermore, the distinct features of this instrument allow it to be mounted on several oceanic observing platforms (*e.g.*, gliders, AUVs, mooring systems) for large-scale characterization of oceanic processes.

2.5 Conclusions

A performance analysis was carried out in order to examine the reliability of the beam attenuation coefficient derived from a newly-developed cost-effective hyperspectral transmissometer (*i.e.* the VIS-Photometer VIPER, TriOS GmbH). A distinct feature of this instrument is to employ an array of different LEDs as light source to provide a full visible-light spectrum. In addition, it uses a micro-spectrometer as detector, which makes it compact. The comparison with other commercial transmissometers demonstrated that VIPER provides reliable beam attenuation measurements in coastal waters applications. In addition to these overall satisfactory results, some spectral artifacts were detected at wavelengths in the range 420-440 nm. The origin of this behavior was related to a poor temperature compensation of one of the integrated LEDs ($\lambda_p = 430$ nm). Ambient light contamination was also observed as a consequence of the non-uniformity in the emitted light intensity, which causes that some spectral regions are more sensitive to the environmental light. These results suggested that future instrument developments should focus on the optimization of these issues. Additionally, a second generation of this instrument should benefit from including a detector acceptance angle equal or higher than the divergence of the beam source. However, with a prior knowledge of the described limiting factors and recommendations of use, the VIPER instrument, as a cost-effective and compact hyperspectral transmissometer, can be considered as a powerful alternative to traditional transmissometers for specific coastal waters applications.

Chapter 2

3

Application of cost-effective spectral beam attenuation measurements to assess changes and patterns in biogeochemical variables in a coastal environment

In the previous chapter, the performance and limitations of an economically affordable and advanced-technology transmissometer have been examined. At this point, we are therefore prepared to use it in the field and thus, to investigate its suitability as optical tool for high resolution characterization of coastal waters. Thereby, this chapter evaluates the potential of this kind of transmissometers for assessing temporal and spatial patterns in the complex estuarine waters of Alfacs Bay (NW Mediterranean) as a test site. In particular, the information contained in the spectral beam attenuation coefficient is assessed and linked with different biogeochemical variables. The attenuation at $\lambda = 710$ nm has been used as a proxy for particle concentration, TSM, whereas a novel parameter has been adopted as an optical indicator for chlorophyll a (Chl-a) concentration, based on the local maximum of $c(\lambda)$ observed at the long-wavelength side of the red band Chl-a absorption peak. In addition, since coloured dissolved organic matter (CDOM) has an important influence on the beam attenuation spectral shape and complementary measurements of particle size distribution are available, the beam attenuation spectral slope has been used to analyze the CDOM content. Results have been successfully compared with optical and biogeochemical variables from laboratory analysis of collocated water samples, and statistically significant correlations have been found between the attenuation proxies and the biogeochemical variables TSM, Chl-a and CDOM. This outcome depicts the potential of high-frequency beam attenuation measurements as a simple, continuous and cost-effective approach for rapid detection of changes and patterns in biogeochemical properties in complex coastal environments.

This chapter corresponds to the published article: *Ramírez-Pérez M, Gonçalves-Araujo R, Wiegmann S, et al. (2017) Towards Cost-Effective Operational Monitoring Systems for Complex Waters: Analyzing Small-Scale Coastal Processes with Optical Transmissometry. PLoS ONE 12(1): e0170706*

3.1 Introduction

Coastal environments are governed by complex physical and biogeochemical processes and thus, undergo changes over a broad range of time-space scales. Continuous and routine provision of data is therefore required to assess the states of coastal ecosystems, detect changes in these states and evaluate their impacts (IOC-UNESCO 2012). The advancement of sensor technology, data acquisition and storage capabilities occurred in the last three decades, make possible to achieve these sampling requirements. An example of this advanced-technology sensor has been introduced in the previous chapter, which showed the distinct characteristics of the recent commercially available transmissometer VIPER (TriOS, GmbH.), as a kind of LED-based hyperspectral and cost-effective beam attenuation meter. The next step consists of evaluating to what extent these measurements allow to assess the state of coastal ecosystems and detect patterns and changes in these states, by providing valuable information about water composition.

Studies based on beam attenuation measurements have been restricted to the use of the particulate beam attenuation coefficient, c_p , at one specific wavelength (commonly at 532, 555, 660 or 670 nm) or the c_p spectral slope, in order to assess the particle concentration (Boss *et al.* 2009b) or the particle size distribution (Boss *et al.* 2001a), respectively. The attenuation coefficient at those wavelengths have been also related to the particulate organic carbon (Loisel & Morel 1998, Oubelkheir *et al.* 2005) or to the chlorophyll concentration (Behrenfeld & Boss 2006, Green *et al.* 2003), but only in oceanic waters. In coastal waters, c_p also registers changes in inorganic, detrital, and heterotrophic particles, thus compromising its correlation with chlorophyll a (Chl-a) concentration (Behrenfeld & Boss 2006). Nevertheless, the correlation between both variables (*i.e.* c_p and Chl-a) still needs to be further explored. The recent development of high spectral resolution (hyperspectral) transmissometers broadens the possibility to extract additional information from the spectral beam attenuation signal, as it has been demonstrated for various optical properties, such as remote-sensing reflectance (Louchard *et al.* 2002, Lubac *et al.* 2008), particulate absorption (Organelli *et al.* 2013, Torrecilla *et al.* 2011) and underwater radiance spectra (Taylor *et al.* 2013).

Thus, this chapter seeks to go one step further on the analysis of beam attenuation spectra, by exploiting all its spectral information to assess the scales of variability in the major in-water constituents.

The study is focused on the microtidal estuary of Alfacs Bay (Ebro Delta, NW Mediterranean coast), using it as a test site. This bay is an important shellfish production area commonly affected by HABs events, which lead to significant economic losses (Berdalet *et al.* 2010). For this reason, this area has been intensively monitored since 1990. Research efforts have focused

on characterizing the hydrodynamics of this bay (Camp & Delgado 1987, Cerralbo *et al.* 2014, Solé *et al.* 2009), its ecology (Garcés *et al.* 1997) and the coupling between physical and biological processes (Llebot 2010). However, the use of optical-based approaches in this area -which allow the assessment of fine-scaled temporal and spatial variability of water constituent characteristics- is still very limited. Only Busch (2013) analyzed the phytoplankton dynamics in this environment using radiometric measurements, which provided useful data only in day time. One of the main conclusions of this author was that continuous observations in Alfacs Bay are required to properly understand the rapid ecosystem dynamics.

3.2 Material and Methods

3.2.1 Study site

Alfacs Bay is located in the south of the Ebro River Delta (Spain), in the NW Mediterranean Sea (Fig. 3.1). It is a shallow estuarine bay with 11 km length, 4 km width and a maximum depth of 6.5 m. It is a semi-enclosed embayment separated from the open sea by a sand barrier that leaves an opening of roughly 2.5 km width, allowing the exchange of water with the open sea. The major physical forcings in the bay are wind and freshwater input, whereas tidal forcing is negligible with a maximum range of 0.25 m (Llebot *et al.* 2013). The freshwater discharge is derived mainly from the rice-fields irrigation channels, located in the northern part of the Bay. These channels are open from April to October or November, with an average flux rate of ca. $14.5 \text{ m}^3 \cdot \text{s}^{-1}$ (Camp, 1994). The freshwater inputs induce vertical stratification, while only during strong wind events the water column is vertically mixed (Camp & Delgado 1987). Heat fluxes in the ocean-atmosphere boundary layer in summer periods contribute in addition to stratifying the water column (Cerralbo *et al.* 2015).

3.2.2 Field campaign

Two sampling strategies were adopted to analyze both temporal and spatial patterns in Alfacs Bay in June 2013. The analysis of temporal patterns was conducted from the 24th of June at 9:30 pm for 48 hours. This time series of vertical profiles was gathered from 0.5 m to 3 m depth at a fixed station located in the north-central part of the Bay (blue circle in Fig. 3.1). At this station, simultaneous measurements of physical (wind and current velocities and direction, and water temperature) and optical parameters (beam attenuation and near-forward angular scattering) were conducted continuously with a vertical resolution of 0.5 m. At each depth, instruments measured for 10 minutes. Thereby, each vertical profile took approximately 1 hour. Water samples were collected every 6 hours at three different depths (0.5 m, 1.5 m and 3 m) for later laboratory analysis of biogeochemical and optical

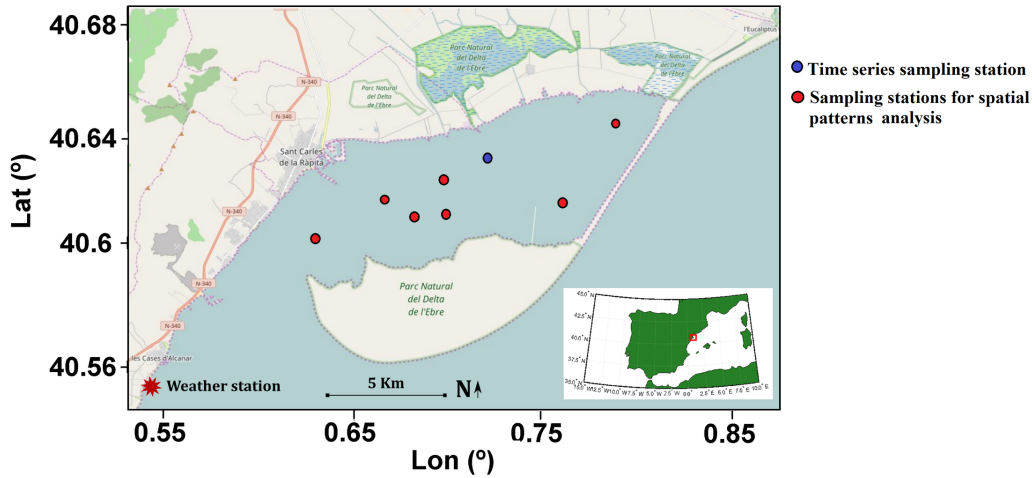


Figure 3.1: Location map of Alfacs Bay in NW Mediterranean Sea. The red star indicates the location of the weather station, whereas circles show the sampling stations for the analysis of temporal (blue circle) and spatial (red circles) patterns. Map produced with Open Street Map.

parameters [Chl-a, total suspended matter (TSM), algal and non-algal particulate absorption (a_{ph} and a_{nap} , respectively) and coloured dissolved organic matter (CDOM) absorption]. The analysis of the spatial variability was undertaken on the 27th of June at seven stations along the bay (red circles in Fig. 3.1). At each station, measurements of physical (temperature and salinity) and optical parameters were made with a ship deployed profiling package and water samples were collected at three different depths (0.5 m, 3 m and 0.5 m above the bottom). Instruments measured for 5 minutes every 0.5 m along each depth profile.

3.2.2.1 Physical parameters

Wind data were obtained from the weather station nearby the coastline in Les Cases de Alcanar, ca. 5 km south of Alfacs Bay (Fig 3.1). Three-dimensional current velocities were measured with an upward-looking Acoustic Doppler Current Profiler (ADCP, 2MHz Aquadopp, Nortek) moored at roughly 2 m depth since the maximum depth at this station was 3.5 m. It was configured to record 10-min average data with vertical cells of about 25 cm. Water temperature and salinity were measured with the CTD48M (Sea&Sun Technology, Germany). Unfortunately, a failure in the instrument caused the loss of the data corresponding to the temporal analysis at the fixed sampling station. Temperature data provided by the multiple-parameter system LISST (Sequoia Scientific Inc.) were used instead.

3.2.2.2 Optical measurements

Spectral beam attenuation coefficient was measured with the 25-cm path length VIPER (TriOS GmbH., Germany). It is an open-path hyperspectral transmissometer which measures

the beam attenuation, $c(\lambda)$, in the spectral range from 360 nm to 750 nm, with an optical resolution of 15 nm (defined by the FWHM) and an acceptance angle of 0.8° . VIPER measurements were carefully performed (*i.e.* on the shadow side of the ship and under calm sea surface conditions) to avoid ambient light contamination. $c(\lambda)$ data were collected continuously and averaged over 5 minutes. Milli-Q water references were subtracted and data were corrected for temperature and salinity dependence of pure seawater to derive the total non-water beam attenuation spectrum, $c_{pg}(\lambda)$ (Ramírez-Pérez *et al.* 2015). Measurements of particle size distribution (PSD) from $1.25 \mu\text{m}$ to $250 \mu\text{m}$ were conducted with the LISST-100X (Sequoia Scientific, Inc.). This instrument measures the near-forward scattering at 32 logarithmically spaced angles and the beam attenuation at 670 nm (Agrawal & Pottsmith 2000). This study focused only on the LISST scattering data to derive the particle size distribution. The volume concentration, $V(D)$, was obtained through inversion of the angular forward scattering pattern using the manufacturer-provided inversion routine. The used inversion algorithm is based on a kernel matrix derived from Mie theory of scattering by spherical particles. Data from the outer and inner rings were excluded from further analysis due to the instability observed in the smallest and largest size ranges (Jouon *et al.* 2008). Then, the particle number distribution, $N(D)$, was calculated from the equation:

$$N(D) = 6 \cdot V(D) / \Pi \cdot D^3 \quad (3.1)$$

where D represents the diameter of a volume-equivalent sphere for the midpoint of each size class. To obtain the PSD, the average number of particles in each size class was divided by the width of the class, which is denoted as $N'(D)$. Finally, the PSD was fitted to the power-law function (or Junge distribution) (Jonasz 1983):

$$N'(D) = N'(D_0) \left(\frac{D}{D_0} \right)^{-\xi} \quad (3.2)$$

where D_0 is a reference diameter, $N'(D_0)$ the differential number concentration at D_0 and ξ is the nondimensional PSD slope.

3.2.2.3 Laboratory analysis of water samples

- CDOM absorption measurements: absorbance spectra (240–600 nm) were acquired with the Aqualog fluorescence spectrometer (HORIBA JobinYvon, Germany) directly after sampling. Water samples were syringe-filtered with $0.2 \mu\text{m}$ Whatman Spartan filters before analysis with 1 cm quartz cuvettes. Absorbance measurements were further converted to absorption coefficient, which is used as a proxy for the CDOM content in a given water sample. The Napierian absorption coefficient of CDOM at each wavelength

(a_λ) was obtained from the given equation:

$$a_\lambda = (2.303 \cdot A_\lambda)/L[m^{-1}] \quad (3.3)$$

where A_λ is the absorbance at specific wavelength and L is the cuvette path length in meters. More detailed information about the measurement protocol can be found in [Gonçalves-Araujo *et al.* \(2015\)](#). CDOM absorption spectra, $a(\lambda)$, were fitted to the following exponential function ([Jerlov 1976](#)):

$$a(\lambda) = a(\lambda_0) \cdot e^{-S(\lambda-\lambda_0)} \quad (3.4)$$

where S represents the spectral slope and $a(\lambda_0)$, the absorption coefficient at a reference wavelength λ_0 (443 nm in this case). The function was fitted to the wavelength range from 300 to 600 nm and extrapolated to 720 nm for later analysis of CDOM contribution at longer wavelengths.

- Algal and non-algal particulate absorption ($a_{ph}(\lambda)$ and $a_{nap}(\lambda)$): water samples were immediately filtered through ϕ 47-mm GF/F filters (pore size 0.7 μm), shock-frozen in liquid nitrogen and stored at $-80^\circ C$ until analysis in the laboratory at the Alfred-Wegener-Institute. The partition of the particulate absorption, $a_p(\lambda)$, into phytoplankton, $a_{ph}(\lambda)$, and non-algal absorption, $a_{nap}(\lambda)$, was performed by the filter pad technique following [Ferrari & Tassan \(1999\)](#). We used a Cary 4000 UV/VIS dual beam spectrophotometer equipped with a 150-mm integrating sphere (Varian Inc., USA) as described in [Talyor *et al.* \(2011\)](#). The measurement procedures and data analysis were performed as detailed in [Röttgers & Gehnke \(2012\)](#). Phytoplankton absorption a_{ph} was obtained as the difference between a_p and a_{nap} .
- Chlorophyll a: water samples for phytoplankton pigments analysis were filtered immediately after collection through ϕ 25-mm Whatman GF/F filters (pore size 0.7 μm). Then, filters were shock-frozen in liquid nitrogen and stored at $-80^\circ C$ until analysis in the laboratory at the Alfred-Wegener-Institute. The extracted pigments were analyzed using the High Performance Liquid Chromatography (HPLC) technique following the method of [Barlow *et al.* \(1997\)](#), with modification customized to our instruments as detailed in [Talyor *et al.* \(2011\)](#). In this study, we use the Chl-a concentration as an index of phytoplankton biomass and covarying materials (biogenic detritus).
- Total suspended matter concentration: TSM concentration was determined gravimetrically following [Röttgers *et al.* \(2014a\)](#) to reject potential errors associated with salt retention in the filters and loss of materials during washing and combustion ([Röttgers *et al.* 2014a,](#)

Stavn *et al.* 2009). Thereby, four different volumes of each water sample (within the range from 0.6 to 2.2 liters) were filtered immediately after collection through pre-weighed Whatman GF/F filters (ϕ 47 mm). Afterwards, the gained mass of each filter was determined by subtracting the weight of the filter from the final weight. A linear regression analysis was performed for filtered volume versus the gained mass, and the regression slope was taken as the TSM concentration value (Röttgers *et al.* 2014a).

3.2.2.4 Data and statistical analysis

This study explored the information contained in the beam attenuation spectrum as a proxy for different biogeochemical properties. In particular, the analysis focused on three major spectral features, which are described as follow (Fig. 3.2):

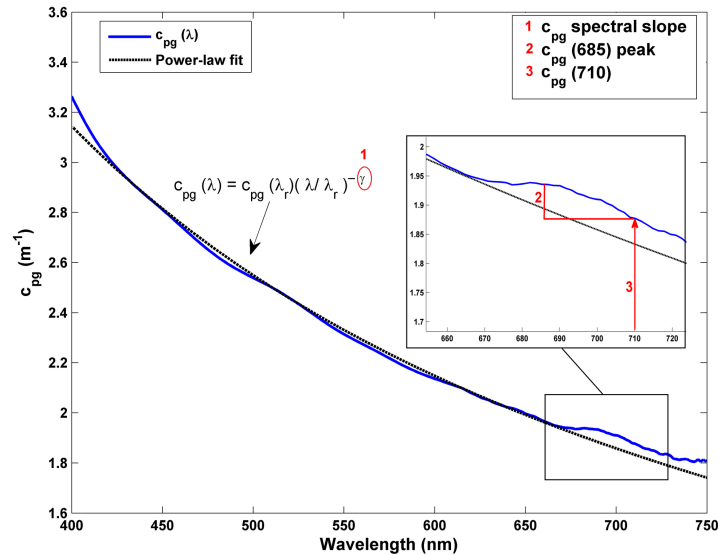


Figure 3.2: Representative total non-water beam attenuation spectrum measured in Alfacs Bay in June 2013. Numbers 1-3 indicate the three spectral features used in this study as proxies for biogeochemical variables: 1 = spectral slope of $c_{pg}(\lambda)$ for CDOM absorption, 2 = $c_{pg}(685) - c_{pg}(710)$ for Chl-a and 3 = $c_{pg}(710)$ for TSM concentration.

- Spectral slope: it is the major spectral shape feature of the beam attenuation coefficient and is related to the particle size distribution and CDOM content (Boss *et al.* 2001a). For this reason and due to the lack of in situ CDOM absorption measurements, we used the total non-water beam attenuation spectral slope to detect variations in CDOM. This simplification was adopted because of the high CDOM content in Alfacs Bay (Busch 2013) and the availability of additional particle size distribution measurements. To compute this parameter, beam attenuation spectra were fitted to the power-law function (Boss *et al.* 2001a):

$$c_{pg}(\lambda) = c_{pg}(\lambda_r) \cdot (\lambda/\lambda_r)^{-\gamma} \quad (3.5)$$

where λ_r is a reference wavelength (532 nm, in our case) and γ is the power-law slope. The exponent was derived by non-linear least-squares regression, with a $r^2 > 0.98$ in all cases.

- Peak height associated with red band phytoplankton absorption peak: although $c(\lambda)$ is typically a smoothly varying function of wavelength (Boss *et al.* 2001b, Voss 1992), deviations from its theoretical behavior -associated with absorbing particles- have been reported by several authors (Bricaud & Morel 1986, Zaneveld & Kitchen 1995). Zaneveld & Kitchen (1995) observed step increases at the long-wavelength side of the chlorophyll absorption peaks as result of anomalous diffraction and dispersion (Van de Hulst 1957), which was called “absorption peak effects”. This local maximum is therefore expected to be related to the Chl-a content (in addition to other factors such as the particle size distribution) (Zaneveld & Kitchen 1995). For this reason, the link between the local maximum of $c(\lambda)$ and the Chl-a concentration was tested in this study, since it can provide a first estimate of phytoplankton biomass and covarying materials. Similarly to Davis *et al.* (1997), who estimated the Chl-a concentration based on the red band absorption peak - $a(676)$ - by subtracting a baseline, we computed the peak height in the red band of the beam attenuation spectrum. However, here the local maximum was found at 685 nm (approximately 10 nm past the absorption peak, in agreement with Zaneveld & Kitchen (1995)). The attenuation at 710 nm was then subtracted from this local peak as a base value to remove the effect of particle scattering. This wavelength was empirically chosen based on providing the best results (based on r^2 and RMSE as compared to collocated Chl-a data determined by HPLC at discrete samples). Thereby, the peak height was computed as $c_{pg}(685) - c_{pg}(710)$, which was used as a proxy for Chl-a concentration.
- $c_{pg}(710)$: At long visible wavelengths, the attenuation is assumed to be determined mostly by their scattering properties and secondarily by the particulate absorption, whereas CDOM absorption has a insignificant contribution (Hill *et al.* 2011, Neukermans *et al.* 2012). For this reason, the attenuation in the red part of the visible spectrum (*i.e.* 660 and 670 nm) has been commonly used as proxy for suspended particle concentration, since it responds primarily to concentration and secondarily to size and nature of the particles (Gernez *et al.* 2011). While this assumption can be considered true in open waters, it could fail for complex coastal waters with high CDOM contents, which can yield a non-negligible CDOM absorption at long wavelengths (~ 700 nm). Nevertheless, the exponential decrease of CDOM absorption with wavelength involves that the longer

the wavelength, the smaller its contribution to the beam attenuation signal. For this reason, this study used the beam attenuation in the NIR (concretely at 710 nm) as proxy for TSM, where the CDOM absorption influence was minimum.

Variations in time and space of these optical parameters were analyzed by means of statistical techniques. In particular, the Kruskal-Wallis H-test was applied at 5% significance level ($\alpha = 0.05$) in order to identify temporal and spatial patterns in Alfacs Bay, given that data were not normally distributed, as demonstrated by the Shapiro-Wilk test performed prior to analysis. On the other hand, since both inputs were subject to errors, a model II linear regression analysis was applied to investigate the relationships between optical parameters and biogeochemical variables. Additionally, the correlations between them were examined using non-parametric Spearman-r correlation coefficients and the associated errors were determined by means of the root mean squared error (RMSE).

3.3 Results and Discussion

At first, the results from validating the above-mentioned beam attenuation-based proxies with laboratory-measured biogeochemical variables are presented. Secondly, the temporal and spatial variability and patterns of these optical and biogeochemical parameters in Alfacs Bay are shown.

3.3.1 Validation of biogeochemical proxies

3.3.1.1 Attenuation at 710 nm *vs.* Total Suspended Matter concentration

The comparison between the total non-water beam attenuation coefficient and the particulate and CDOM absorption at 710 nm ($c_{pg}(710)$, $a_p(710)$ and $a_{CDOM}(710)$, respectively) was performed to determine the relative contribution of the two last components to the bulk $c_{pg}(710)$ signal (Fig. 3.3-a). In all samples, $a_p(710)$ and $a_{CDOM}(710)$ represented a minor fraction of $c_{pg}(710)$, since their values were two orders of magnitude lower than $c_{pg}(710)$. $c_{pg}(710)$ oscillated from 0.96 to 4.66 m^{-1} , whereas $a_p(710)$ and $a_{CDOM}(710)$ ranged from 0.0065 to 0.025 m^{-1} in our dataset. The insignificant CDOM contribution to the attenuation signal at 710 nm, enabled to use $c_{pg}(710)$ as proxy for TSM. Then, a model II linear regression analysis was applied to investigate the relationship between $c_{pg}(710)$ and TSM (Fig. 3.3-b). The regression slope (\pm SD) was $0.224 \pm 0.03 g \cdot m^{-2}$, which agreed with previous works (Boss *et al.* 2009b, Hill *et al.* 2011). In addition, although our slope was flatter, our observations were within the confidence bounds of the relationship found by Neukermans *et al.* (2012) for the C-Star attenuation meter (with an acceptance angle of 1.2°) (Fig. 3.3-b). This disparity in the regression slope can be partly explained due to the different attenuation

wavelength used in the relationship (670 and 710 nm in [Neukermans *et al.* \(2012\)](#) and in our study, respectively). A significant correlation was observed between $c_{pg}(710)$ and TSM, with $r^2 = 0.75$ and $RMSE = 0.49 m^{-1}$ ($p < 0.001$).

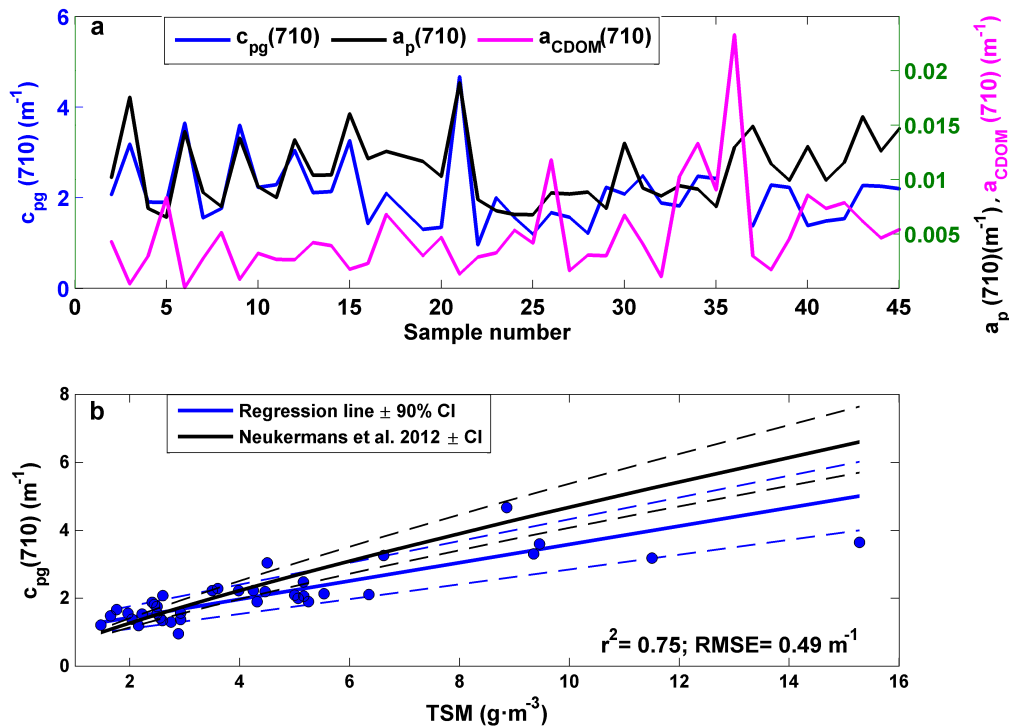


Figure 3.3: (a) Comparison of $c_{pg}(710)$, $a_p(710)$ and $a_{CDOM}(710)$ along all the samples used in this study. (b) Scatter plot of TSM and the attenuation at 710 nm. Best fit $\pm 90\%$ confidence intervals are shown in blue. Black solid and dashed lines represent the 90% prediction bounds of the $[TSM] - c_p(670)$ data of [Neukermans *et al.* \(2012\)](#) (for the C-Star).

3.3.1.2 $c_{pg}(685)$ peak height vs. Chl-a concentration

A relatively good linear correlation was found between the Chl-a concentration and the non-water attenuation peak height at 685 nm, $c_{pg}(685)$ peak ($r^2 = 0.79$, $RMSE = 0.014 m^{-1}$, $p < 0.001$, Fig. 3.4-a). Thereby, it is reasonable to consider $c_{pg}(685)$ peak as a proxy for tracking changes in Chl-a concentration. Since this peak was associated with the red-band Chl-a absorption peak due to anomalous dispersion, the linear correlation between $c_{pg}(685)$ peak and the laboratory-derived phytoplankton absorption at 676 nm, $a_{ph}(676)$, was examined (Fig 3.4-b). A significant linear correlation was also obtained in this case, with $r^2 = 0.68$ and $RMSE = 0.014 m^{-1}$ ($p < 0.01$). In turn, the correlation between Chl-a concentration and $a_{ph}(676)$ was analyzed ($r^2 = 0.83$; $RMSE = 0.019 m^{-1}$; $p < 0.001$) and compared to the power-law fit obtained by [Bricaud *et al.* \(1995\)](#). Our observations were in agreement with the function predicted by those authors (Fig 3.4-c). According to [Bricaud *et al.* \(1995\)](#), the relationship between $a_{ph}(\lambda)$, and Chl-a varied as a result of

changes in packaging effect and pigment composition. Our proxy is therefore suspected to be affected not only by these factors but also by minor contributions associated with CDOM and non-algal particles absorption, particle size distribution or Chl-a fluorescence, which compromise the relationship found between Chl-a concentration and $c_{pg}(685)$ peak height. For this reason, we recommend this approach as a qualitative proxy, since its capability to provide quantitative estimates of Chl-a concentration should be further explored with a more extensive dataset. The potential influence of Chl-a fluorescence, which could lead to a decrease in the attenuation signal around 685 nm, was not evaluated here. Nevertheless, we assumed a minor effect since Chl-a fluorescence from the light beam leads to an emission into all directions, and therefore the amount of fluorescence into the direction of the beam towards the detector can be considered insignificant.

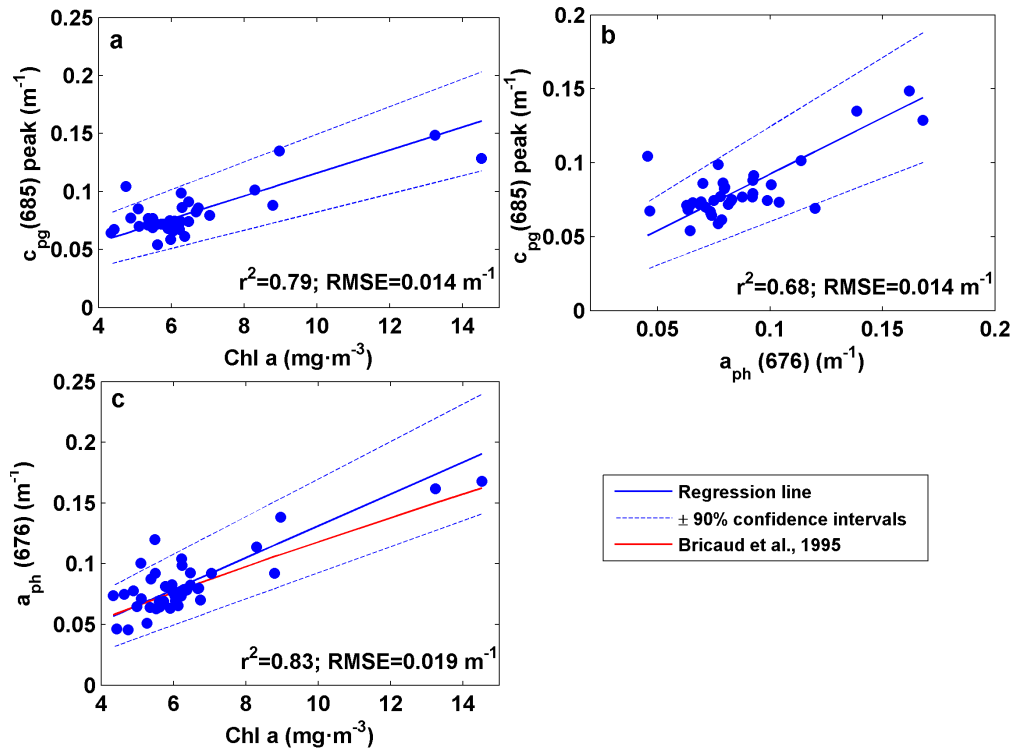


Figure 3.4: Scatter plots of (a) Chl-a concentration and $c_{pg}(685)$ peak. (b) Phytoplankton absorption at 676 nm, $a_{ph}(676)$, and $c_{pg}(685)$ peak. (c) Chl-a concentration and $a_{ph}(676)$. The red line represents the power-law fit proposed by [Bricaud *et al.* \(1995\)](#). Blue lines are the regression line $\pm 90\%$ confidence intervals.

3.3.1.3 Spectral slope of total non-water beam attenuation *vs.* $a_{CDOM}(443)$

The evolution of the attenuation spectral slope, the particle size distribution slope and the CDOM absorption at 443 nm was analyzed to evaluate the suitability of using c_{pg} slope as an indicator of CDOM content. Variations in c_{pg} slope responded mainly to changes in

$a_{CDOM}(443)$, since both parameters exhibited a fairly similar behavior although the magnitude of these variations differed. PSD slope, however, varied within a relatively narrow range (from 3.43 to 4.24), playing a smaller role in the variations observed in c_{pg} slope (Fig. 3.5-a). Note that the PSD slope of the LISST and the VIPER-derived c_{pg} slope are sensitive to different particle range given the distinct scattering angles they collect, which can contribute to the different behavior observed among both variables. In order to test whether these variations in c_{pg} slope were associated with changes in the magnitude of a_{CDOM} instead of in the CDOM absorption spectral slope, S_{CDOM} , the correlation between $a_{CDOM}(443)$ and S_{CDOM} was analyzed ($p < 0.001$). An inverse relationship was found between both variables, which is consistent with the observations from Helms *et al.* (2008) (Fig. 3.5-b). In contrast, no correlation was observed between S_{CDOM} and c_{pg} slope ($p > 0.1$). Finally, the relationship between $a_{CDOM}(443)$ and c_{pg} slope showed a significant correlation ($p < 0.001$), although the coefficient of determination was not too strong ($r^2 = 0.5$; $RMSE = 0.93$) (Fig. 3.5-c). This correlation was due to the high CDOM content in Alfacs Bay. For future studies, however, it is recommended to perform in situ measurements of $0.2 \mu m$ -filtered and unfiltered seawater alternatively to determine CDOM absorption separately (*e.g.* Boss *et al.* 2001a).

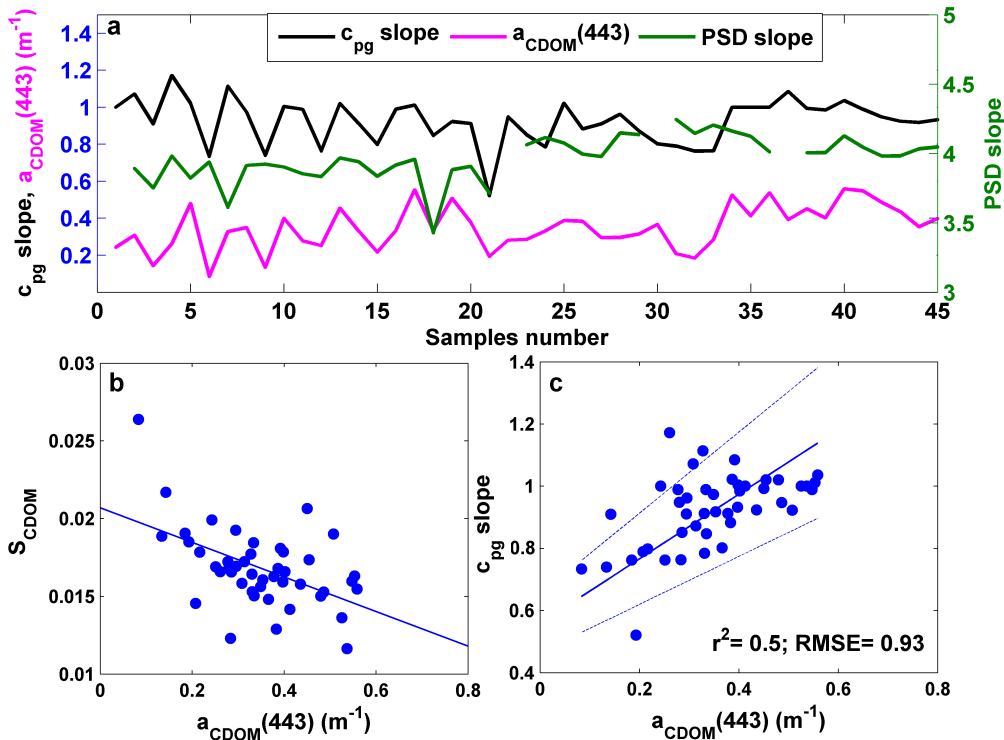


Figure 3.5: (a) Evolution of beam attenuation spectral slope (c_{pg} slope), PSD slope and CDOM absorption at 443 nm ($a_{CDOM}(443)$) along all samples. (b) Scatter plot of $a_{CDOM}(443)$ and CDOM absorption spectral slope, S_{CDOM} . (c) Scatter plot of c_{pg} slope and $a_{CDOM}(443)$. The blue lines are the regression fits.

3.3.2 Spatial variability

The horizontal and vertical spatial variability of the environmental, optical and biogeochemical parameters was analyzed based on vertical profiles measured at seven stations spread in Alfacs Bay (Fig. 3.6-a). The vertical profiles of temperature and salinity showed a stratified water column, with a fresher and warmer surface layer and an underlying cooler and saltier water layer (Figs. 3.6-b,c). The pycnocline was located at ~ 3.5 m depth, consistent with previous studies (Cerralbo *et al.* 2015, Llebot *et al.* 2013). The averaged temperature and salinity gradients between surface and bottom were of $\Delta T = 1.33^\circ\text{C}$ and $\Delta S = 1.84$, with maximal differences of 2.1°C and 2.7, respectively (found in the bay mouth).

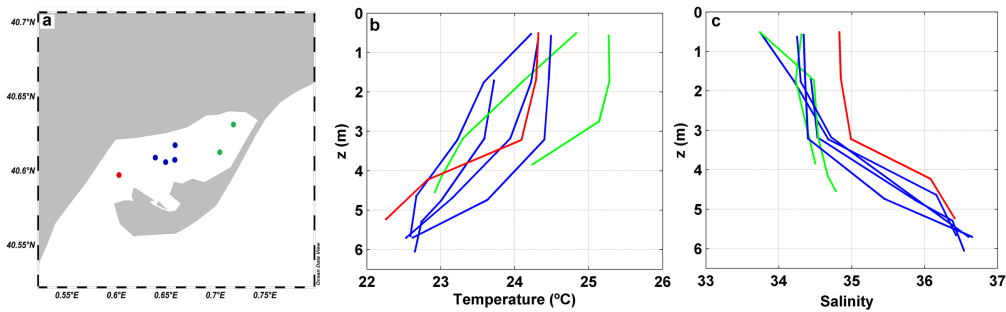


Figure 3.6: Analysis of the spatial variability in Alfacs Bay. (a) Sampling stations for the analysis of spatial patterns, with different colors according to its location: inner (green), central (blue), outer (red) region of the Bay. Map produced with Ocean Data View (ODV) software (Schlitzer 2016). (b) Temperature and (c) salinity vertical profiles measured at the seven sampling stations with colors according to Fig. 3.6-a.

The stratification of the water column determined the spatial variations observed in the optical properties. Thereby, significant differences in the beam attenuation spectra as well as in CDOM and phytoplankton absorption spectra were found between surface and bottom water layers (*i.e.* $z \leq 3.5$ m and > 3.5 m, respectively) ($p < 0.01$) (Fig. 3.7). Meanwhile, no noticeable differences were detected in the non-algal particulate absorption, $a_{nap}(\lambda)$ (not shown). Waters below the pycnocline were characterized by a higher attenuation and phytoplankton absorption, whereas CDOM absorption was lower. The shape of the particle size distribution was relatively homogeneous, although the PSD slope decreased slightly with depth (Table 3.1) ($p > 0.05$).

The analysis of the spatial patterns based on $c_{pg}(\lambda)$ measurements was carried out by using the above-mentioned attenuation spectral features - $c_{pg}(710)$, $c_{pg}(685)$ peak and c_{pg} slope- and their relationships with the underlying biogeochemistry. In general, surface waters presented steeper c_{pg} slopes and lower values of both $c_{pg}(685)$ peak and $c_{pg}(710)$. In contrast, $c_{pg}(\lambda)$ measured below the pycnocline showed the opposite behavior, although their oscillations were larger (Table 3.1, Fig. 3.8). Statistically significant differences ($p < 0.01$) between

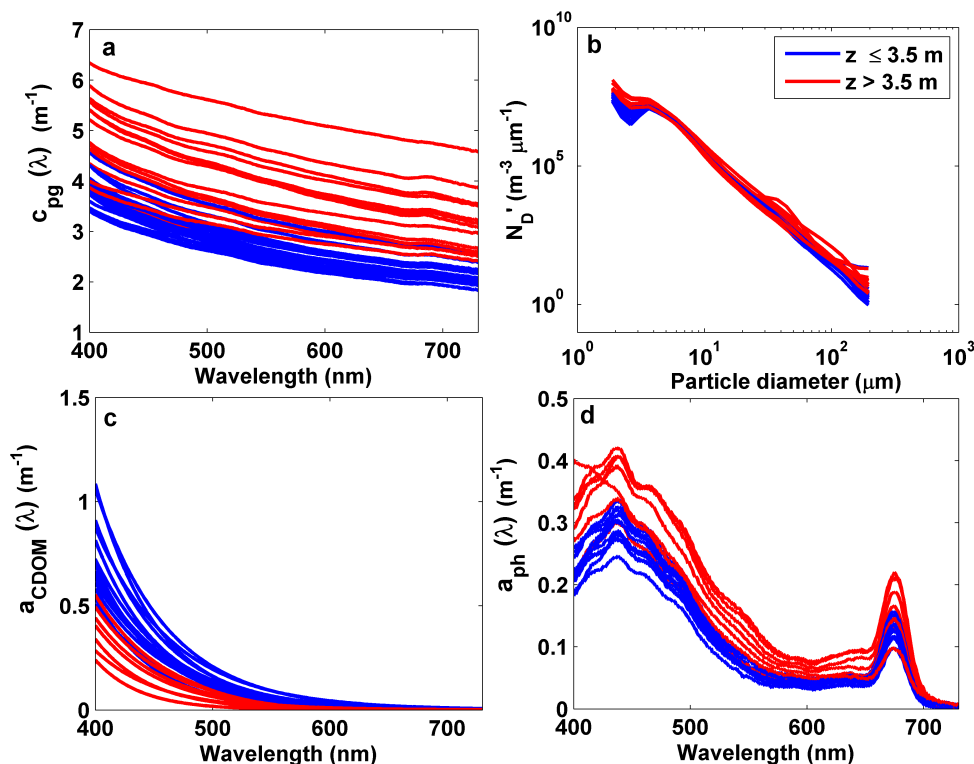


Figure 3.7: Optical properties measured at seven stations occupied in Alfacs Bay and over the water column. (a) In situ measured total non-water beam attenuation spectra. (b) LISST-derived size distribution for particle number. (c) CDOM absorption and (d) phytoplankton absorption spectra. Blue and red lines indicate measurements performed above and below the pycnocline, respectively.

surface and bottom layers were found in $c_{pg}(710)$ and c_{pg} slope, which increased by 40% and decreased by 27% with depth, respectively (Table 3.1, Fig. 3.9-a). The observed decrease in the attenuation spectral slope with depth can be associated not only with a reduction in CDOM contribution but also with resuspension events. Horizontally, except slight differences detected in the bottom layer, no significant spatial patterns were observed along the different bay regions, suggesting a horizontal homogeneity in $c_{pg}(\lambda)$ spectral features (Fig. 3.8).

On the other hand, the spatial variability observed in the biogeochemical parameters over the sampled transects were in agreement with the total non-water beam attenuation proxies, since noticeable differences were found between surface and bottom water layers for these as well. While TSM and Chl-a increased with depth, CDOM absorption decreased (Table 3.1, Fig. 3.8). However, horizontal variations observed in the attenuation proxies were less pronounced than those in the biogeochemical variables (Fig. 3.8).

Finally, the results from the laboratory-measured absorption spectra exhibited differences in optical constituents contribution between surface and bottom layers, although the averaged magnitude of the total absorption was very similar for both cases (0.82 and 0.84 m^{-1} ,

Table 3.1: Mean and standard deviation of the non-water beam attenuation-based proxies and biogeochemical variables for waters above and below the pycnocline (*i.e.* $z \leq 3.5$ m and $z > 3.5$ m, respectively).

	$Z \leq 3.5$ m		$Z > 3.5$ m	
	Mean	SD	Mean	SD
c_{pg} (710) (m^{-1})	2.12	0.16	3.53	0.55
c_{pg} (685) peak height (m^{-1})	0.074	0.007	0.12	0.024
c_{pg} slope	1.04	0.08	0.76	0.12
PSD slope	3.89	0.09	3.77	0.17
TSM ($g \cdot m^{-3}$)	3.97	1.37	9.36	3.44
Chl-a ($mg \cdot m^{-3}$)	5.28	1.44	9.47	3.73
a_{CDOM} (443) (m^{-1})	0.38	0.09	0.19	0.08

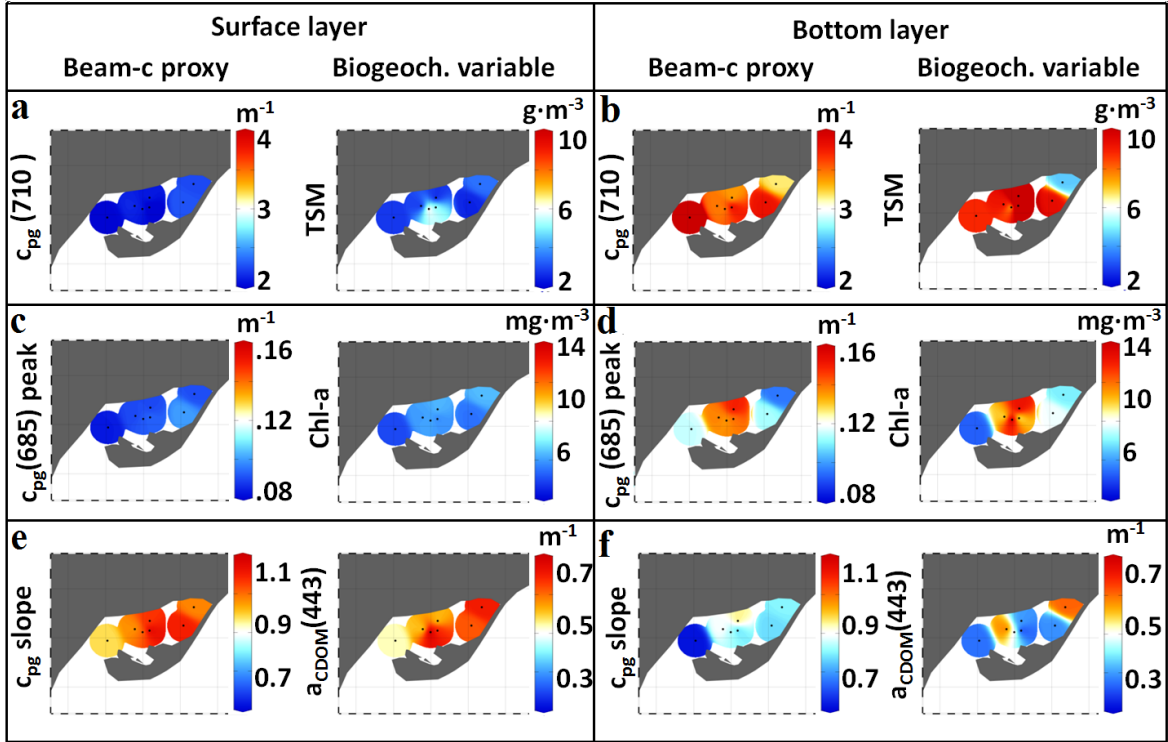


Figure 3.8: Spatial distribution of proxies from non-water beam attenuation and biogeochemical variables. Attenuation at 710 nm, $c_{pg}(710)$, *vs.* TSM at the (a) surface ($z \approx 0.5$ m) and (b) bottom ($z \approx 5$ m) layers of Alfacs Bay. $c_{pg}(685)$ peak *vs.* Chl-a concentration at the (c) surface and (d) bottom layers. c_{pg} spectral slope *vs.* CDOM absorption at 443 nm at the (e) surface and (f) bottom layers. Produced with Ocean Data View software (Schlitzer 2016).

respectively) (Fig. 3.9-a). The spatial variations found in these variables coincided with those observed from the beam attenuation-based analysis. The ternary plot of the partitioned absorption at each sampling station showed that surface waters were characterized by a higher proportion of CDOM and lower phytoplankton absorption than the water below the pycnocline, which presented larger particulate fraction (Fig. 3.9-b). These observations are consistent with a previous study in the region (Busch 2013), that found similar vertical

distribution of optically active constituents (*i.e.* Chl-a, TSM, and CDOM).

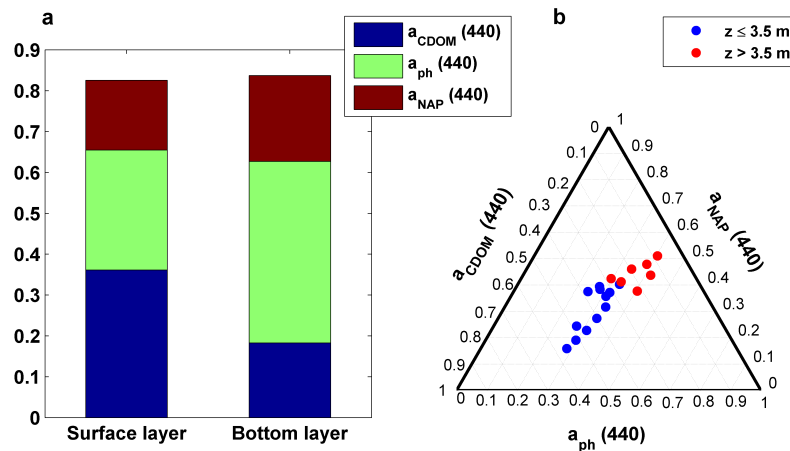


Figure 3.9: Analysis of partitioned absorption data. (a) Contribution of the major biogeochemical variables to the total non-water absorption coefficient at 440 nm for the two different water layers. (b) Ternary plot of the partitioned absorption coefficient at 440 nm (CDOM, phytoplankton, and non-algal particles) measured at the different sampling stations in Alfacs Bay. Blue and red circles correspond to water samples collected above and below the pycnocline, respectively.

3.3.3 Temporal variability

The 48 hours-time series of wind data showed a clear bimodal pattern with two dominant directions, from southwest and northwest (Figs. 3.10-a, -b). NW winds blew for ca. 10 – 12 hours during the nighttime (from 10 pm until 9:30 am, approximately) and shifted from SE to SW during daytime. The velocities reached by southern winds were $5 \text{ m} \cdot \text{s}^{-1}$ on average, with maximum values up to $8 \text{ m} \cdot \text{s}^{-1}$ in the evening (8:30 pm). The strongest winds blew from SW from 5 pm to 10 pm. The observed wind pattern responded to the typical land breeze characterized by weak nocturnal winds ($< 2 \text{ m} \cdot \text{s}^{-1}$) blowing from land, that reverses the direction and increases the intensity during the daytime (sea breeze) (Llebot, 2010; Cerralbo et al., 2015). A similar behavior was observed in the surface current velocities, indicating that the water circulation at the sampling station was driven by the prevailing wind (Fig. 3.10-c). Thereby, surface water flowed in northward direction during daytime in response to southern winds and southwards when the wind ceased during nighttime. This pattern was observed within the first 2 m depth, though the velocity decreased with depth.

The effect of hydrodynamics on the water optical properties was analyzed for time and depth, and no significant correlations ($p > 0.05$) between the optical properties and both the current velocity and direction were found. Thereby, the differences in the optical parameters between both prevailing flow regimes (*i.e.* southward and northward currents) were not statistically significant ($p > 0.05$) (Fig. 3.11).

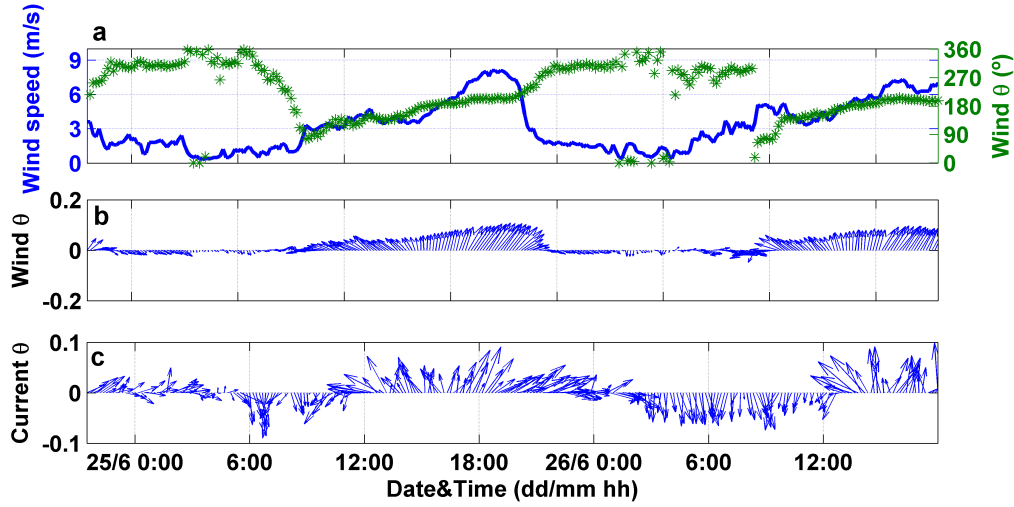


Figure 3.10: Time series of physical forcings along 48 hours. (a) Wind speed and direction measured in the weather station located in Alcanar. (b) Wind speed and direction (to) represented by arrows. Upward pointing arrow indicates the North. (c) Surface current velocity and direction represented by arrows, measured at 0.5 m depth with the ADCP located in the sampling station.

The surface current velocity (at 0.5 m depth) was $0.1 \text{ m} \cdot \text{s}^{-1}$ on average, with a maximum value of $0.2 \text{ m} \cdot \text{s}^{-1}$, coinciding with SW winds episodes (Fig. 3.12-a). In relation to the hydrographical variability, water temperature showed a marked diurnal cycle (day-night), with an oscillation of 1.2°C . It ranged from 23.2°C (registered at 4 am) to 24.4°C , at 6 pm (Fig. 3.12-b). While no significant correlations were found between physical and optical variables, the time series of $c_{pg}(710)$ and particle size distribution slope were characterized by an increase in their magnitude at periods of maximum current velocities, in response to the more intense northward currents (Figs. 3.12-a,c,f). In contrast, $c_{pg}(685)$ peak and c_{pg} spectral slope exhibited a bimodal pattern similar to that observed for the wind and current data. Both parameters rose under weak southward current conditions, whereas the minimum values concurred with the maximum current velocities flowing northwards (Figs. 3.12-a,d,e).

The temporal variations in biogeochemical properties showed similar patterns as those observed based on $c_{pg}(\lambda)$ proxies (Fig. 3.13). The concentration of particulate matter increased with current velocity within the time interval from 6 pm to 12 am, on June 25, in agreement with $c_{pg}(710)$. Nevertheless, the magnitude of this increase differed, since $c_{pg}(710)$ showed a rise of 20% with respect to the mean value, whereas a 40% increase was detected for TSM concentration (Fig. 3.13-a). Apart from this, no similar patterns were observed between both parameters along the time series, involving no significant correlation between TSM and $c_{pg}(710)$ ($p > 0.05$). In contrast, significant correlations were found between Chl-a concentration and $c_{pg}(685)$ peak ($p < 0.05$), as well as between CDOM absorption at 443 nm and the attenuation spectral slope ($p < 0.01$). The bimodal pattern detected in the optical

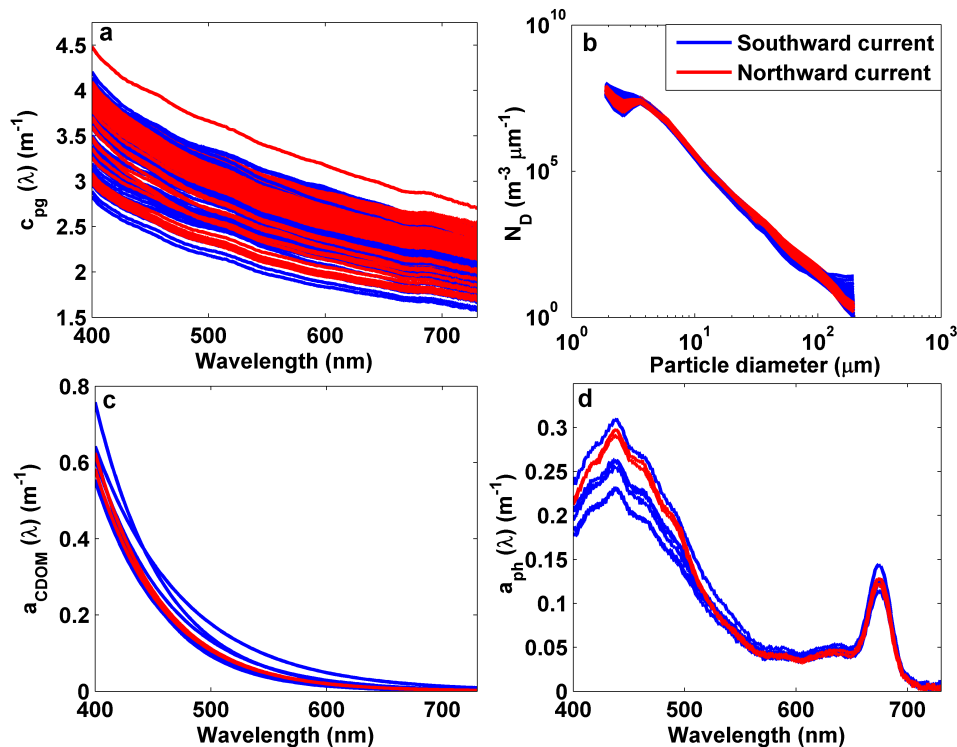


Figure 3.11: Optical measurements collected during profiling along 48 hours for the analysis of temporal patterns in Alfacs Bay. (a) In situ measured total non-water beam attenuation spectra. (b) LISST-derived size distribution for particle number. (c) CDOM absorption and (d) phytoplankton absorption spectra. Blue and red lines indicate measurements performed under the influence of southward and northward currents, respectively.

proxies was also observed within the bulk analyses of Chl-a and $a_{CDOM}(443)$. Both variables increased their magnitude during southward current conditions (*i.e.* from 12 am to 12 pm, approximately) (Figs. 3.13-b,c).

3.4 Conclusions

Continuous measurements of spectral beam attenuation coefficient collected in situ with an advanced-technology transmissometer have been proven as a powerful tool to better understand the existing interactions between physical and biogeochemical variables in the complex estuarine waters of Alfacs Bay (NW Mediterranean). In particular, this approach allowed the detection of qualitative changes in the major biogeochemical variables (*i.e.* Chl-a, TSM and CDOM) at high temporal and spatial scales in this microtidal estuary. Spatial patterns observed in the biogeochemical properties were driven by the vertical stratification of the water column. Accordingly, surface and bottom water layers were characterized by a different relative contribution of the major biogeochemical variables to the bulk beam attenuation. Meanwhile, observations along the 48 hours time series revealed a coupling between physical

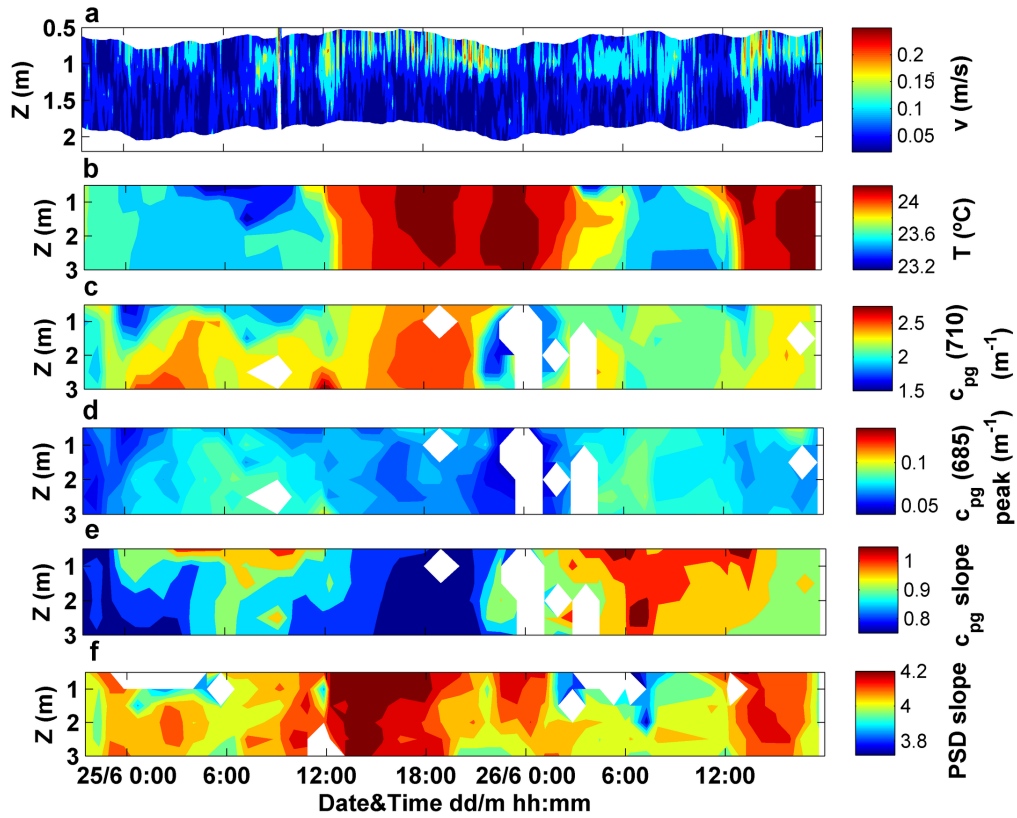


Figure 3.12: Variations with time and depth in the attenuation-based proxies and PSD slope along with the current velocity. (a) Temporal dataset of current velocity measured within the first 2 m depth. Time series of vertical profiles of (b) water temperature, (c) $c_{pg}(710)$, (d) $c_{pg}(685)$ peak, (e) c_{pg} spectral slope and (e) LISST-derived PSD slope.

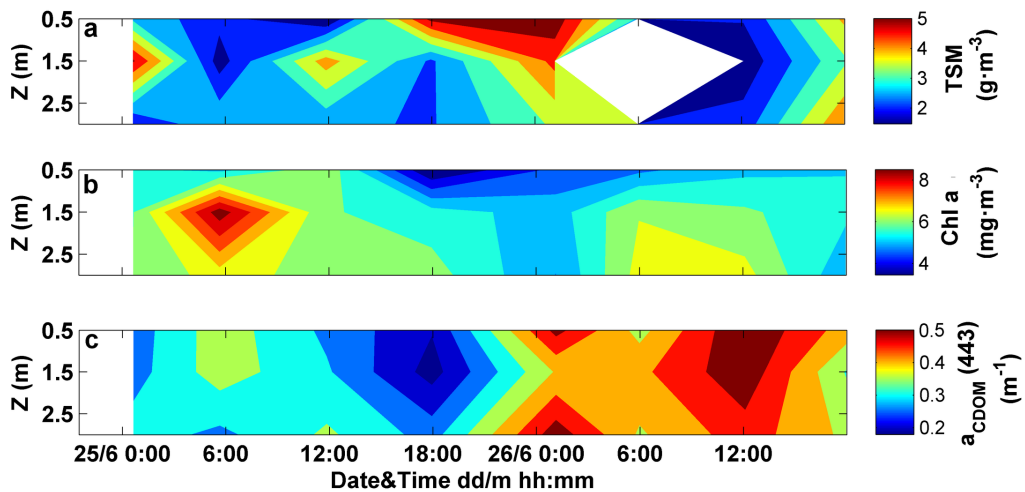


Figure 3.13: Variations with time and depth in biogeochemical variables. Time series of vertical profiles of (a) suspended matter concentration, (b) Chl-a concentration and (c) CDOM absorption at 443 nm.

Chapter 3

(meteorological and hydrodynamic conditions) and biogeochemical properties, since the prevailing hydrodynamic regimes determined the variations in water composition. The temporal and spatial patterns were obtained based on the spectral features of the total non-water beam attenuation coefficient and validated with laboratory results of discrete water samples (*i.e.* biogeochemical variables and partitioned absorption coefficients). Significant linear relationships were found between the non-water beam attenuation proxies and the biogeochemical variables. However, for future studies, it is highly recommended to include in situ beam attenuation measurements of 0.2 μm -filtered seawater for better CDOM characterization. The proposed proxies are subject to numerous uncertainties due to several factors affecting the attenuation signal (CDOM absorption and particle characteristics such as size, shape, composition, etc., which determine their absorption and scattering properties), compromising their ability to provide quantitative estimates. The collection of discrete water samples for laboratory analysis of biogeochemical variables is therefore required for validation purposes. Our results based on a high-frequency, low power ($\leq 3W$), compact, versatile (adaptable to different observing platforms) and cost-effective (~ 10000 €) beam attenuation meter, as well as on a simple and rapid data processing method, have demonstrated a capability to improve the operational monitoring of coastal waters towards a better understanding of their complex physical and biogeochemical interactions.

4

Quantitative estimates of constituent concentrations in optically complex waters by means of inversion procedure of in situ spectral attenuation and absorption measurements

The previous chapter has demonstrated the potential of spectral beam attenuation measurements to detect qualitative changes in the major non-water constituents in optically complex waters. However, it is insufficient to retrieve quantitative estimates due to the numerous factors determining the beam attenuation coefficient, including the absorption and scattering properties of the different water constituents. Consequently, additional measurements are required to be able to retrieve more extensive and quantitative information about water quality variables. For this reason, in the last chapter of this thesis, spectral absorption measurements are included in the analysis in order to evaluate how improve our capability to assess complex marine environments by combining both IOPs measurements.

In this context, a deconvolution approach is presented to use spectral absorption and attenuation data to estimate the concentration of the major non-water compounds in complex shelf sea waters. The inversion procedure requires knowledge of local material-specific inherent optical properties (SIOPs) which are determined from natural samples using a bio-optical model that differentiates between Case I and Case II waters and uses least squares linear regression analysis to provide optimal SIOP values. A synthetic data set is used to demonstrate that the approach is fundamentally consistent and to test the sensitivity to injection of controlled levels of artificial noise into the input data. Self-consistency of the approach is further demonstrated by application to field data collected in the Ligurian Sea, with chlorophyll (Chl), mineral suspended solids (MSS) and coloured dissolved organic materials (CDOM) retrieved with RMSE of $0.61 \text{ mg} \cdot \text{m}^{-3}$, $0.35 \text{ mg} \cdot \text{L}^{-1}$ and 0.02 m^{-1} respectively. The utility of the approach is finally demonstrated by application to depth profiles of in situ absorption and attenuation data resulting in profiles of optically significant constituents with associated

Chapter 4

error bar estimates. The advantages of this procedure lie in the simple input requirements, the avoidance of error amplification, full exploitation of the available spectral information from both absorption and attenuation channels and the reasonably successful retrieval of constituent concentrations in an optically complex shelf sea.

This chapter is in process to be published in: *Ramírez-Pérez M., Twardowski M., Trees C., Píera J., McKee D. (2017) Inversion of in situ absorption and attenuation measurements to estimate constituent concentrations in optically complex shelf seas. Journal of Geophysical Research. In press.*

4.1 Introduction

There is great interest in characterizing water quality over a wide range of spatial and temporal scales in shelf seas. It involves the quantification of the major constituents present in the water which includes: phytoplankton and associated biogenic detritus (usually related to chlorophyll a concentration, Chl), nonbiogenic suspended solids (often classed as mineral suspended solids, MSS, but see below for discussion of limitations in this assumption) and coloured dissolved organic material, CDOM (Kirk 1994).

As it was above mentioned, the potential to derive useful information about constituent characteristics from measured inherent optical properties (IOPs) has been demonstrated in many studies (*e.g.* Astoreca *et al.* 2012, Boss *et al.* 2001a, McKee & Cunningham 2006). However, quantification of the major non-water constituent concentrations from these measurements is still a challenging task because simple relationships vary locally with particle composition; thus a generally accepted protocol does not yet exist (Brown *et al.* 2007). The most direct method to address this issue is by means of the material-specific IOPs (SIOPs), since these parameters provide a link between IOPs and concentrations of the materials in water. Whilst this may seem straightforward, there is in fact a significant challenge in generating all of the required SIOPs as this requires (a) a suitable bio-optical model to relate available optical and biogeochemical measurements, and (b) ability to partition IOP data into constituent-related components (*e.g.* McKee & Cunningham 2006). This is partly achieved by ancillary measurements and laboratory analysis, such as filter pad spectrophotometry (to separate the absorption by phytoplankton and by non-algal particulate material) and absorption measurements of 0.2 μm filtered seawater (for deriving the absorption by CDOM). However, there is not at present any technique to separate particulate scattering and non-algal particulate absorption into biogenic and non-biogenic components. This has led some authors to determine the SIOPs based on (1) multiple linear regression of total IOPs against constituent concentrations (Brown *et al.* 2007, Strömbeck *et al.* 2003), (2) simple linear regression for data sets partitioned by optically dominant constituent (McKee & Cunningham 2006) or (3) laboratory analysis of phytoplankton cultures (Bricaud *et al.* 1983, Stramski & Morel 1990) and purified suspended minerals (Babin & Stramski 2002; 2004). The linear regression analysis proposed by McKee & Cunningham (2006) allows calculation of representative SIOPs for a specific location and is attractive as the method reduces the impact of systematic and random errors (McKee *et al.*, 2014). These authors used relationships between IOPs to identify optically distinct water types dominated by different constituents (Chl or MSS) in the studied area, which application of regression analysis to partitioned IOPs and single constituent concentrations. As there is not a simple one-to-one correspondence between observed IOPs and relevant biogeochemical constituents, determination of local SIOPs inevitably involves

pragmatic decisions on how to partition in situ data. It is important to highlight that the regression analyses discussed above consider linear relationships between IOPs and constituent concentration. This is a simplification which requires careful consideration. For example, it is well known that the chlorophyll-specific phytoplankton absorption coefficient decreases with increasing Chl concentration due to the pigment packaging effect (Bricaud *et al.* 1995). However, it is proposed here that linear regression can be performed for the ranges of chlorophyll concentration values that are relevant for shelf seas as the effect of pigment packaging will be relatively limited for these values. This obviously places a constraint over the general applicability of such an approach, but this should be viewed as a pragmatic decision that results from the need to deal with several competing requirements and the emphasis on using deconvolution for optically complex shelf waters.

There are different approaches to invert in situ IOPs measurements without using SIOPs. For example, Gallegos & Neale (2002) employed normalized absorption spectra in a matrix inversion approach, while Schofield *et al.* (2004) developed a non-linear constrained regression of bulk absorption spectra. However, these methods provide estimates of optical weights and spectral slopes for the different constituents rather than values of concentrations. For these reasons, the focus of this chapter is on developing a simple IOP inversion model based on knowledge of local SIOPs. This model utilizes all the spectral information contained in in situ absorption and attenuation data to retrieve the major non-water compound concentrations in complex shelf sea areas. SIOPs are determined from a limited number of natural samples, following an extended version of the McKee & Cunningham (2006) approach, and special attention has been paid to the impact of different sources of uncertainties in the retrieval.

4.2 Theory

4.2.1 A linear spectral deconvolution model for inversion of in situ ac-9 data

The total absorption and scattering coefficients can be written as the sum of the corresponding coefficients of individual components:

$$a(\lambda) = a_{ph}(\lambda) + a_{bd}(\lambda) + a_{nd}(\lambda) + a_{CDOM}(\lambda) + a_w(\lambda) \quad (4.1)$$

$$b(\lambda) = b_{ph}(\lambda) + b_{nd}(\lambda) + b_w(\lambda) \quad (4.2)$$

where the subscripts represent: phytoplankton (*ph*), biogenic detritus (*bd*), nonbiogenic detritus (*nd*), coloured dissolved organic material (*CDOM*) and water (*w*). This slightly awkward

Chapter 4

formulation is necessary in order to facilitate subsequent integration with measured parameters. In particular, biogenic detrital scattering is included in the phytoplankton scattering term (b_{ph}) as it is currently not possible to separate these experimentally or numerically. Equations 4.1 and 4.2 can be expressed as the product of SIOPs and constituent concentrations:

$$a(\lambda) = a_{ph}^*(\lambda) \cdot Chl + a_{bd}^*(\lambda) \cdot Chl + a_{nd}^*(\lambda) \cdot TSS_{nd} + a_{CDOM}^*(\lambda) \cdot CDOM + a_w(\lambda) \quad (4.3)$$

$$b(\lambda) = b_{ph}^*(\lambda) \cdot Chl + b_{nd}^*(\lambda) \cdot TSS_{nd} + b_w(\lambda) \quad (4.4)$$

where the constituent concentrations are: chlorophyll (Chl), the nonbiogenic detrital component of total suspended solids (TSS_{nd}) and the absorption of CDOM at 440 nm. $a_{CDOM}^*(\lambda)$ is actually the CDOM absorption spectrum normalized to the signal at 440 nm. It is assumed (e.g., Morel 1988) that biogenic variables covary with Chl. In order to maximize the spectral information content of both measurements, the scattering to absorption ratio is used:

$$\frac{b(\lambda)}{a(\lambda)} = \frac{b_{ph}^*(\lambda) \cdot Chl + b_{nd}^*(\lambda) \cdot TSS_{nd} + b_w(\lambda)}{a_{ph}^*(\lambda) \cdot Chl + a_{bd}^*(\lambda) \cdot Chl + a_{nd}^*(\lambda) \cdot TSS_{nd} + a_{CDOM}^*(\lambda) \cdot CDOM + a_w(\lambda)} \quad (4.5)$$

The equation can be simplified, grouping terms to Chl , TSS_{nd} , and $CDOM$, as follows:

$$[b(\lambda)a_{ph}^*(\lambda) - a(\lambda)b_{ph}^*(\lambda) + b(\lambda)a_{bd}^*(\lambda)] \cdot Chl + [b(\lambda)a_{nd}^*(\lambda) - a(\lambda)b_{nd}^*(\lambda)] \cdot TSS_{nd} + [b(\lambda)a_{CDOM}^*(\lambda)] \cdot CDOM = -b(\lambda)a_w(\lambda) + a(\lambda)b_w(\lambda) \quad (4.6)$$

The total absorption and scattering coefficients, $a(\lambda)$ and $b(\lambda)$, the SIOPs and the absorption and scattering of pure water, $a_w(\lambda)$ and $b_w(\lambda)$, are all known. $a_w(\lambda)$ and $b_w(\lambda)$ are taken from Pope & Fry (1997) and Morel (1974), respectively. These coefficients are also added to the ac-9 measurements to obtain the total absorption and scattering coefficients, $a(\lambda)$ and $b(\lambda)$. The chlorophyll, nonbiogenic detrital suspended sediments and CDOM concentrations (Chl , TSS_{nd} and $CDOM$ respectively), are unknowns and are found by minimizing least squares for n wavelengths, where $n \geq 3$. In this case, the system is formed by 9 equations ($n = 9$), corresponding to the nine available ac-9 wavebands. For oceanic waters (Case I waters) where the optical properties are dominated by algae and covarying materials, the

inversion model is reduced to two unknowns: Chl and CDOM.

4.2.2 Practical implementation of the spectral deconvolution model

In Case 1 waters it is assumed that the nonbiogenic detrital components of absorption and scattering are negligible. Consequently, for Case 1 waters, non-algal particulate absorption, $a_{nap}(\lambda)$, measured using bleached filter pads is classed here as biogenic detrital absorption, $a_{bd}(\lambda)$, and is assumed to correlate with Chl (and is demonstrated as such later). The corresponding SIOP, $a_{bd}^*(\lambda)$, can therefore be determined by simple linear regression. In Case 2 waters $a_{nap}(\lambda)$ is assumed to have both biogenic and nonbiogenic components. However, the biogenic component can be established from associated Chl and Case 1 estimates of $a_{bd}^*(\lambda)$ and the nonbiogenic component of NAP absorption is then given by

$$a_{nd}(\lambda) = a_{nap}(\lambda) - a_{bd}^*(\lambda) \cdot Chl \quad (4.7)$$

A similar argument allows partitioning of the Case 2 particulate scattering coefficient, $b_p(\lambda)$, into biogenic and nonbiogenic components using

$$b_{nd}(\lambda) = b_p(\lambda) - b_{ph}^*(\lambda) \cdot Chl \quad (4.8)$$

where the chlorophyll-specific phytoplankton scattering coefficient, $b_{ph}^*(\lambda)$, is previously determined for Case 1 waters using linear regression of $b_p(\lambda)$ against Chl, and includes contributions for all biogenic particles found in Case 1 waters. Finally, it is necessary to relate these two nonbiogenic detrital IOPs to the nonbiogenic detrital mass concentration, TSS_{nd} . Unfortunately this cannot be directly measured. In Case 1 waters, the total suspended solids concentration, TSS, can be assumed to be biogenic in origin, while in Case 2 waters there will also be a nonbiogenic component. Whilst combustion of filtered material to give mineral suspended solids, MSS, will remove the organic content, it will leave biogenic minerals such as diatom frustules on the filter paper. In this case it is suggested that establishing a relationship between TSS and Chl for Case 1 waters permits subsequent estimation of the biogenic component of TSS for Case 2 waters using

$$TSS_{nd} = TSS - TSS_{bd}^* \cdot Chl \quad (4.9)$$

This partitioning approach has previously been successfully demonstrated for this data set by [Bengil *et al.* \(2016\)](#), who used this data set to establish a bio-optical model for the Ligurian Sea, adopting full non-linear fits to maximize the range of compatibility. In this paper,

however, it is necessary to limit the analysis to linear fits between IOPs and constituent concentrations as the deconvolution model is solved as a system of linear equations. An advanced version, incorporating non-linear SIOP models is planned for the future, but requires significantly more complex mathematical solving processes.

4.2.3 Propagation of measurement uncertainty

A key benefit of the proposed spectral deconvolution approach is the computational simplicity of solving a system of linear equations. At the same time, there is a need to consider how uncertainties in both IOPs and SIOPs propagate through the model and the system is sufficiently complex that an analytical approach is unattractive. Under these circumstances it is suggested that statistical bootstrapping is an efficient means of assessing the propagation of errors. To do this it is necessary to establish uncertainty estimates for both IOPs and SIOPs, taking care to consider both the magnitude and the nature (*e.g.* absolute *vs* fractional) of the uncertainties. Once these are available, it is a simple matter of injecting randomly distributed errors into observations and repeatedly solving the system of equations to build up statistical distributions of constituents. The final outcome is a set of constituent concentrations that are quantified as a best estimate (median) and associated uncertainty (standard deviation of the bootstrap distribution). The ability to rapidly establish associated uncertainties in the constituent concentrations is a particularly useful aspect of this approach.

4.3 Materials and Methods

4.3.1 Field data

Sampling was performed at 36 stations in the Ligurian Sea, off the northwest coast of Italy, between 13th and 26th March 2009 on the RV Alliance during the BP09 cruise. Stations can be classified in two different groups according to location: offshore and onshore with 12 and 24 stations, respectively (Fig. 4.1). The first group was characterized by deep (up to 2500 m) oceanic waters where a spring bloom was occurring, whereas the second group belonged to the shallow coastal region, ranging from quite clear to turbid waters, including some stations within the plume of the River Arno. More detailed information about the study area can be found in McKee *et al.*(2014). At each station, vertical profiles of spectral absorption and attenuation coefficients were measured and water samples were collected simultaneously at different depths for later laboratory analysis.

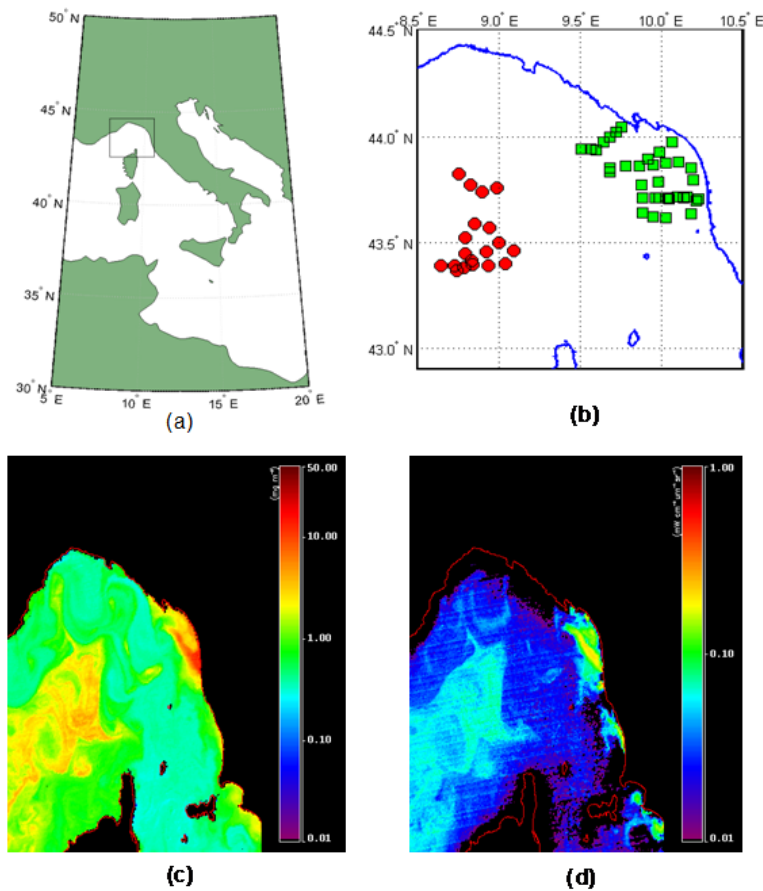


Figure 4.1: (a) Study area marked within box and (b) location of offshore (circles) and onshore (squares) stations for the BP09 cruise. (c) MODIS standard Chl from 18th March 2009 shows a bloom in the central region of the Ligurian Sea, northwest of Corsica. The high intensity “bloom” on the Italian coast is actually a sediment plume from the River Arno, which is clearly identified from (d) MODIS nLw667 from the same date.

4.3.2 In situ optical measurements

Vertical profiles of the total non-water absorption and beam attenuation coefficients were measured in situ with a WET Labs 25-cm-pathlength ac-9 instrument operating at 9 wavelengths across the visible – NIR (412, 440, 488, 510, 532, 555, 650, 676, and 715 nm, 10 nm FWHM) and data were averaged over 1-m depth intervals. AC-9 measurements were calibrated during the cruise with ultrapure water (Milli-Q, Millipore) and the salinity and temperature dependence of pure water were corrected in all samples (Pegau *et al.* 1997) using data from a Seabird SBE 19 plus CTD. The proportional correction by Zaneveld *et al.* (1994) was used to correct AC-9 absorption data for scattering collection errors. In situ backscattering measurements were made with a BB9 backscattering meter (WET Labs Inc.) operating at 412, 440, 510, 532, 595, 660, 676, 715 nm. BB9 data were linearly interpolated where necessary to match AC-9 wavelengths and were corrected for temperature, salinity and path

length absorption effects in line with the manufacturer’s instructions. Total scattering b was derived from $c - a$. Note the c measurement has an acceptance angle of 0.93 degrees, so these c and b parameters do not include scattering in the 0 to 0.93 degree solid angle. The AC-9 and BB9 were deployed simultaneously, measuring IOPs from the surface to the maximum depth possible in shallow stations or down to a maximum of 100 m for deeper stations.

4.3.3 Laboratory measurements

The absorption of all dissolved and suspended components minus water was measured using a Point Source Integrating Cavity Absorption Meter (PSICAM) (Röttgers & Doerffer 2007, Röttgers *et al.* 2005). This instrument has previously been extensively validated and has been shown to provide high accuracy ($\pm 2\%$) absorption coefficients across a wide range of water conditions. A 1 m liquid waveguide capillary cell (LWCC) with an Ocean Optics USB2000 mini-spectrometer was used to measure absorption by CDOM. This instrument is somewhat faster to operate than the PSICAM and provides noise range of $\pm 0.0001 m^{-1}$ (95% Prediction Interval) at 532 nm. In both cases, measurements were made against fresh Milli-Q references and all samples were corrected for the effects of salinity and temperature on water absorption (Röttgers & Doerffer 2007). From this pair of measurements particulate absorption, $a_p(\lambda)$, was derived by subtraction of CDOM absorption, a_{CDOM} , from PSICAM non-water absorption, a_{PSICAM} . Total particulate absorption, $a_p(\lambda)$, was measured using the quantitative filter pad method. Samples were placed directly in front of the optical windows of a Shimadzu UV-2501 PC spectrophotometer. Absorption by phytoplankton, $a_{ph}(\lambda)$, was determined by bleaching samples, measuring the absorption of non-algal particles, $a_{nap}(\lambda)$, and subtracting this from $a_p(\lambda)$. Pathlength amplification factors and scattering offset corrections were determined using a linear regression approach (Lefering *et al.* 2016) and corresponding PSICAM $a_p(\lambda)$ data. The resulting filter pad corrections were subsequently applied to both bleached and unbleached filter pad absorption spectra. Chlorophyll concentration was measured using standard HPLC measurements on samples filtered through GF/F filters, stored in liquid nitrogen and transported to laboratories for later analysis. Chl data presented here were collected by colleagues from Management Unit of the North Sea Mathematical Models (MUMM). Triplicate HPLC samples were analyzed by the Marine Chemistry Laboratory of the MUMM using a reversed phase, acetone-based method with a C18 column and a Jasco FP-1520 fluorescence detector. In this chapter Chl refers to the chlorophyll a concentration and does not include contributions from other pigments. Total suspended solids concentrations (TSS) were obtained by colleagues from MUMM by filtering samples through pre-ashed, rinsed and pre-weighed 47mm GF/F filters. Samples were rinsed with several aliquots of ultrapure water, taking care to rinse the edge of the filter to minimize salt retention. Filters were stored frozen and returned to the lab where they were dried and reweighed.

4.4 Results

Having established a conceptual framework for the spectral deconvolution approach, the aim of what follows is to demonstrate the feasibility of its parameterization and then to establish theoretical and practical performance. The stages of model development are therefore:

1. Determine an appropriate water classification scheme for the Ligurian Sea data set to support partitioning of IOPs and TSS.
2. Determine spectral SIOPs required for incorporation into Eq. 4.4. In the same process, determine associated SIOP uncertainties for inclusion into bootstrapping.
3. Establish theoretical performance for the deconvolution approach using a synthetic data set and bootstrapping to determine the effect of measurement uncertainty propagation.
4. Establish practical performance using the set of in situ IOPs and associated biogeochemical data from the Ligurian Sea.
5. Demonstrate ability to convert AC-9 depth profiles into constituent concentration depth profiles.

4.4.1 Water type classification

The Ligurian Sea data set consists of two geographically separated subsets. The offshore data set was collected in deep oceanic waters that are assumed to be Case 1 optically. The onshore data set crosses the continental shelf into coastal waters where the influence of nonbiogenic material becomes significant and the water fits a Case 2 classification. Across the entire data set Chl varied between $0.29 \text{ mg} \cdot \text{m}^{-3}$ and $3.31 \text{ mg} \cdot \text{m}^{-3}$, TSS varied from $0.13 \text{ mg} \cdot \text{l}^{-1}$ to $3.77 \text{ mg} \cdot \text{l}^{-1}$, and CDOM varied from 0.01 to 0.1 m^{-1} (at 440 nm). The distinction in optical and biogeochemical properties between onshore and offshore waters is illustrated in Fig. 4.2. Offshore stations show significantly lower particulate backscattering ratios (Fig. 4.2-a) and also lower values of TSS:Chl, both reflecting the increased significance of nonbiogenic particles for onshore stations. A best-fit linear regression forced through the origin provides an estimate of TSS_{bd}^* required for Eq. 4.9. Although there is significant spread in the data, the dashed lines provide 95% confidence intervals for this value. The question then is to what extent can this relationship be expected to work for the biogenic component of the onshore particulate population? This will largely be determined by the consistency of the phytoplankton population across the two subsets of data. Figure 4.3-a shows 440 nm normalized phytoplankton absorption spectra for the entire data set. There is remarkably little variability in the shape of these spectra, supporting the idea that the

phytoplankton properties are relatively consistent across both subsets. In this case it seems reasonable to assume that the broader biogenic properties are likely to be similarly consistent. Based on this, it will be reasonable to determine chlorophyll specific absorption coefficients for phytoplankton, $a_{ph}^*(\lambda)$, using the entire data set. Similarly, Figure 4.3-b shows 440 nm normalized CDOM absorption spectra for the entire data set, with very little obvious difference in spectral structure across the data set. Based on this it is also reasonable to use the entire data set to establish a single normalized CDOM absorption spectrum, $a_{CDOM}^*(\lambda)$.

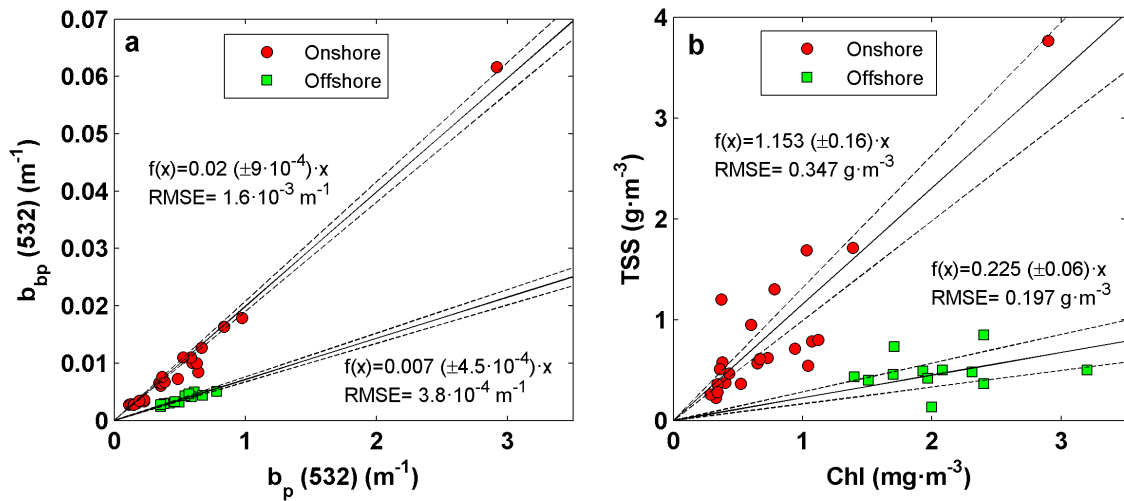


Figure 4.2: (a) Particulate backscattering against particulate scattering at 532 nm and (b) Chl against total suspended matter concentration (TSS) for all the stations from Ligurian Sea. Offshore and onshore stations marked with green squares and red circles, respectively. Black solid and dashed lines represent the best fit line forced through origin and $\pm 95\%$ confidence bounds.

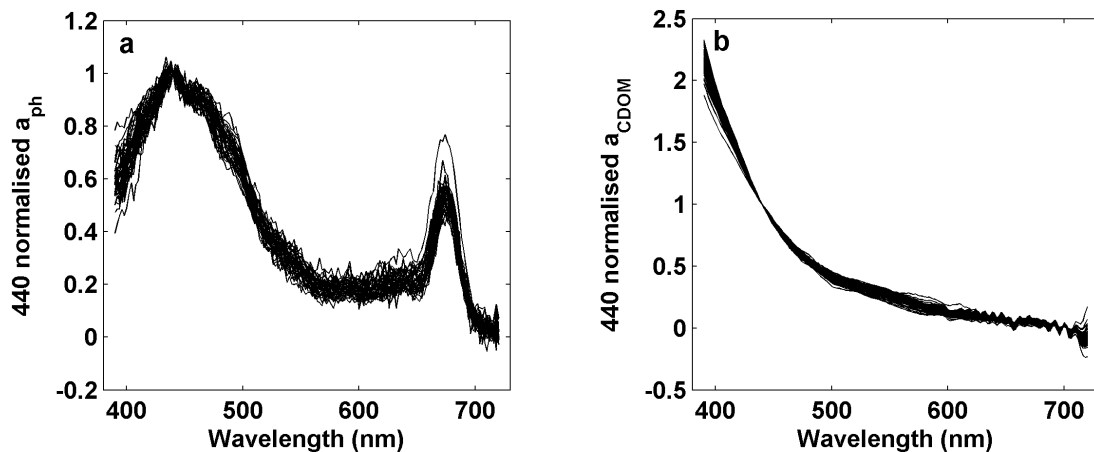


Figure 4.3: (a) Phytoplankton absorption spectra normalized at 440 nm show very little spectral variability across the entire data set. (b) 440 nm normalized CDOM spectra are also very consistent across the entire data set.

4.4.2 Determination of SIOPs and associated uncertainties

The set of material-specific absorption and scattering coefficients required to populate the spectral deconvolution model (Eq. 4.6) was derived by linear least squares regression of partitioned IOPs against associated constituent concentrations from surface water samples (Fig. 4.4). Regressions were applied for each available wavelength and were forced through the origin to avoid the complicating influence of statistical offsets. Following McKee *et al.* (2009), the regression slopes were taken as the optimal SIOP values, and the 95% confidence intervals in these slopes, $CI_{95\%}$, were considered to represent the uncertainty in each SIOP. $CI_{95\%}$ were calculated as 1.96σ and were included in the inversion procedure to quantify the product uncertainties.

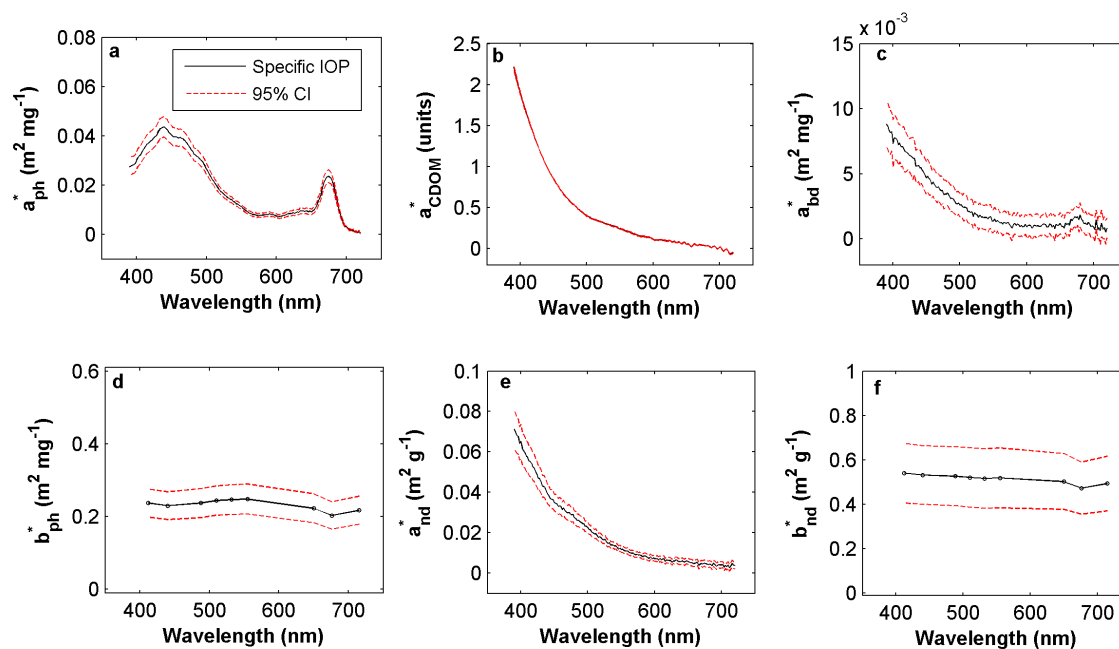


Figure 4.4: Material-specific IOPs with 95% confidence bounds obtained by linear regression: (a) Chl-specific phytoplankton absorption – full data set, (b) CDOM absorption normalized at the signal at 440 nm – full data set, (c) Chl-specific biogenic detrital absorption – offshore data set, (d) Chl-specific phytoplankton scattering – offshore data set, (e) TSS_{nd} -specific nonbiogenic detrital absorption coefficient – onshore data set, and (f) TSS_{nd} -specific nonbiogenic detrital scattering coefficient – onshore data set.

As there does not appear to be significant variability in the spectral structure of $a_{ph}(\lambda)$ or $a_{CDOM}(\lambda)$ across the data set (Fig. 4.3), the corresponding SIOPs could be derived using both the Case 1 and Case 2 parts of the data set (Figs. 4.4-a,b). Coefficients of determination (R^2) for $a_{ph}^*(\lambda)$ were 0.9 on average. 95% confidence intervals varied across the spectrum but were generally narrow (maximum $\sim 0.01 \text{ m}^2 \text{ mg}^{-1}$) and represented less than fifteen percent of the slope value for $\lambda < 700 \text{ nm}$. This linearly derived single $a_{ph}^*(\lambda)$ spectrum can be

justified by noting that Chl varied from 0.3 to 3.3 mgm^{-3} and that over this range the power law function proposed by [Bricaud *et al.* \(1995\)](#) can reasonably be approximated with a linear function. Linear regressions for $a_{CDOM}^*(\lambda)$ had an average $R^2 = 0.95$ with $CI_{95\%} < 5\%$ of corresponding signal for the majority of wavelengths.

Biogenic detrital absorption and chlorophyll-specific scattering SIOPs were derived using data from offshore stations only, assuming that these were effectively Case 1 waters. Figures 4.4-c and 4.4-d show $a_{bd}^*(\lambda)$ and $b_{ph}^*(\lambda)$ respectively, obtained by regression of $a_{nap}(\lambda)$ and $b_p(\lambda)$ against Chl for the offshore data set. Coefficients of determination for $a_{bd}^*(\lambda)$ were > 0.85 for $\lambda < 500$ nm but decreased with increasing wavelength. This is a natural consequence of the signal decreasing with wavelength. 95% confidence intervals for $a_{bd}^*(\lambda)$ were broadly constant at approximately $\pm 0.002 m^2mg^{-1}$ across the spectrum. A small peak centered on 676 nm indicates the presence of residual quantities of algal pigment due to imperfect bleaching of filters. The $b_{ph}^*(\lambda)$ spectrum shows features associated with anomalous dispersion around pigment absorption peaks. Coefficients of determination were > 0.93 across the spectrum and $CI_{95\%}$ were consistent across the spectrum at $\pm 0.4 m^2mg^{-1}$.

The nonbiogenic component of total suspended solids concentration (TSS_{nd}) for onshore stations was obtained using Eq. 4.9 and the value of TSS_{bd}^* obtained from Fig. 4.2-b. Similarly, nonbiogenic components of detrital absorption, $a_{nd}(\lambda)$, and particulate scattering, $b_{nd}(\lambda)$, were obtained for onshore stations using Eqs. 4.7 and 4.8 and biogenic SIOPs determined for offshore stations. Nonbiogenic detrital SIOPs, $a_{nd}^*(\lambda)$ and $b_{nd}^*(\lambda)$, were obtained by correlating associated IOPs with TSS_{nd} . Figure 4.4-e shows the resulting $a_{nd}^*(\lambda)$ spectrum, with the signal decreasing approximately exponentially with wavelength as expected, though there is a small, broad feature around 480 nm that might be imperfect pigment bleaching or, alternatively an unknown mineral absorption feature. Despite the additional level of processing required to reach this stage, the coefficient of determination gave an average $R^2 = 0.84$ across all wavelengths. $CI_{95\%}$ values decreased with increasing wavelength with maximum values of $\sim 0.01 m^2g^{-1}$ in the blue. $b_{nd}^*(\lambda)$ was featureless and showed only a small decrease with wavelength (Fig. 4.4-f). However this masks the fact that this set of regressions returned the lowest coefficients of determination with average $R^2 > 0.75$ across the spectrum. Normalized nonbiogenic detrital scattering spectra showed a broader range of spectral variability than any of the other IOPs in this data set. $CI_{95\%}$ values were spectrally invariant however, with an average value of $\pm 0.15 m^2g^{-1}$.

4.4.3 Spectral deconvolution model sensitivity analysis

The spectral deconvolution model represented by Eq. 4.6 is a system of linear equations operating on spectrally dependent IOPs and SIOPs to retrieve three unknown constituent

concentrations: Chl , TSS_{nd} and $CDOM$. In the case of AC-9 data, there are nine available spectral bands, providing an overdetermined system of equations that can nevertheless be easily solved in Matlab (The Mathworks, Inc.) using the *mldivide* operator that provides a least squares solution. This approach enables exploitation of all of the spectral information provided by the AC-9 sensor combination. The aim of this sensitivity analysis is to establish basic algorithm performance in the case of perfect input data and then to determine the impact of measurement uncertainties (and other sources of variability). By its nature, this is an open-ended problem so the analysis will be restricted to set ranges of constituent concentrations and a single set of measurement uncertainty ranges.

Synthetic IOPs were generated based on SIOPs derived in the previous section and different combinations of constituent concentrations according to Eqs. 4.3 and 4.4. The synthetic IOP data set comprised 1000 absorption and scattering coefficient spectra modeled using log-spaced constituent concentrations between the ranges shown in Table 4.1. AC-9 measurement uncertainties were modeled as normally distributed random values with a standard deviation $\sigma = \pm 0.0025 \text{ m}^{-1}$ corresponding to the manufacturer's estimates of the instrument precision ($\pm 0.005 \text{ m}^{-1}$). These errors were assumed to be absolute in magnitude (consistent with McKee *et al.* (2009)) and random with wavelength, so a separate error was generated for each wavelength and measurement of absorption and attenuation. Uncertainties in SIOPs were expressed as normally distributed random errors within the range $\pm 5\%$. This arbitrary value was selected as being broadly representative of the 95% confident intervals obtained from linear regressions in the previous section. A relative error was selected for the SIOPs to reflect the apparent dependence on signal observed in *e.g.* Fig. 4.4-a. Note, however, that this is a simplification only used for this sensitivity analysis. For each combination of constituents, 1000 sets of IOPs with randomly generated errors were created and propagated through the deconvolution model to produce distributions of constituent concentration estimates. The median minus the input value was used to quantify the offset error while the spread in the retrieved values was expressed as the standard deviation of the output distributions.

Table 4.1: Constituent concentration ranges used in the generation of the synthetic IOP data set.

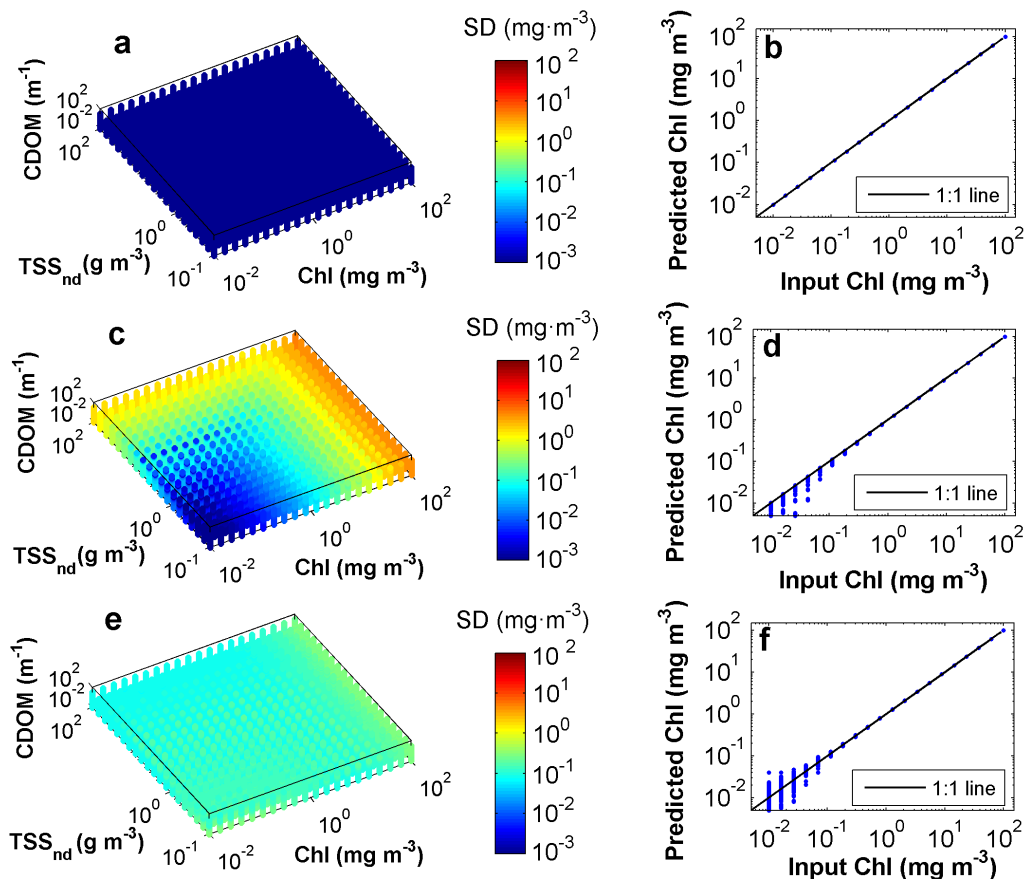
Constituent	Min	Max
$Chl \text{ (} mg \cdot m^{-3} \text{)}$	0.01	100
$TSS_{nd} \text{ (} g \cdot m^{-3} \text{)}$	0.1	100
$CDOM \text{ (} m^{-1} \text{)}$	0.01	10

The magnitude of the offset error was typically of the order of 10^{-2} - 10^{-3} (relevant units for each parameter) and only increased to significant levels when each constituent reached the very highest end of the ranges outlined in Table 4.1. For the constituent concentration ranges in the Ligurian Sea data set, the offset error can be assumed to be negligible. Fig. 4.5

shows the spread and offset errors in retrieval of Chl for all combinations of constituent concentrations for three different scenarios: (a and b) zero error in both IOPs and SIOPs, (c and d) zero error in IOPs and 5% error in SIOPs, and (e and f) $\sigma = \pm 0.0025 \text{ m}^{-1}$ error in IOPs and zero error in SIOPs. Retrieval of constituents when the input errors are zero (Figs. 4.5-a,b) is effectively perfect for the synthetic data set. This is to be expected and is merely confirmation that the Matlab *mldivide* operator is successfully dealing with the overdetermined system of equations. Introducing relative errors into the SIOPs and absolute errors into the IOPs impact differently on the distribution of retrieved Chl. The effect of a 5% relative error in SIOPs results in a spread error distribution that effectively scales with the magnitude of the constituent concentrations, though CDOM does not appear to be particularly significant (Fig. 4.5-c). Introduction of the 5% SIOP error results in offset errors in the distribution of output Chl values that increase as the concentration gets smaller and, somewhat unexpectedly, are skewed towards underestimates (Fig. 4.5-d). The effect of an absolute error in IOPs, on the other hand, is more evenly spread and potentially more significant at low concentrations for both spread and offset errors (Fig. 4.5-e,f). The salient point is that it is essential that both the magnitude and the nature (*i.e.* absolute vs relative) of errors is established in order to understand their impact on this kind of deconvolution approach. Combining both IOP and SIOP uncertainties leads to spread error distributions for each constituent that broadly scale with the magnitude of the corresponding constituent concentration (Fig. 4.6-a,-c and -e). Interestingly, the effect of combining IOP and SIOP errors is for offset errors to be reasonably uniformly spread around the 1:1 line and to become significant only at low concentrations of each constituent (Fig. 4.6-b,-d and -f). Combining IOP and SIOP errors in the deconvolution method results minimum and maximum spread (σ) and offset errors shown in Table 4.2. Both spread and offset errors are maximal when associated input concentrations are highest. So although these are in some cases large absolute values, in relative terms they are all less than 10% and in many cases much less than 1%. On the other hand, the apparently small values of minimum spread errors in Table 4.2 correspond to low input concentrations and actually represent significant relative errors, up to almost an order magnitude in the case of Chl. Overall, it seems reasonable that relative errors in constituent retrieval should increase as the contribution of that constituent to the formation of the optical signals diminishes. The retrieval of Chl at low concentrations appears to be significantly worse than for the other constituents. However, this really reflects the fact that the simulations have been performed for concentration combinations where the contribution of Chl to the formation of optical signals is almost insignificant: there is no reason to expect that such small contributions can be efficiently resolved, and this level of performance is therefore entirely within reason.

Table 4.2: Minimum and maximum standard deviations (σ) and offset errors of the retrieved variables obtained from the inversion of simulated IOPs.

Constituent	Min σ	Max σ	Max Offset error
Chl ($mg \cdot m^{-3}$)	0.08	5.02	0.47
TSS_{nd} ($g \cdot m^{-3}$)	0.047	9.32	0.68
$CDOM$ (m^{-1})	0.0029	1.41	1.28

**Figure 4.5:** Chl standard deviation distributions for the synthetic IOP data set incorporating: (a) zero error in both IOPs and SIOPs, (b) zero error in IOPs and 5% error in SIOPs, and (c) $\sigma = \pm 0.0025 m^{-1}$ error in IOPs and zero error in SIOPs.

4.4.4 Inversion of in situ IOPs at sample depths

The IOP inversion model was applied to in situ AC-9 measurements collected close to the sea surface. Since the SIOPs were previously determined using the same surface water samples, this analysis is not a rigorous test of model performance but does allow determination of how well the single set of linearly derived SIOPs represents the optical properties of the data set. As offshore and onshore stations were considered as Case I and Case II waters respectively, the inversion procedure was implemented separately to both data subsets. For Case I waters, the term related to TSS_{nd} in Eq. 4.6 was neglected, leaving only Chl and CDOM as the

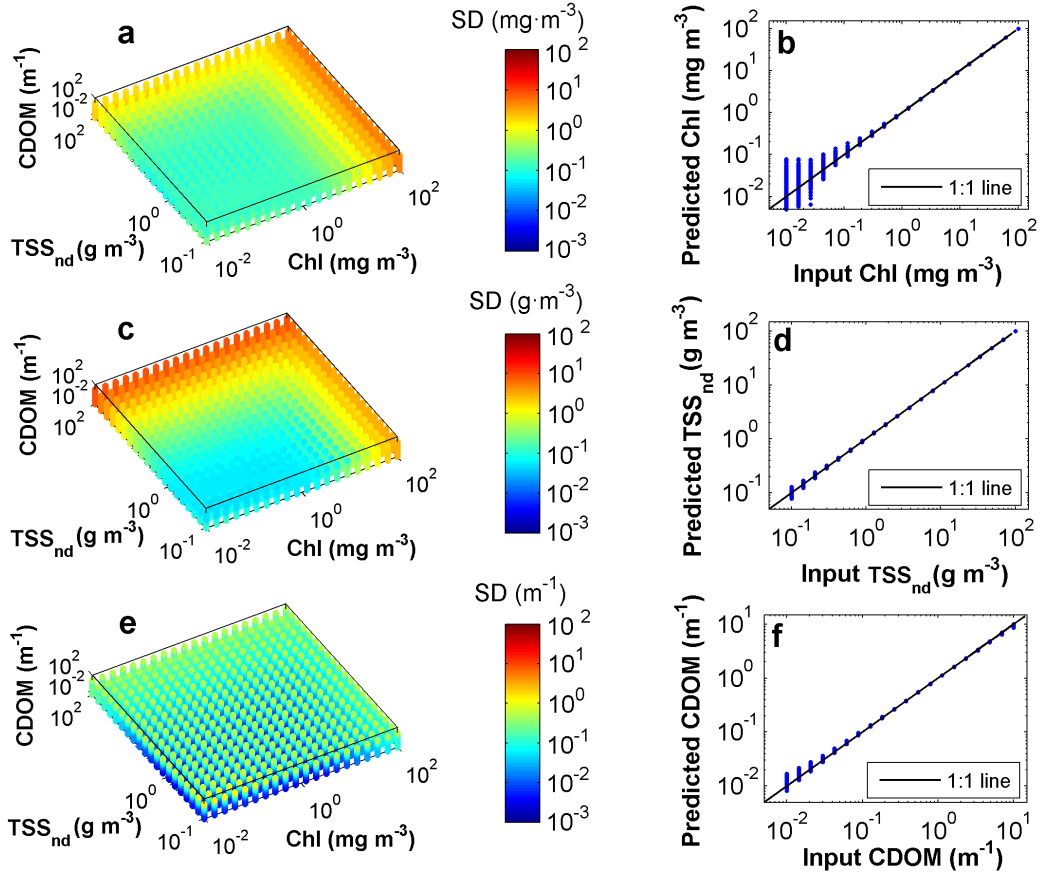


Figure 4.6: Spread and offset error distributions for Chl (a and b), TSS_{nd} (c and d), and CDOM (e and f). Results for IOP inversions with $\sigma = \pm 0.0025 \text{ m}^{-1}$ error in IOPs and 5% error in SIOPs.

model unknowns. The full set of terms in Eq. 4.6 was used in the inversion procedure for Case II waters. The bootstrap method was used to estimate uncertainties in retrieved biogeochemical variables by including random noise with $\sigma = \pm 0.0025 \text{ m}^{-1}$ for the IOPs, using the observed 95% confidence intervals for the SIOPs and repeating each calculation 1000 times to build statistically sound distributions. Figs. 4.7 and 4.8 show the comparison of retrieved and measured biogeochemical variables for Case I and II water types. The error bars are standard deviations of the bootstrap distributions. For Case I waters (Fig. 4.7) modeled Chl and CDOM were both distributed around the 1:1 line with RMSE of 0.58 mgm^{-3} and 0.008 m^{-1} respectively. In both cases, the error bars from bootstrapping were generally insufficient to explain the deviation from 1:1 which suggests that either there has been an underestimation in the magnitude of errors in the input IOPs or there is an as yet unknown factor that needs to be accounted for in the inversion procedure. The agreement between modeled and measured variables declined slightly (see RMSE values in Table 4.3) when the inversion was applied to the optically complex onshore stations (Fig. 4.8). The model tended to simultaneously overestimate Chl and underestimate TSS_{nd} , while CDOM retrieval

was generally closer to the 1:1 line but was also slightly overestimated as its concentration increased. RMSE errors for the retrieval of Chl , TSS_{nd} and $CDOM$ using the in situ IOP data set are given in Table 4.3. Note the increase in the magnitude of the Chl and $CDOM$ errors and introduction of systematic deviations from the 1:1 line moving from the Case I to Case II model, presumably reflecting the influence of including the additional TSS_{nd} parameterization in the Case II version. The introduction of systematic errors for Case II retrievals, where there appears to be some sort of mutual compensation in the recovery of each parameter, requires particular further attention and is discussed in more detail later.

Table 4.3: RMSE errors obtained from the inversion of in situ AC-9 measurements of offshore and onshore stations from Ligurian Sea.

Constituent	Case I (offshore)	Case II (onshore)
Chl ($mg \cdot m^{-3}$)	0.58	0.61
TSS_{nd} ($g \cdot m^{-3}$)	—	0.35
$CDOM$ (m^{-1})	0.008	0.02

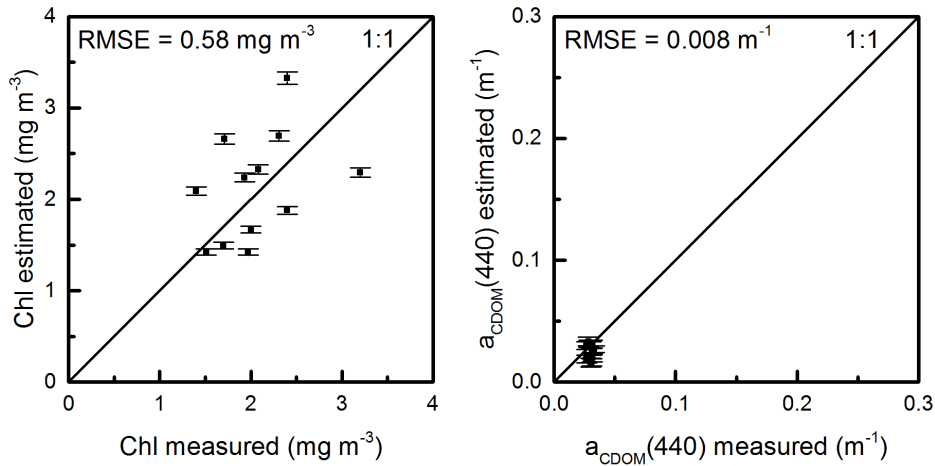


Figure 4.7: Comparison of retrieved versus measured (a) Chl and (b) $CDOM$ for offshore stations (Case I waters model). The error bars are standard deviations of bootstrap distributions.

4.4.5 Deconvolution of vertical IOP profiles

The inversion model was applied to depth profiles of in situ AC-9 measurements collected at the onshore stations. The retrieved vertical structures of Chl , TSS_{nd} and $CDOM$ with associated uncertainties are shown in Figs. 4.9, 4.10 and 4.11. Results from laboratory analyses of discrete water samples (including deep samples not previously used for SIOP generation) are also presented for validation with the modeled constituent concentrations. Chl and $CDOM$ profiles are broadly consistent with measured values through the water column, though this agreement generally declined for the shallower stations. Measured TSS_{nd} data were only available for surface waters, which therefore precludes the possibility of validating the verti-

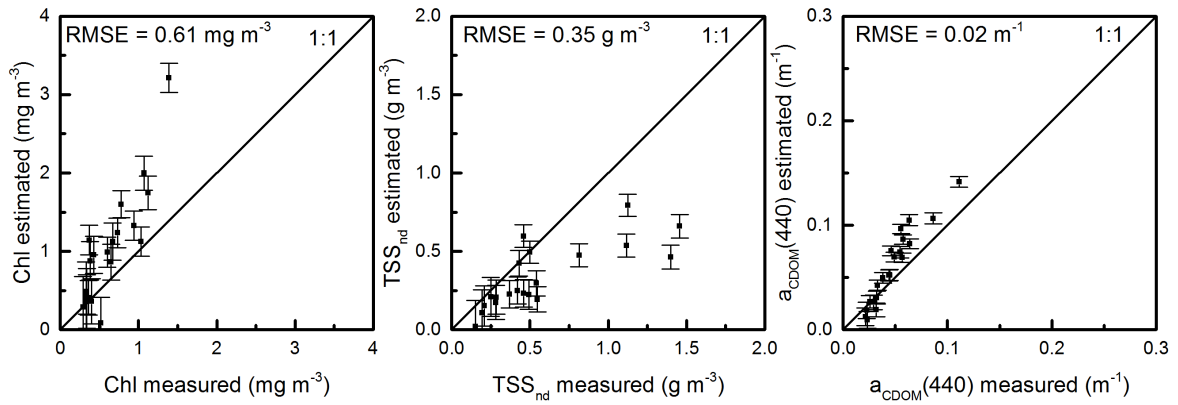


Figure 4.8: Comparison of retrieved versus measured (a) *Chl*, (b) TSS_{nd} and (c) *CDOM* for onshore stations (Case II waters model). The error bars are standard deviations of bootstrap distributions.

cal distributions of this variable. It is interesting to note, however, that the shallower stations show characteristic increases in TSS_{nd} towards the sea bottom, consistent with resuspension of sediment near the sea bed. Furthermore, deeper stations (close to or even over the shelf edge) exhibited a homogeneous vertical distribution and consistently low values of $TSS_{nd} < 0.22 \text{ gm}^{-3}$, e.g. stations #1, #2, #3 and #6.

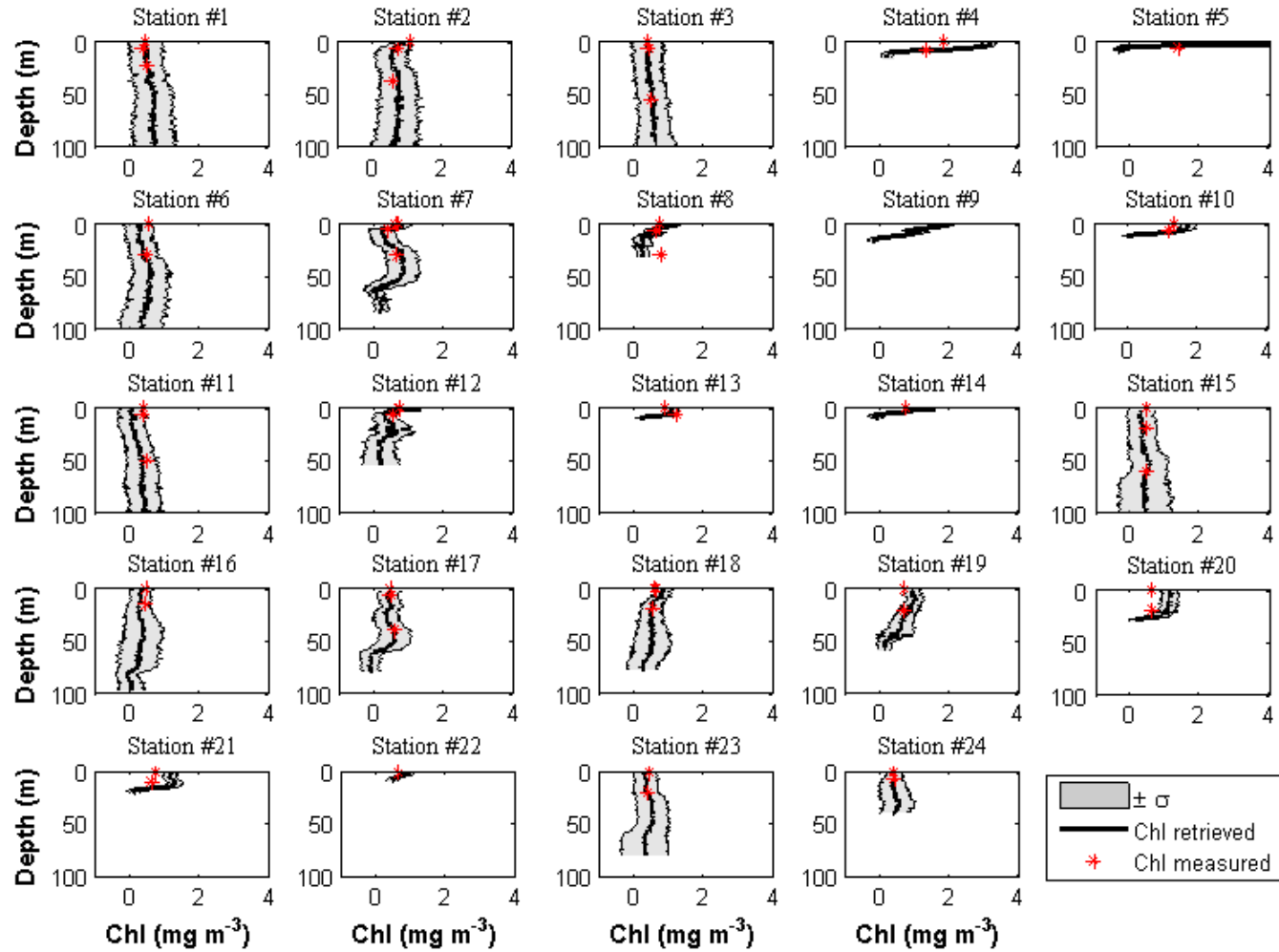


Figure 4.9: Chl depth profiles from onshore stations in the Ligurian Sea retrieved from the inversion of AC-9 measurements. Retrieved values are shown as thick black lines with shadow areas representing bootstrap standard deviations. Red stars indicate results from laboratory analyses of water samples.

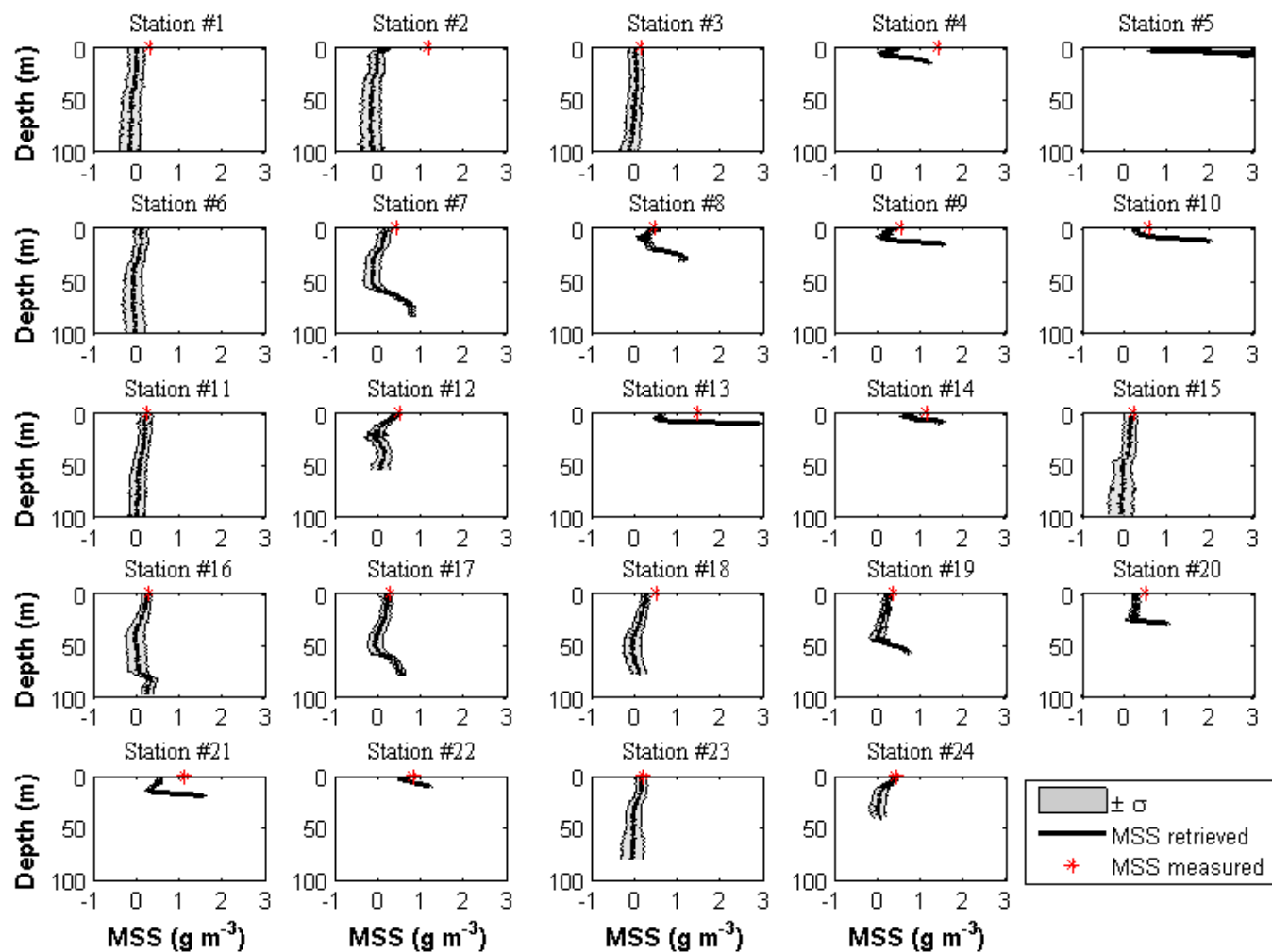


Figure 4.10: TSS_{nd} depth profiles from onshore stations in the Ligurian Sea retrieved from the inversion of AC-9 measurements. Retrieved values are shown as thick black lines with shadow areas representing bootstrap standard deviations. Red stars indicate results from laboratory analyses of water samples.

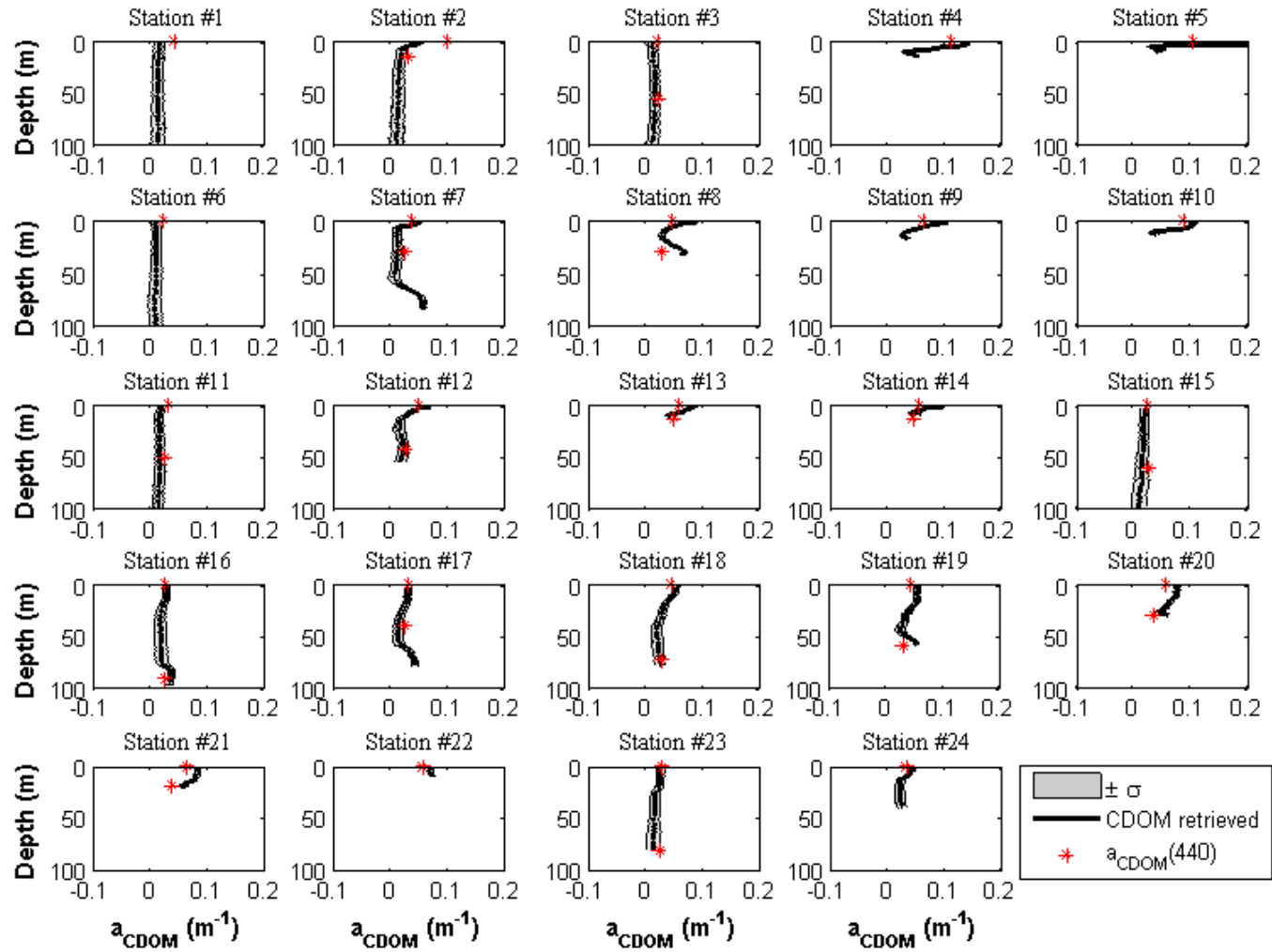


Figure 4.11: CDOM depth profiles from onshore stations in the Ligurian Sea retrieved from the inversion of AC-9 measurements. Retrieved values are shown as thick black lines with shadow areas representing bootstrap standard deviations. Red stars indicate results from laboratory analyses of water samples.

4.5 Discussion

The spectral deconvolution approach developed here is built on a simple four component bio-optical model (water, phytoplankton, mineral or nonbiogenic particles, and CDOM) that is conceptually as close to a standard model for Case II as currently exists. The deconvolution method seeks to exploit all of the spectral information that an AC-9 instrument is able to provide and it has been shown that in the case of a perfect data set it is capable of returning essentially perfect estimates of the required biogeochemical concentrations (Fig. 4.5-a). Of course it is expected that real data sets will contain measurement uncertainties, and it has been shown using a synthetic IOP data set that the effect of introducing such uncertainties into the deconvolution process is primarily to introduce a spread error into the results, with offset errors being found to be practically negligible in comparison. If the proposed bio-optical model is a reasonable representation of the natural system, one might hope, therefore, to observe retrieved biogeochemical constituents that have a spread centered on the 1:1 line when plotted against real sample data. Indeed this is the case for the Case I data set (Fig. 4.7) where both Chl and CDOM retrieved values are scattered around the 1:1 line. However, the Case II retrievals (Fig. 4.8) deviate from this scenario and show trends towards over and under-estimation for different parts of the data set. Given that the deconvolution approach has been shown to perform well for an internally consistent synthetic data set, and to be relatively tolerant to the effects of IOP and SIOP measurement uncertainties, at least in terms of offset errors, the question that arises is: what is the source of these trends away from the 1:1 line within the Case II data set? There are a number of factors that could potentially influence the performance of the deconvolution approach.

The deconvolution approach was built upon an assumption that partial IOPs could be expressed as linear products of the relevant SIOPs and constituent concentrations (Eqs. 4.3 and 4.4). It is well known, however, that there are a variety of factors that may influence such relationships in practice, with the phytoplankton pigment packaging effect perhaps being the best known (Bricaud *et al.* 1995). The model may therefore be insufficient in its representation of such effects. This is true and a nonlinear version of the approach could be developed but would have to incorporate more sophisticated solution methods. In fact this is anticipated as an area for future research effort. However, the fact that the Case I results are spread around the 1:1 line suggests that this might not be the missing factor as it would be expected to influence both data sets. The influence of changes in pigment packaging on SIOPs is most likely to be significant for data sets that extend from truly oligotrophic to eutrophic waters and span a broader range of Chl concentrations than is the case here.

Quantification and propagation of measurement uncertainties of IOPs and SIOPs also may not be optimal. In an earlier study (McKee *et al.* 2009) the range of measurement uncer-

tainty for AC-9 particulate scattering was found to be significantly greater ($\sim \times 4$) than the $\sigma = \pm 0.0025 \text{ m}^{-1}$ used here. Increasing this uncertainty estimate would increase the range of the error bars for each constituent retrieval, but would not significantly affect the central position of the output distribution. Therefore it does not explain the systematic deviation from 1:1 observed for the Case II data set. The linear regression approach to deriving SIOPs has previously been shown to mitigate the impact of individual uncertainties in IOPs and constituent concentrations (McKee *et al.*, 2014). Errors in measured constituent concentrations have not been directly addressed above, but are surely a significant factor in determining the spreads observed in Figs. 4.7 and 4.8. Again, however, it is unclear how this would generate the systematic deviations observed for the Case II data set.

This then requires a more fundamental problem to be addressed. The underpinning bio-optical model assumes three non-water components whose optical properties must be consistent across the relevant data sets. This appears to be a reasonable proposition for both the Chl and the CDOM components as (a) single linear regressions of $a_{ph}(\lambda)$ vs Chl and $a_{CDOM}(\lambda)$ vs $a_{CDOM}(440)$ provide high coefficients of determination, and (b) the retrieval of both constituents in Case I waters is not biased from the 1:1 line. This leaves the non-biogenic particulate material as a prime suspect. It was noted above that normalized non-biogenic detrital scattering spectra showed a broader range of spectral variability than any of the other IOPs. This data is shown in Fig. 4.12. It can be seen that whilst the $b_{nd}^*(\lambda)$ spectrum (Fig. 4.4-f) does capture the most commonly occurring spectral dependency, there is in fact a fairly wide range of spectral variability in this parameter that is not adequately addressed by single SIOP spectrum. Considering the location of Case II stations and the position of the Arno Plume (Figs. 4.1-b,d), it is possible that there are two (possibly more) nonbiogenic particle types in this region perhaps corresponding to plume and benthic sediment populations. Failure to adequately parameterize this level of population complexity has the potential to disrupt the retrieval of not only TSS_{nd} , but also Chl and $CDOM$ through compensation effects.

4.6 Conclusions

The conceptual framework of a novel and simple spectral deconvolution approach has been developed and shown to perform well in theory with idealized data and within quantifiable boundaries for data subject to realistic measurement uncertainties. For both Case I and Case II waters, the approach returns estimates of biogeochemical variables that are broadly consistent with the RMSE predictions from the earlier analysis of synthetic data. However the performance in Case II waters is marred by apparent tendencies to deviate from the 1:1 line that are inconsistent with the synthetic data set predictions. The most likely source of

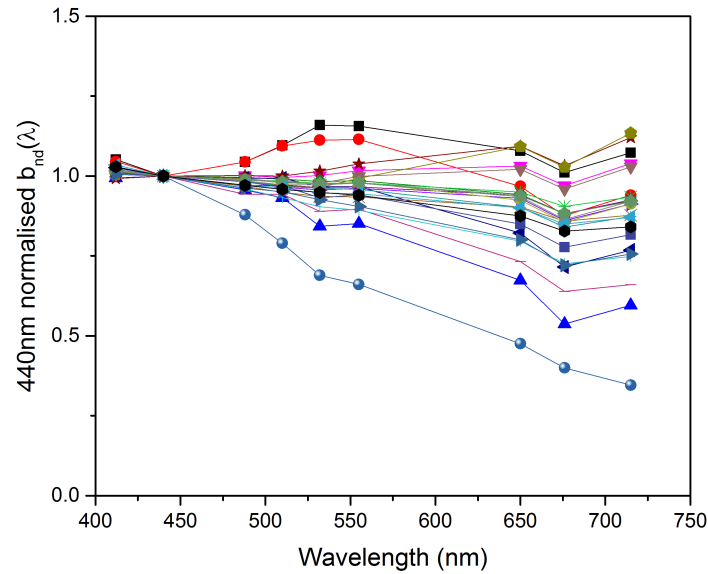


Figure 4.12: The nonbiogenic detrital scattering coefficient, $b_{nd}(\lambda)$, normalized at 440 nm shows considerable spectral variability that is potentially due to mixing of variable concentrations of two or more sub-populations.

unforeseen error is in the parameterization of the nonbiogenic particle population which in this case is potentially influenced by the presence of material associated with the River Arno plume as well as marine sediments. Whilst the overall model performance is encouraging in terms of RMSE errors, and provides potentially valuable new capability for converting IOP profiles into biogeochemical depth distributions, this study highlights the need to fully capture all of the optically significant and distinct components in a given system. The spectral deconvolution approach developed here could easily accommodate extension of the simple four component model to include additional components. Adding further spectral IOP information through *e.g.* moving from AC-9 to AC-S data (9 to 70+ wavelengths) could potentially extend the capacity to resolve such additional components. However, the limiting factor is likely to be ability to determine the SIOPs of additional components. The IOP and constituent partitioning approach used in this study is less easily extended to include resolution of additional components. Development of libraries of SIOPs for naturally occurring sub-populations and generally developing a better understanding of the true variability in SIOPs are both important future steps that would support further development of this type of deconvolution approach, and facilitate transition from local as at present to global applicability in the future.

Chapter 4

5

Conclusions and outlook

The last chapter summarizes the major contributions of this thesis and describe potential applications and the directions for future research.

5.1 Summary of contributions

The overall aim of this thesis was to investigate new observational approaches based on in situ measurements of beam attenuation coefficient to fulfill the urgent demand for sustained and routine characterization of optically complex waters. With this purpose, this study explored for the first time, the potential of advanced-technology transmissometers and exploited all the information contained in the attenuation spectrum by means of two different approaches. This thesis was conducted to address two general questions posed in Chapter 0, whose answers are detailed as follow:

1. *How much information of biogeochemical constituents can be retrieved from in situ spectral beam attenuation measurements in optically complex waters?*

It is well known that the magnitude of the beam attenuation coefficient at long visible wavelengths responds to the concentration of particulate matter, whereas the spectral slope is related to the particle size distribution slope and CDOM content. Furthermore, we found that the attenuation peak at 685 nm -associated with red-band chlorophyll absorption as result of anomalous dispersion- is highly correlated with the chl-a concentration. Thus, variations in particles and chl-a concentrations in an estuarine bay were successfully detected based on spectral attenuation data. Given that CDOM was the dominant water compound in this bay and complementary measurements of particle size distribution were available, the attenuation spectral slope was used to assess variations in CDOM content. This last proxy should be considered with caution, due to the inability to separate the contributions of CDOM and particulate attenuation from the total non-water attenuation coefficient. Therefore, spectral beam attenuation measurements have proven an effective tool to obtain an overview of changes and patterns in the optically active constituents in complex waters, but it provided limited information to retrieve more extensive and quantitative estimates. These capabilities increased remarkably when including simultaneous measurements of the absorption coefficient. This allowed to satisfactorily and rapidly quantify the concentration of the major non-water compounds (CDOM, chl-a and mineral suspended solids) as well as to obtain the associated error bar estimates.

2. *Can optical transmissometers provide a potential tool to address the actual needs of high resolution and cost-effective observing systems for optically complex waters?*

Advances in sensor technology have enabled to assess marine waters at time-spaces scales which were not possible before and thus, to obtain previously unavailable environmental information. For this reason, this kind of sensors offer a promising solution to accomplish the current observational requirements for coastal environments. The

results presented in this thesis depicted that the incorporation of advanced-technology transmissometers in coastal observing platforms is worthwhile, because of the distinct features of these devices and the useful biogeochemical information contained in the attenuation spectrum. Nevertheless, as it was above mentioned, the combination of these transmissometers with additional optical sensors (such as absorption meters) is highly recommended in order to obtain more extensive and accurate environmental information.

The work has yielded to three peer reviewed papers, which are the three main chapters of this thesis. The goals set out at the beginning of this document were accomplished through these three main Chapters.

5.1.1 Summary and contributions of Chapter 2: “*Characterization of advanced-technology transmissometers: performance and uncertainty analyses*”:

- Recent advances in sensor technology has led to the development of a new generation of optical transmissometers characterized by hyperspectral resolution, cost-effectiveness, small size and low-power consumption. The operational capabilities of these devices have therefore significantly improved, allowing their sustained and autonomous deployment aboard a variety of observing platforms. An example of this kind of sensors is the recently commercially available VIS-Photometer VIPER (TriOS, GmbH), which is the focus of this study.
- The distinct characteristics of these transmissometers have been achieved by using an array of different LEDs as light source to provide a full visible-light spectrum and a micro-spectrometer as detector. In the specific case of the first version of the VIPER (TriOS, GmbH), this configuration was found to exhibit some limitations:
 - The non-uniformity in the emitted light intensity and the open-path configuration produced ambient light contamination under specific sea surface conditions.
 - Spectral artifacts in the range 420 – 440 nm were frequently observed as result of a poor temperature compensation of one of the integrated LEDs. It occurred due to the specific mounting configuration of this LED (*i.e.* it is a SMD (Surface Mounted Design) LED with ball lens) and the use of a single internal temperature sensor.
 - The detector acceptance angle is smaller than the divergence of the beam source (0.8° and 1.33° , respectively), which implies that part of the light exiting the source is not collected by the receiver.

- Despite these limitations, VIPER provided reliable beam attenuation measurements in coastal waters (with attenuation values higher than 1.6 m^{-1}), as demonstrated from the comparison with other transmissometers.
- The acquisition of high quality data is crucial to be able to obtain high quality results. For this reason, future versions of VIPER instrument should focus on solving the observed limitations, in order to provide more accurate beam attenuation measurements and extend its application to clearer waters. Furthermore, the development of a detailed manual and a technical specification sheet would be also required.

5.1.2 Summary and contributions of Chapter 3: “*Application of cost-effective spectral beam attenuation measurements to assess changes and patterns in biogeochemical variables in a coastal environment*”:

- The spatial distribution and temporal variability of the major in-water constituents (*i.e.* CDOM, Chl-a and suspended particles) were determined based on high-resolution spectral beam attenuation measurements collected in situ with an advanced-technology transmissometer in the estuarine waters of Alfacs Bay (NW Mediterranean).
- The combination of this optical measurement with physical (temperature and salinity) and hydrodynamic variables (current velocity and direction) allowed a better understanding of the existing interactions between physical and biogeochemical processes in Alfacs Bay.
- The analysis focused on three major spectral features of the beam attenuation coefficient (*i.e.* the spectral slope, the peak height observed at 685 nm and the attenuation coefficient at 710 nm), which were successfully correlated with the three biogeochemical variables (CDOM, Chl-a and total suspended matter concentrations, respectively).
- This approach allowed the qualitative detection of changes and patterns in the biogeochemical variables, whereas it is insufficient to derive quantitative estimates due to the numerous factors affecting the beam attenuation signal.

5.1.3 Summary and contributions of Chapter 4: “*Quantitative estimates of constituent concentrations in optically complex waters by means of inversion procedure of in situ spectral attenuation and absorption measurements*”:

- Many coastal oceanographic applications such as water quality management require the quantification of the major in-water constituents at wide range of time-space scales, which involves that additional optical data beyond the beam attenuation are needed.

- In order to quantitatively estimate the major in-water constituents, a novel and simple spectral deconvolution approach was developed using exclusively in situ spectral attenuation and absorption measurements and local material-specific inherent optical properties (SIOPs) as model inputs.
- The material-specific inherent optical properties were determined from natural samples using a bio-optical model that differentiated between Case I and Case II waters and used least squares linear regression analysis to provide optimal SIOP values.
- The inversion procedure consisted of a system of n linear equations (where n is the number of wavelengths available in the absorption and attenuation meters), which presented the advantage of avoidance of error amplification, as demonstrated from the sensitivity analysis performed with synthetic data subject to realistic measurement uncertainties.
- The model provided reasonably successful retrieval of constituent concentrations, although deviations from 1:1 line were observed in the optically complex waters, which probably derived from errors in the parameterization of the nonbiogenic particle population.

5.2 Applications and future research

This thesis presented two different beam attenuation-based approaches, which can be considered complementary. The use of cost-effective and compact transmissometers provides a comprehensive overview of the heterogeneity -in terms of optically active constituents- of the marine study area, allowing the determination of the time-space scales of variability of these constituents and the better understanding of the physical and biogeochemical interactions. This information is highly valuable to define the optimal sampling strategy (*e.g.* the location of the sampling stations or the sampling frequency) which can be adopted for the second proposed approach based on sophisticated and widely validated dual spectrophotometers. Using these instruments, the inversion procedure of absorption and attenuation data is performed to derive quantitative estimates of the major in-water constituents, which are greatly needed for water quality managers and the oceanographic community.

In terms of future work, the following points describe some ideas to consider for further investigations:

- The application of cost-effective and compact transmissometers for analyzing changes in the concentration of optically active constituents in coastal regions requires complementary measurements of 0.2 μm filtered seawater for proper CDOM characterization. Thereby, in the case of transmissometers with open-path configuration, the

installation of a flow tube (with the corresponding cartridge filter and water pump) is greatly needed. Otherwise, the development of optical transmissometers covering the UV-visible spectral regions could be worthwhile, because of the particularly important contribution of CDOM absorption in the UV wavebands. Both methods seek to separate CDOM absorption from the bulk attenuation in order not only to analyze the CDOM content reliably, but also to derive useful information of the particle size distribution from the particulate attenuation spectral slope.

- The correlation found between the attenuation 685nm-peak and the Chl-a concentration in Alfacs Bay should be further explored due to the novelty and potential of this proxy. Therefore, a more extensive dataset should be used, covering a wider range of Chl concentrations and including different physiological states and composition of phytoplankton, in order to determine the reliability of this approach.
- The improvement in the IOPs inversion model performance in optically complex waters requires a better characterization of the material-specific IOPs (SIOPs), that are specific for each study area. With this purpose, it is necessary a better understanding of the true variability in SIOPs and the development of libraries of SIOPs for naturally occurring sub-populations. Furthermore, a nonlinear version of this approach could be developed in order to account for the nonlinearity between some of the material-specific IOPs and the corresponding constituent concentrations (*e.g.* the phytoplankton-specific absorption coefficient).
- As future perspectives, it is expected that the rapid technological advances will lead to considerably improved sensor features, including significant lower prizes and power consumption and reduced sizes, which indeed will improve the capabilities of these sensors. Furthermore, absorption meters with similar characteristics as the advanced transmissometers will be also developed. In fact, the recently-developed OSCAR absorption meter (from TriOS GmbH) fulfills these specific characteristics. This therefore allows to merge the two approaches presented here into one, since the estimation of the major in-water constituents concentrations in complex waters could be carried out by means of advanced-technology and cost-effective IOPs devices.

Bibliography

- AAS, E. (1984). Influence of shape and structure on light scattering by marine particles. Tech. rep., Institute of Geophysics, University of Oslo. [18](#)
- AGRAWAL, Y.C. (2005). The optical volume scattering function: Temporal and vertical variability in the water column off the new jersey coast. *Limnology and Oceanography*, **50**, 1787–1794. [29](#)
- AGRAWAL, Y.C. & POTTSMITH, H.C. (2000). Instruments for particle size and settling velocity observations in sediment transport. *Marine Geology*, **168**, 89–114. [53](#)
- ASANO, S. (1979). Light scattering properties of spheroidal particles. *Applied Optics*, **18**, 712–723. [19](#)
- ASTORECA, R., DOXARAN, D., RUDDICK, K., ROUSSEAU, V. & LANCELOT, C. (2012). Influence of suspended particle concentration, composition and size on the variability of inherent optical properties of the southern north sea. *Continental Shelf Research*, **35**, 117–128. [32](#), [71](#)
- AUSTIN, R. & PETZOLD, T. (1977). Light in the sea. vol. 3, chap. Considerations in the design and evaluation of oceanographic transmissometers, 104–120, J E Tyler. [27](#)
- BABIN, M. & STRAMSKI, D. (2002). Light absorption by aquatic particles in the near-infrared spectral region. *Limnology and Oceanography*, **47**, 911–915. [26](#), [71](#)
- BABIN, M. & STRAMSKI, D. (2004). Variations in the mass-specific absorption coefficient of mineral particles suspended in water. *Limnology and Oceanography*, **49**, 756–767. [71](#)
- BABIN, M., MOREL, A., SICRE, V.F., FELL, F. & STRAMSKI, D. (2003). Light scattering properties of marine particles in coastal and open ocean waters as related to the particle mass concentration. *Limnology and Oceanography*, **48**, 843–859. [26](#)
- BADER, H. (1970). The hyperbolic distribution of particle sizes. *Journal of Geophysical Research*, **75**, 2822–2830. [17](#)
- BAKER, E.T. & LAVELLE, J.W. (1984). The effect of particle size on the light attenuation coefficient of natural suspensions. *Journal of Geophysical Research*, **89**, 8197–8203. [32](#)

- BARLOW, R.G., CUMMINGS, D.G. & GIBB, S.W. (1997). Improved resolution of mono- and divinyl chlorophylls a and b and zeaxanthin and lutein in phytoplankton extracts using reverse phase c-8 hplc. *Oceanographic Literature Review*, **45**, 1362. [54](#)
- BARTZ, R.J., ZANEVELD, J.R. & PAK, H. (1978). A transmissometer for profiling and moored observations in water. *Society of Photo-optical Instrument Engineers*, **160**, 102–108. [26](#), [27](#)
- BEHRENFELD, M.J. & BOSS, E. (2006). Beam attenuation and chlorophyll concentration as alternative optical indices of phytoplankton biomass. *Journal Marine Research*, **64**, 431–451. [50](#)
- BENGIL, F., MCKEE, D., BESIKTEPEC, S.T., CALZADO, V.S. & TREES, C. (2016). A bio-optical model for integration into ecosystem models for the ligurian sea. *Progress in Oceanography*, **49**, 1–15. [74](#)
- BERDALET, E., ROSS, O.N., SOLÉ, J., ARTIGAS, M.L., LLAVERIA, G., LLEBOT, C., QUE-SADA, R., PIERA, J. & ESTRADA, M. (2010). Multidisciplinary and multiscale approach to understand (harmful) phytoplankton dynamics in a nw mediterranean bay. In *ICES CM*, 2. [50](#)
- BLOUGH, N.V. & VECCHIO, R.D. (2002). Biogeochemistry of marine dissolved organic matter. chap. Chromophoric DOM in the coastal environment, 509–546, Acad Press, Amsterdam. [20](#)
- BOSS, E., PEGAU, W.S., GARDNER, W.D., ZANEVELD, J.R.V., BARNARD, A.H., TWARDOWSKI, M.S., CHANG, G.C. & DICKEY, T.D. (2001a). Spectral particulate attenuation and particle size distribution in the bottom boundary layer of a continental shelf. *Journal of Geophysical Research*, **106**, 9509–9516. [17](#), [25](#), [32](#), [50](#), [55](#), [60](#), [71](#)
- BOSS, E., TWARDOWSKI, M.S. & HERRING, S. (2001b). Shape of the particulate beam attenuation spectrum and its inversion to obtain the shape of the particulate size distribution. *Applied Optics*, **40**, 4885–4893. [56](#)
- BOSS, E., COLLIER, R., LARSON, G., FENNEL, K. & PEGAU, W.S. (2007). Measurements of spectral optical properties and their relation to biogeochemical variables and processes in crater lake, crater lake national park, or. *Hidrobiologia*, **574**, 149–159. [32](#)
- BOSS, E., SLADE, W.H., BEHRENFELD, M. & DALL’OLMO, G. (2009a). Acceptance angle effects on the beam attenuation in the ocean. *Optics Express*, **17**, 1535–1550. [43](#), [46](#)
- BOSS, E., TAYLOR, L., GILBERT, S., GUNDERSEN, K., HAWLEY, N., JANZEN, C., JOHENG-GEN, T., PURCELL, H., ROBERTSON, C., SCHAR, D.W.H., SMITH, G.J. & TAMBURRI,

- M.N. (2009b). Comparison of inherent optical properties as a surrogate for particulate matter concentration in coastal waters. *Limnology and Oceanography: Methods*, **7**, 803–810. [45](#), [50](#), [57](#)
- BRICAUD, A. & MOREL, A. (1986). Light attenuation and scattering by phytoplanktonic cells: a theoretical modeling. *Applied Optics*, **25**, 571–580. [25](#), [56](#)
- BRICAUD, A., MOREL, A. & PRIEUR, L. (1981). Absorption by dissolved organic matter of the sea (yellow substance) in the uv and visible domains. *Limnology and Oceanography*, **26**, 43–53. [19](#)
- BRICAUD, A., MOREL, A. & PRIEUR, L. (1983). Optical efficiency factors of some phytoplankters. *Limnology and Oceanography*, **28**, 816–832. [71](#)
- BRICAUD, A., BABIN, M., MOREL, A. & CLAUSTRE, H. (1995). Variability in the chlorophyll-specific absorption coefficients of natural phytoplankton: Analysis and parameterization. *Journal of Geophysical Research*, **100**, 321–332. [58](#), [59](#), [72](#), [81](#), [91](#)
- BROWN, I., CUNNINGHAM, A. & MCKEE, D. (2007). An approach to determining shelf seawater composition by inversion of in situ inherent optical property measurements. In *Proceedings of the Oceans*. [71](#)
- BUGNOLO, D.S. (1960). On the question of multiple scattering in the troposphere. *Journal of Geophysical Research*, **65**, 879–884. [46](#)
- BUI TEVELD, H., HAKVOORT, J.H.M. & DONZE, M. (1994). The optical properties of pure water. In *SPIE, Ocean Optics XII*, vol. 2258, 174–183. [19](#)
- BUKATA, R.P., JEROME, J.H., KONDRATYEV, K.Y. & POZDNYAKOV, D.V. (1995). *Optical properties and remote sensing of inland and coastal waters*. 362, CRC Press. [13](#), [21](#), [22](#)
- BUSCH, J.A. (2013). *Phytoplankton dynamics and bio-optical variables associated with Harmful Algal Blooms in aquaculture zones*. Doctoral thesis, University of Bremen. [51](#), [55](#), [63](#)
- CAMP, J. & DELGADO, M. (1987). Hidrografia de las bahías del delta del ebro. *Investigaciones Pesqueras*, **51**, 351–369. [51](#)
- CAMPBELL, D.E. & SPINRAD, R.W. (1987). The relationship between light attenuation and particle characteristics in a turbid estuary. *Estuarine, Coastal and Shelf Science*, **25**, 53–65. [32](#)
- CERRALBO, P., GRIFOLL, M., VALLE-LEVINSON, A. & ESPINO, M. (2014). Tidal transformation and resonance in a short, microtidal mediterranean estuary (alfacs bay in ebre delta). *Estuarine, Coastal and Shelf Science*, **145**, 57–68. [51](#)

- CERRALBO, P., GRIFOLL, M. & ESPINO, M. (2015). Hydrodynamic response in a microtidal and shallow bay under energetic wind and seiche episodes. *Journal of Marine Systems*, **149**, 1–13. [51](#), [61](#)
- COSTANZA, R., D'ARGE, R., DE GROOT ANS S FARBER, R., GRASSO, M., HANNON, B., NAEEM, S., LIMBURG, K., PARUELO, J., O'NEILL, R.V., RASKIN, R., SUTTON, P. & VEN DEN BELT, M. (1997). The value of the world's ecosystem services and natural capital. *Nature*, **387**, 253–260. [6](#)
- DAVIS, R.F., MOORE, C.C., ZANEVELD, J.R.V. & NAPP, J.M. (1997). Reducing the effects of fouling on chlorophyll estimates derived from long-term deployments of optical instruments. *Journal of Geophysical Research*, **102**, 5851–5855. [56](#)
- DICKEY, T. & FALKOWSKI, P. (2002). The sea. chap. Solar energy and its biological-physical interactions in the sea, 401–440, Harvard University Press. [32](#)
- DIEHL, P. & HAARDT, H. (1980). Measurement of the spectral attenuation to support biological research in a “plankton tube” experiment. *Oceanologica Acta*, **3**, 89–96. [17](#), [32](#)
- D'SA, E.J., STEWARD, R.G., VODACEK, A., BLOUGH, N.V. & PHINNEY, D. (1999). Determining optical absorption of colored dissolved organic matter in seawater with a liquid capillary waveguide. *Limnology and Oceanography*, **44**, 1142–1148. [29](#)
- DUCHA, J. & KUBIN, S. (1976). Measurement of in vivo absorption spectra of microscopic algae using bleached cells as a reference sample. *Archiv fuer Hydrobiologie, Supplement*, **49**, 199–213. [25](#)
- ELECTROSPELL (2015). ElectrosPELL white leds. <http://www.electrosPELL.com/GatewayPages/WhiteLEDs.html>. [46](#)
- ESTAPA, M.L., BOSS, E., MAYER, L.M. & ROESLER, C.S. (2012). Role of iron and organic carbon in mass-specific light absorption by particulate matter from louisiana coastal waters. *Limnology and Oceanography*, **57,1**, 97–112. [23](#)
- FERRARI, G.M. & TASSAN, S. (1999). A method using chemical oxidation to remove light absorption by phytoplankton pigments. *Journal of Phycology*, **35**, 1090–1098. [54](#)
- FRY, E.S. (2000). Visible and near ultraviolet absorption spectrum of liquid water. *Applied Optics*, **39**, 2743–2744. [19](#)
- FRY, E.S., KATTAWAR, G.W. & POPE, R.M. (1992). Integrating cavity absorption meter. *Applied Optics*, **31**, 2055–2065. [29](#)

- GALLEGOS, C.L. & NEALE, P.J. (2002). Partitioning spectral absorption in case 2 waters: discrimination of dissolved and particulate components. *Applied Optics*, **41**, 4220–4233. [72](#)
- GARCÉS, E., DELGADO, M. & CAMP, J. (1997). Phased cell division in a natural population of *dinophysis* and the in situ measurement of potential growth rate. *Journal of Plankton Research*, **19**, 2067–2077. [51](#)
- GARDNER, W.D., WALSH, I.D. & RICHARDSON, M.J. (1993). Biophysical forcing and particle production and distribution during a spring bloom in the north atlantic. *Deep Sea Research*, **40**, 171–195. [25](#)
- GAZZAZ, N.M., YUSOFF, M.K., JUAHIR, H., RAMLI, M.F. & ARIS, A.Z. (2013). Water quality assessment and analysis of spatial patterns and temporal trends. *Water Environment Research*, **85**, 751–766. [32](#)
- GERNEZ, P., ANTOINE, D. & HUOT, Y. (2011). Diel cycles of the particulate beam attenuation coefficient under varying tropic conditions in the northwestern mediterranean sea: Observations and modeling. *Limnology and Oceanography*, **56**, 17–36. [56](#)
- GIBBS, R.J. (1974). Suspended solids in water. chap. Principles of studying suspended materials in water, 3–15, Plenum. [26](#)
- GIBBS, R.J. (1977). Clay mineral segregation in the marine environment. *Journal of Sedimentary Petrology*, **47**, 237–243. [16](#)
- GONÇALVES-ARAÚJO, R., STEDMON, C.A., HEIM, B., DUBINENKOV, I., KRABERG, A., MOISEEV, D. & BRACHER, A. (2015). From fresh to marine waters: Characterization and fate of dissolved organic matter in the lena river delta region, siberia. *Frontiers in Marine Science*, **2**, 1–13. [54](#)
- GREEN, R.E., SOSIK, H.M. & OLSON, R.J. (2003). Contributions of phytoplankton and other particles to inherent optical properties in new england continental shelf waters. *Limnology and Oceanography*, **48**, 2377–2391. [50](#)
- GREENBERG, A.E., CLESCERI, L.S. & EATON, A.D. (1992). Standard methods for the examination of water and wastewater. Tech. rep., American Public Health Association (APHA). [29](#)
- HAMAMATSU (2014). Hamamatsu micro-spectrometer. <http://www.hama-matsu.com/jp/en/C12666MA.html>. [36](#)
- HELMS, J.R., STUBBINS, A., RITCHIE, J.D. & MINOR, E.C. (2008). Absorption spectral slopes and slope ratios as indicators of molecular weight, source, and photobleaching of chromophoric dissolved organic matter. *Limnology and Oceanography*, **53**, 955–969. [60](#)

- HILL, P.S., BOSS, E., NEWGARD, J.P., LAW, B.A. & MILLIGAN, T.G. (2011). Observations of the sensitivity of beam attenuation to particle size in a coastal bottom boundary layer. *Journal of Geophysical Research*, **116**. 56, 57
- HOBI LABS (2011). *A-Sphere In-Situ Spectrophotometer User's Manual*. 36
- IOC-UNESCO (2012). Requirements for global implementation of the strategic plan for coastal goos. <http://unesdoc.unesco.org/ulis>. 50
- JERLOV, N.G. (1951). *Optical Measurement of Particle Distribution in the Sea*. 3, Tellus. 9
- JERLOV, N.G. (1976). *Marine Optics*. 231, Elsevier. 17, 26, 32, 54
- JERLOV, N.G. (1978). The optical classification of sea water in the eutrophic zone. Tech. rep., Kobenhavns University. Institute of Fys Oceanography, Copenhagen. 26
- JONASZ, M. (1983). *Particle size distribution in the Baltic*. 35, Tellus B. 53
- JOUON, A., OUILLOU, S., PASCAL, D., LEFEBVRE, J.P., FERNANDEZ, J.M., MARI, X. & FROIDEFOND, J.M. (2008). Spatio-temporal variability in suspended particulate matter concentration and the role of aggregation on size distribution in a coral reef lagoon. *Marine Geology*, **256**, 36–48. 53
- KENNISH, M. (2001). Practical handbook on marine science. Tech. Rep. 3, Marine Science Series. 14
- KENNISH, M. (2002). Environmental threats and environmental future of estuaries. *Environment Conservation Journal*, **29**, 78–107. 6
- KERKER, M. (1969). *The scattering of light*. Academic Press Inc, New York. 18
- KIRK, J.T.O. (1980). Spectral absorption properties of natural waters: contribution of the soluble and particulate fractions to light absorption in some inland waters of southeastern australia. *Australian Journal of Marine and Freshwater Research*, **31**, 287–296. 9
- KIRK, J.T.O. (1983). *Light and Photosynthesis in Aquatic Ecosystems*. 401, Cambridge University Press, New York. 14, 24
- KIRK, J.T.O. (1994). *Light and Photosynthesis in Aquatic Ecosystems*. Cambridge University Press, 2nd edn. 11, 71
- KIRK, J.T.O. (1997). Point-source integrating-cavity absorption meter: theoretical principles and numerical modeling. *Applied Optics*, **36**, 6123–6128. 29

- LEE, Z., LANCE, V.P., SHANG, S., VAILLANCOURT, R., FREEMAN, S., LUBAC, B., HARGREAVES, B.R., CASTILLO, C., MILLER, R., TWARDOWSKI, M. & WEI, G. (2011). An assessment of optical properties and primary production derived from remote sensing in the southern ocean (so gasex). *Journal of Geophysical Research*, **116**, C00F03. [32](#)
- LEFERING, I., BENGIL, F., TREES, C., RÖTTGERS, R., BOWERS, D., NIMMO-SMITH, A., SCHWARZ, J. & MCKEE, D. (2016). Optical closure in marine waters from in situ inherent optical property measurements. *Optics Express*, **24**, 14036–14052. [77](#)
- LLEBOT, C. (2010). *Interactions between physical forcing, water circulation and phytoplankton dynamics in a microtidal estuary*. Doctoral thesis, University of Las Palmas de Gran Canaria. [51](#)
- LLEBOT, C., RUEDA, F.J., SOLÉ, J., ARTIGAS, M.L. & ESTRADA, M. (2013). Hydrodynamic state in a wind-driven microtidal estuary (alfacs bay). *Journal of Sea Research*, **85**, 263–276. [51](#), [61](#)
- LOISEL, H. & MOREL, A. (1998). Light scattering and chlorophyll concentration in case 1 waters: A reexamination. *Limnology and Oceanography*, **43**, 847–858. [50](#)
- LOUCHARD, E.M., REID, R.P., STEPHENS, C.F., DAVIS, C.O., LEATHERS, R.A. & DOWNES, T.V. (2002). Derivative analysis of absorption features in hyperspectral remote sensing data of carbonate sediments. *Optics Express*, **10**, 1573–1584. [50](#)
- LUBAC, B., LOISEL, H., GUISELIN, N., ASTORECA, R., ARTIGAS, L.F. & MERIAUX, X. (2008). Hyperspectral and multispectral ocean color inversions to detect phaeocystis globosa blooms in coastal waters. *Journal of Geophysical Research*, **113**, C06026. [50](#)
- MALONE, T., DAVIDSON, M., DIGIACOMO, P., GONCALVES, E., KNAP, T., MUELBERT, J., PARSLow, J., SWEIJD, N., YANAGAI, J. & YAP, H. (2010). Climate change, sustainable development and coastal ocean information needs. *Procedia Environmental Sciences*, **1**, 324–341. [6](#)
- MARTÍNEZ, M.L., INTRALAWAN, A., VÁZQUEZ, G., PÉREZ-MAQUEO, O., SUTTON, P. & LANDGRAVE, R. (2007). The coasts of our world: Ecological, economic and social importance. *Ecological Economics*, **63**, 254–272. [6](#)
- MAX, J.J. & CHAPADOS, C. (2010). Infrared transmission equations in a five media system: gas and liquid. *Journal of Mathematical Chemistry*, **47**, 590–625. [39](#), [40](#), [41](#)
- MCCAVE, I.N. (1983). Particulate size spectra, behavior, and origin of nephloid layers over the nova scotia continental rise. *Journal of Geophysical Research*, **88**, 7647–7666. [25](#)

- McKEE, D. & CUNNINGHAM, A. (2006). Identification and characterisation of two optical water types in the Irish Sea from in situ inherent optical properties and seawater constituents. *Estuarine Coastal and Shelf Science*, **68**, 305–316. [71](#), [72](#)
- McKEE, D., CHAMI, M., BROWN, I., CALZADO, V.S., DOXARAN, D. & CUNNINGHAM, A. (2009). Role of measurement uncertainties in observed variability in the spectral backscattering ratio. a case study in mineral-rich coastal waters. *Applied Optics*, **48**, 4663–4675. [80](#), [82](#), [91](#)
- MEA (2005). Ecosystems and human well-being: Current state and trend. Tech. rep., Island Press, Washington DC, USA. [6](#)
- MIE, G. (1908). Beiträge zur Optik trüber Medien, speziell kolloidaler Metallösungen. *Annalen der Physik*, **330**, 337–445. [24](#)
- MOBLEY, C.D. (1994). *Light and water, radiative transfer in natural waters*. Academic Press Inc. [11](#), [12](#), [14](#), [15](#), [22](#), [23](#), [24](#)
- MOORE, C., ZANEVELD, J.R.V. & KITCHEN, J.C. (1992). Preliminary results from an in situ spectral absorption meter. In *SPIE, Ocean Optics XI*, vol. 1750, 330–337. [29](#)
- MOORE, C., BARNARD, A., FIETZEK, P., LEWIS, M.R., SOSIK, H.M., WHITE, S. & ZIELINSKI, O. (2009). Optical tools for ocean monitoring and research. *Ocean Science*, **5**, 661–684. [8](#), [27](#)
- MOREL, A. (1973). Diffusion de la lumière par les eaux de mer: Résultats expérimentaux et approche théorique. *A GARD Lecture Series*, **61**, 1–76. [17](#), [24](#)
- MOREL, A. (1974). Optical properties of pure water and pure seawater. In *Optical aspects of Oceanography*, 1–24, Academic New York. [xi](#), [23](#), [73](#)
- MOREL, A. & AHN, Y.H. (1990). Optical efficiency factors of free-living marine bacteria: influence of bacterioplankton upon the optical properties and particulate organic carbon in oceanic waters. *Journal of Marine Research*, **48**, 145–175. [15](#)
- MOREL, A. & BRICAUD, A. (1981). Theoretical results concerning light absorption in a discrete medium, and application to specific absorption of phytoplankton. *Deep Sea Research*, **28A**, 1375–1393. [24](#)
- MOREL, A. & BRICAUD, A. (1986). Inherent optical properties of algal cells, including picoplankton. theoretical and experimental results. *Canadian Bulletin of Fisheries and Aquatic Science*, **214**, 521–559. [19](#)

- MOREL, A. & GENTILI, B. (1991). Diffuse reflectance of oceanic waters: Its dependence on sun angle as influenced by the molecular scattering distribution. *Applied Optics*, **30**, 4427–4438. [24](#)
- MOREL, A. & PRIEUR, L. (1977). Analysis of variations in ocean color. *Limnology and Oceanography*, **22**, 709–722. [9](#)
- NEUKERMANS, G., LOISEL, H., MÉRIAUX, X., ASTORECA, R. & MCKEE, D. (2012). In situ variability of mass-specific beam attenuation and backscattering of marine particles with respect to particle size, density, and composition. *Limnology and Oceanography*, **57**, 124–144. [56](#), [57](#), [58](#)
- OMAR, A.F. & MATJAFRI, M.Z. (2009). Turbidimeter design and analysis: a review on optical fiber sensors for the measurement of water turbidity. *Sensors (Basel)*, **9**, 8311–8335. [24](#)
- ORGANELLI, E., BRICAUD, A., ANTOINE, D. & UITZ, J. (2013). Multivariate approach for the retrieval of phytoplankton size structure from measured light absorption spectra in the mediterranean sea (boussole site). *Applied Optics*, **52**, 2257–2273. [50](#)
- OUBELKHEIR, K., CLAUSTRE, H., SCIANDRA, A. & BABIN, M. (2005). Bio-optical and biogeochemical properties of different trophic regimes. *Limnology and Oceanography*, **50**, 1795–1809. [50](#)
- PEGAU, S., ZANEVELD, J.R., MITCHELL, B.G., MUELLER, J.L., KAHRU, M., WIELAND, J. & STRAMSKA, M. (2003). Ocean optics protocols for satellite ocean color sensor validation. chap. Inherent Optical Properties: instruments, characterizations, field measurements and data analysis protocols, NASA. [27](#), [32](#), [33](#), [35](#), [36](#)
- PEGAU, W.S., GRAY, D. & ZANEVELD, J.R. (1997). Absorption and attenuation of visible and near-infrared light in water: Dependence on temperature and salinity. *Applied Optics*, **36**, 6035–6046. [19](#), [36](#), [39](#), [76](#)
- PELEVIN, V.N. & RUTKOVSKAYA, V.A. (1977). On the optical classification of ocean waters from the spectral attenuation of solar radiation. *Oceanology*, **17**, 28–32. [9](#)
- PETZOLD, T. & AUSTIN, R.W. (1968). An underwater transmissometer for ocean survey work. In *Underwater photo-optical instrument applications*, vol. 12, 133–137, SPIE. [26](#), [27](#)
- PETZOLD, T.J. (1972). Volume scattering functions for selected ocean waters. Tech. Rep. 72, Scripps Institution of Oceanography. [24](#)

- POPE, R. & FRY, E. (1997). Absorption spectrum (380-700 nm) of pure water, ii, integrating cavity measurements. *Applied Optics*, **36**, 8710–8723. [xi](#), [19](#), [20](#), [73](#)
- PREISENDORFER, R.W. (1976). *Hydrological Optics*. US Department of Communication NOAA, Honolulu, HA. [10](#)
- PRIEUR, L. & SATHYENTRANATH, S. (1981). An optical classification of coastal and oceanic waters based on the specific spectral absorption curves of phytoplankton pigments, dissolved organic matter and other particulate materials. *Limnology and Oceanography*, **26**, 671–689. [9](#)
- RAMÍREZ-PÉREZ, M., RÖTTGERS, R., TORRECILLA, E. & PIERA, J. (2015). Cost-effective hyperspectral transmissometers for oceanographic applications: performance analysis. *Sensors*, **15**, 20967–20989. [39](#), [53](#)
- ROESLER, C.S. & BOSS, E. (2008). Real-time coastal observing systems for marine ecosystem dynamics and harmful algal blooms: Theory, instrumentation and modelling. chap. In situ measurements of the inherent optical properties (IOPs) and potential for harmful algal bloom detection and coastal ecosystem observations. In *Real-Time Coastal Observing Systems for Ecosystem Dynamics and Harmful Algal Blooms*, 153–206, UNESCO. [26](#)
- ROESLER, C.S. & PERRY, M.J. (1995). In-situ phytoplankton absorption, fluorescence emission, and particulate backscattering spectra determined from reflectance. *Journal of Geophysical Research*, **100**, 13279–13294. [25](#)
- ROESLER, C.S., PERRY, M.J. & CARDER, K.L. (1989). Modeling in situ phytoplankton absorption from total absorption spectra in productive inland marine waters. *Limnology and Oceanography*, **34**, 523–531. [22](#)
- RÖTTGERS, R. & DOERFFER, R. (2007). Measurements of optical absorption by chromophoric dissolved organic matter using a point-source integrating-cavity absorption meter. *Limnology and Oceanography Methods*, **5**, 126–135. [29](#), [77](#)
- RÖTTGERS, R. & GEHNKE, S. (2012). Measurement of light absorption by aquatic particles: improvement of the quantitative filter technique by use of an integrating sphere approach. *Applied Optics*, **51**, 1336–1351. [54](#)
- RÖTTGERS, R., SCHOENFELD, W., KIPP, P.R. & DOERFFER, R. (2005). Practical test of point-source integrating cavity absorption meter. the performance of different collector assemblies. *Applied Optics*, **44**, 5549–5560. [77](#)

- RÖTTGERS, R., HEYMANN, K. & KRASEMANN, H. (2014a). Suspended matter concentrations in coastal waters: Methodological improvements to quantify individual measurement uncertainty. *Estuarine and Coastal Shelf Science*, **151**, 148–155. [54](#), [55](#)
- RÖTTGERS, R., MCKEE, D. & UTSCHIG, C. (2014b). Temperature and salinity correction coefficients for light absorption by water in the visible to infrared spectral region. *Optics Express*, **22**, 25093–25108. [36](#), [39](#), [40](#)
- SABBAH, S., FRASER, J.M., BOSS, E., BLUM, I. & HAWRYSHYN, C.W. (2010). Hyper-spectral portable beam transmissometer for the ultraviolet-visible spectrum. *Limnology and Oceanography: Methods*, **8**, 527–538. [37](#)
- SATHYENDRANATH, S. (2000). Remote sensing of ocean colour in coastal and other optically-complex waters. Tech. Rep. 3, International Ocean-Colour Coordinating Group (IOCCG), Dartmouth, Canada. [10](#)
- SCHLITZER, R. (2016). Odv: Ocean data view, version 4_7_6. <http://odv.awi.de>. [61](#), [63](#)
- SCHOFIELD, O., BERGMANN, T., OLIVER, M.J., IRWIN, A., KIRKPATRICK, G., BISSETT, W.P., MOLINE, M.A. & ORRICO, C. (2004). Inversion of spectral absorption in the optically complex coastal waters of the mid-atlantic bight. *Journal of Geophysical Research*, **109**, C12S04. [72](#)
- SCHROTENBOER, B.R. & ARBOGAST, A.F. (2010). Locating alternative sand sources for michigan’s foundry industry: A geographical approach. *Applied Geography*, **30**, 697–719. [18](#)
- SMITH, R.C. & BAKER, K.S. (1978). The bio-optical state of ocean waters and remote sensing. *Limnology and Oceanography*, **23**, 247–259. [9](#)
- SMITH, R.C. & BAKER, K.S. (1981). Optical properties of the clearest natural waters (200–800 nm). *Applied Optics*, **20**, 177–184. [19](#)
- SOGANDARES, F.M. & FRY, E.S. (1997). Absorption spectrum (340–640 nm) of pure water, i, photothermal measurements. *Applied Optics*, **33**, 8699–8709. [19](#)
- SOLÉ, J., TURIÉL, A., ESTRADA, M., LLEBOT, C., BLASCO, D., CAMP, J., DELGADO, M., FERNÁNDEZ, M. & DIOGENE, J. (2009). Climatic forcing on hydrography of a mediterranean bay (alfacs bay). *Continental Shelf Research*, **29**, 1786–1800. [51](#)
- SPINRAD, R.W., ZANEVELD, J.R.V. & KITCHEN, J.C. (1983). A study of the optical characteristics of the suspended particles in the benthic nepheloid layer of the scotian rise. *Journal of Geophysical Research*, **88**, 7641–7645. [32](#)

- STAVN, R.H., RICKB, H.J. & FALSTERC, A.V. (2009). Correcting the errors from variable sea salt retention and water of hydration in loss on ignition analysis: Implications for studies of estuarine and coastal waters. *Estuarine and Coastal Shelf Sciences*, **81**, 575–582. [55](#)
- STOJANOVIC, R. & KARADAGLIC, D. (2007). An optical sensing approach based on light emitting diodes. *Journal of Physics: Conference Series*, **76**, 012054. [32](#)
- STRAMSKI, D. & KIEFER, D.A. (1991). Light scattering by microorganisms in the open ocean. *Progress in Oceanography*, **28**, 343–383. [15](#)
- STRAMSKI, D. & MOREL, A. (1990). Optical properties of photosynthetic picoplankton in different physiological states as affected by growth irradiance. *Deep Sea Research*, **37**, 245–266. [71](#)
- STRAMSKI, D., BRICAUD, A. & MOREL, A. (2001). Modeling the inherent optical properties of the ocean based on the detailed composition of planktonic community. *Applied Optics*, **40**, 392–403. [26](#)
- STRAMSKI, D., BOSS, E., BOGUCKI, D. & VOSS, K.J. (2004). The role of seawater constituents in light backscattering in the ocean. *Progress in Oceanography*, **61**, 27–56. [18](#)
- STRÖMBECK, N., CANDIANI, G., GIARDINO, C. & ZILIOLI, E. (2003). Water quality monitoring of lake garda using multi-temporal data. In *MERIS User Workshop*, Frascati, Italy. [71](#)
- SULLIVAN, J.M., TWARDOWSKI, M.S., ZANEVELD, J.R.V., MOORE, C.M., BARNARD, A.H., DONAGHAY, P.L. & RHOADES, B. (2006). Hyperspectral temperature and salt dependencies of absorption by water and heavy water in the 400–750 nm spectral range. *Applied Optics*, **45**, 5294–5309. [36](#), [39](#), [40](#)
- SUTTLE, C.A., CHAN, A.M. & COTTRELL, M.T. (1990). Infection of phytoplankton by viruses and reduction of primary productivity. *Nature*, **347**, 467–469. [15](#)
- TALYOR, B.B., TORRECILLA, E., BERNHARDT, A., TAYLOR, M.H., PEEKEN, I., RÖTTGERS, R., PIERA, J. & BRACHER, A. (2011). Bio-optical provinces in the eastern atlantic ocean and their biogeographical relevance. *Biogeosciences*, **8**, 3609–3629. [54](#)
- TANG, Q., ZHANG, J. & FANG, J. (2011). Shellfish and seaweed mariculture increase atmospheric co2 absorption by coastal ecosystems. *Marine Ecology Progress Series*, **424**, 97–104. [6](#)

- TAYLOR, B.B., TAYLOR, M., DINTER, T. & BRACHER, A. (2013). Estimation of relative phycoerythrin concentrations from hyperspectral underwater radiance measurements. a statistical approach. *Journal of Geophysical Research: Oceans*, **118**, 2948–2960. 50
- TORRECILLA, E., TRAMSKI, D., REYNOLDS, R.A., MILLAN-NUNEZ, E. & PIERA, J. (2011). Cluster analysis of hyperspectral optical data for discriminating phytoplankton pigment assemblages in the open ocean. *Remote Sensing Environment*, **115**, 2578–2593. 50
- TRIOS BROCHURE (2014). Vis-photometer viper product brochure. <http://trios.de>. 33
- TWARDOWSKI, M.S., LEWIS, M., BARNARD, A. & ZANEVELD, J.R.V. (2005). Remote sensing of coastal aquatic waters. chap. In-water instrumentation and platforms for ocean color remote sensing applications, 69–100, Springer Publishing. 25, 26
- VAN DE HULST, H.C. (1957). *Light Scattering by Small Particles*. John Wiley & Sons, New York. 24, 56
- VOSS, K.J. (1992). A spectral model of the beam attenuation coefficient in the ocean and coastal areas. *Limnology and Oceanography*, **37**, 501–509. 25, 56
- VOSS, K.J. & AUSTIN, R.W. (1993). Beam-attenuation measurement error due to small-angle scattering acceptance. *American Meteorological Society*, **10**, 113–121. 46
- VOSS, K.J. & FRY, E.S. (1984). Measurement of the mueller matrix for ocean water. *Applied Optics*, **23**, 4427–4439. 18
- WELLS, M.L. & GOLDBERG, E.D. (1991). Occurrence of small colloids in sea water. *Nature*, **353**, 342–344. 15
- WETLABS (2014). Ac meter protocol. http://www.commttec.com/Prods/mfgs/WetLabs_Prods.html. 43
- YIN, Z., LIU, X., WANG, H., WU, Y., HAO, X., Z, Z.J. & XU, X. (2013). Light transmission enhancement from hybrid zno micro-mesh and nanorod arrays with application to gan-based light-emitting diodes. *Optics Express*, **21**, 28531–28542. 32
- ZANEVELD, J.R.V. (1973). Variation of optical sea parameters with depth. *Optics of the Sea*, **61**, 1–22. 32
- ZANEVELD, J.R.V. & KITCHEN, J.C. (1995). The variation in the inherent optical properties of phytoplankton near an absorption peak as determined by various models of cell structure. *Journal of Geophysical Research*, **100**, 13309–13320. 24, 25, 56

ZANEVELD, J.R.V., KITCHEN, J.C. & MOORE, C. (1994). The scattering error correction of reflecting-tube absorption meters. In *Proceedings of Ocean Optics XII*, vol. 2258, 44–55, SPIE. [76](#)

This thesis has been funded by the Spanish Ministry of Economy and Competitiveness, by means of the FPI fellowship: BES-2012-054205.